INVESTIGATION OF THE MECHANISM OF INTERMEDIATE-DEPTH EARTHQUAKES IN THE PAMIR-HINDU KUSH REGION

Wan-Jou Chen, B.S.

An Abstract Presented to the Graduate Faculty of
Saint Louis University in Partial Fulfillment
of the Requirements for the Degree of
Master of Science (Research)

2012

Abstract

The Pamir–Hindu Kush seismic zone is caused by the collision of the Indian plate with the Eurasian plate. Earthquakes in this region can occur down to ~250 km depth. Intermediate-depth earthquakes that occur in the Hindu Kush region may be related to deformation and break-off of the Indian plate, dehydration of former oceanic crust in the northern margin of the Indian plate, or subduction of the Eurasian plate in the eastern part of the Pamir–Hindu Kush region. We use a cross-correlation-based method to estimate differential rupture duration between each pair of seismic stations to find the rupture direction and the orientation of the fault plane for 52 intermediate-depth earthquakes between 1990 and 2009. We found most of the analyzed intermediate-depth earthquakes are located in the western part of the Pamir-Hindu Kush seismic zone. Among the 52 analyzed earthquakes, we observed directivity for 13 intermediate-depth earthquakes. Moreover, 6 of the earthquakes that show directivity have their rupture toward the intersection of the nodal planes. Regardless of the rupture direction, we can classify the earthquakes with observable directivity at depths between 180 and 240 km into two clusters based on the orientation of the fault planes. Earthquakes in cluster I have similar rupture behavior. Furthermore, earthquakes in cluster II have their fault planes migrate with the shape of Indian slab.

INVESTIGATION OF THE MECHANISM OF INTERMEDIATE-DEPTH EARTHQUAKES IN THE PAMIR-HINDU KUSH REGION

Wan-Jou Chen, B.S.

A Thesis Presented to the Graduate Faculty of
Saint Louis University in Partial Fulfillment
of the Requirements for the Degree of
Master of Science (Research)

2012

COMMITTEE IN CHARGE OF CANDIDACY:

Assistant Professor Linda M. Warren,
Advisor and Chairperson

Professor Robert B. Herrmann

Associate Professor Lupei Zhu

Acknowledgements

I am deeply indebted to my advisor, Dr. Linda Warren, for her guidance and supervision. She provided information consistent support throughout my thesis. I would never have been able to finish it without her guidance. My grateful thanks also go to Dr. Robert Herrmann and Dr. Lupei Zhu for serving on my committee and reviewing my thesis. I would like to thank Dr. David Crossley for his help and support with my courses.

Finally, thanks to the entire faculty of the Department of Earth and Atmospheric Sciences for providing fascinating and enlightening courses. I learned more than I expected to learn. One of the most important things I learned is that students must begin to understand the origin of knowledge. Last but not least, I would like to express my gratitude to my friends and family who helped me to complete this thesis and my Master's degree.

Table of Contents

List of Tables ..... **iv**
List of Figures ..... **v**
Chapter 1. Introduction **1**
Chapter 2. Literature Review **3**
2.1 Intermediate-depth Earthquakes 3
2.1.1 Existence of Oceanic Crust 4
2.1.2 Orientation of Fault Planes 6
2.2 Tectonic History of the Hindu Kush-Pamir Region 7
Chapter 3. Methodology **12**
3.1 Fault Plane Ambiguity 12
3.2 Method for Fault Plane Identification 14
3.3 Data Selection 20
Chapter 4. Results **22**
4.1 Ruptures on the North-dipping Plane 22
4.2 Ruptures on the South-dipping Plane 26
4.3 Rupture Propagation towards the Nodal Plane Intersection 28
4.4 Earthquakes with Rupture Directions that cannot be interpreted 28
Chapter 5. Discussion **30**
5.1 Earthquakes that Show Directivity 30
5.1.1 Focal Mechanisms 30
5.1.2 Rupture Directions 36
5.1.3 3 March 2002 (Mw 7.4, Depth 225 km) Earthquake 37
5.2 Earthquakes without Directivity 40
Chapter 6. Conclusions **41**
Appendix A **42**
Appendix B **48**
References **91**
Vita Auctoris **96**

List of Tables

Table A1: Earthquake rupture parameters for the 13 earthquakes that show directivity. 42

Table A2: Earthquake rupture parameters for the 39 earthquakes that do not show directivity. 44

List of Figures

Figure 1: Topography map of the Pamir-Hindu Kush seismic zone 2

Figure 2: Example of the double-couple focal mechanism and the two possible rupture planes.....13

Figure 3: Map view of the rupture duration and the rupture-takeoff angle.....15

Figure 4: An ideal model for a unilateral earthquake rupture and three seismic stations deployed on the surface of the Earth 17

Figure 5: Slab contours and distribution of the 52 intermediate-depth earthquakes (white dots) for the 1990 to 2009 time period used in this study 21

Figure 6: Seismograms of the 13th May 1997 earthquake (Mw 6.5, 196 km depth) with rupture propagation on the north-dipping plane. 24

Figure 7: The 31 January 1991 23:03:33.67 earthquake (Mw 6.9, depth 118 km) 25

Figure 8: The 13 July 1990 14:20:43.47 earthquake (Mw 6.4, depth 216 km).....27

Figure 9: Relative locations and focal mechanisms of the 13 intermediate-depth earthquakes 32

Figure 10: Focal mechanisms of earthquakes in cluster I 33

Figure 11: Close view of the focal spheres in cluster II, which was shown in Figure 9, and the focal mechanisms for earthquakes in cluster II. 35

Figure 12: Histograms showing the distribution of rupture propagation for the six earthquakes with their ruptures propagating toward the intersection of the nodal planes 36

Figure 13: A simple cartoon shows a vertical view of the relative location of the two subevents of the 3 March 2002 Mw 7.4 earthquake in the Kiser et al. (2011) study 38

Figure 14: The seismograms of 3 March 2002 12:08:07.81 (Mw 6.3, depth 216 km) and 12:08:19.74 (Mw 7.4, depth 225 km) earthquakes. 39

Figure B1: Results for the 13 July 1990, Mw 6.4 earthquake, which occurred at 36.42°N 70.79°E and 216 km depth. 49

Figure B2: Synthetics for the north-dipping subhorizontal plane for the 13 July 1990, Mw 6.4 earthquake 50

Figure B3: Synthetics for the south-dipping near-vertical plane for the 13 July 1990, Mw 6.4 earthquake 51

Figure B4: Results for the 31 January 1991, Mw 6.9 earthquake, which occurred at 35.99°N 70.42°E and 142 km depth. 52

Figure B5: Synthetics for the north-dipping subhorizontal plane for the 31 January 1991, Mw 6.9 earthquake. 53

Figure B6: Synthetics for the south-dipping near-vertical plane for the 31 January 1991, Mw 6.9 earthquake 54

Figure B7: Results for the 14 July 1991, Mw 6.4 earthquake, which occurred at 36.33°N 71.12°E and 212 km depth. 55

Figure B8: Synthetics for the north-dipping plane for the 14 July 1991, Mw 6.4 earthquake. 56

Figure B9: Synthetics for the south-dipping plane for the 14 July 1991, Mw 6.4 earthquake. 57

Figure B10: Results for the 9 August 1993, Mw 6.3 earthquake, which occurred at 36.44°N 70.71°E and 204 km depth. 58

Figure B11: Synthetics for the north-northeast-dipping subhorizontal plane for the 9 August 1993, Mw 6.3 earthquake. 59

Figure B12: Synthetics for the south-southwest-dipping near-vertical plane for the 9 August 1993, Mw 6.3 earthquake. 60

Figure B13: Results for the 30 June 1994, Mw 6.3 earthquake, which occurred at 36.33°N 71.13°E and 226 km depth. 61

Figure B14: Synthetics for the more west-northwest-dipping plane for the 30 June 1994, Mw 6.3 earthquake.....62

Figure B15: Synthetics for the more vertical east-southeast-dipping plane for the 30 June 1994, Mw 6.3 earthquake. 63

Figure B16: Results for the 25 October 1994, Mw 6.0 earthquake, which occurred at 36.36°N 70.96°E and 238 km depth. 64

Figure B17: Synthetics for the north-dipping plane for the 25 October 1994, Mw 6.0 earthquake. 65

Figure B18: Synthetics for the south-southeast-dipping plane for the 25 October 1994, Mw 6.0 earthquake.....66

Figure B19: Results for the 13 May 1997, Mw 6.5 earthquake, which occurred at 36.41°N 70.94°E and 196 km depth. 67

Figure B20: Synthetics for the north-dipping plane for the 13 May 1997, Mw 6.5 earthquake. 68

Figure B21: Synthetics for the southeast-dipping plane for the 13 May 1997, Mw 6.5 earthquake. 69

Figure B22: Results for the 14 February 1998, Mw 5.5 earthquake, which occurred at 36.36°N 71.11°E and 218 km depth.....70

Figure B23: Synthetics for the north-dipping subhorizontal plane for the 14 February 1998, Mw 5.5 earthquake. 71

Figure B24: Synthetics for the south-dipping near-vertical plane for the 14 February 1998, Mw 5.5 earthquake. 72

Figure B25: Results for the 12 May 2000, Mw 6.3 earthquake, which occurred at 35.97°N 70.66°E and 107 km depth. 73

Figure B26: Synthetics for the southwest-dipping subhorizontal plane for the 12 May 2000, Mw 6.3 earthquake. 74

Figure B27: Synthetics for the northwest-dipping near-vertical plane for the 12 May 2000, Mw 6.3 earthquake. 75

Figure B28: Results for the 23 November 2001, Mw 6.1 earthquake, which occurred at 36.39°N 71.51°E and 106 km depth. 76

Figure B29: Synthetics for the north-northwest-dipping plane for the 23 November 2001, Mw 6.1 earthquake. 77

Figure B30: Synthetics for the south-southeast-dipping plane for the 23 November 2001, Mw 6.1 earthquake. 78

Figure B31: Results for the 3 March 2002, Mw 6.3 and Mw 7.4 earthquakes, which occurred at 36.43°N 70.44°E 209 km depth and 36.50°N 70.48°E 225 km depth, separately. 79

Figure B32: Synthetics for the north-northeast-dipping subhorizontal plane for the 3 March 2002 Mw 6.3 and Mw 7.4 earthquakes. 80

Figure B33: Synthetics for the south-southwest-dipping near-vertical plane for the 3 March 2002 Mw 6.3 and Mw 7.4 earthquakes. 81

Figure B34: Results for the 3 March 2002, Mw 7.4 earthquake, which occurred at 36.50°N 70.48°E and 225 km depth. 82

Figure B35: Synthetics for the north-northeast-dipping subhorizontal plane for the 3 March 2002, Mw 7.4 earthquake. 83

Figure B36: Synthetics for the south-southwest-dipping near-vertical plane for the 3 March 2002, Mw 7.4 earthquake. 84

Figure B37: Results for the 12 December 2005, Mw 6.5 earthquake, which occurred at 36.36°N 71.09°E and 224 km depth. 85

Figure B38: Synthetics for the north-dipping plane for the 12 December 2005, Mw 6.5 earthquake.....86

Figure B39: Synthetics for the south-dipping plane for the 12 December 2005, Mw 6.5 earthquake.....87

Figure B40: Results for the 22 October 2009, Mw 6.2 earthquake, which occurred at 36.52°N 70.95°E and 185 km depth. 88

Figure B41: Synthetics for the south-southeast-dipping plane for the 22 October 2009, Mw 6.2 earthquake.....89

Figure B42: Synthetics for the north-northwest-dipping plane for the 22 October 2009, Mw 6.2 earthquake.....90

Chapter 1. Introduction

The Pamir–Hindu Kush is an orogenic area deformed and created by the collision of the Indian plate with the Eurasian plate. The region is characterized by high concentrations of intermediate-depth earthquakes. The Pamir–Hindu Kush seismic zone is surrounded by several blocks such as the Afghan block, the Turan plate, and the Tarim block (Koulakov and Sobolev, 2006) (Figure 1). The contact between the Indian and the Eurasian plates started at the Eocene, and their continuous collision results in strong compression and crustal thickening in the Pamir-Hindu Kush area. Earthquakes around the Hindu Kush seismic zone can occur down to ~250 km depth and their distribution dips to the north under the western and central parts of the Hindu Kush area and southwards underneath the Pamir region. Researchers have proposed this view of the Pamir-Hindu Kush seismic zone from seismic tomography modeling, earthquake locations, thermal modeling, and gravity modeling. However, the cause of the intermediate-depth earthquakes is still debatable. In this study, we will focus on the intermediate-depth earthquakes that occurred in the Pamir-Hindu Kush seismic zone in order to learn more about the earthquake process.

The reason for the high concentration of intermediate-depth earthquakes in the Pamir-Hindu Kush area is still unknown. Globally, the intermediate-depth earthquakes occur in subduction zones. However, the Pamir-Hindu Kush seismic zone is a continent-continent collision zone, which makes the origin of deeper earthquakes in this region mysterious. We hope to find the rupture direction and the orientation of the fault plane of intermediate-depth earthquakes to better define the geometry of the

surfaces on which they occur. If we can identify which of the two possible fault planes (of the focal mechanism) is the real fault plane, we may be able to determine the cause of the intermediate-depth earthquakes that take place in the Pamir-Hindu Kush seismic zone.

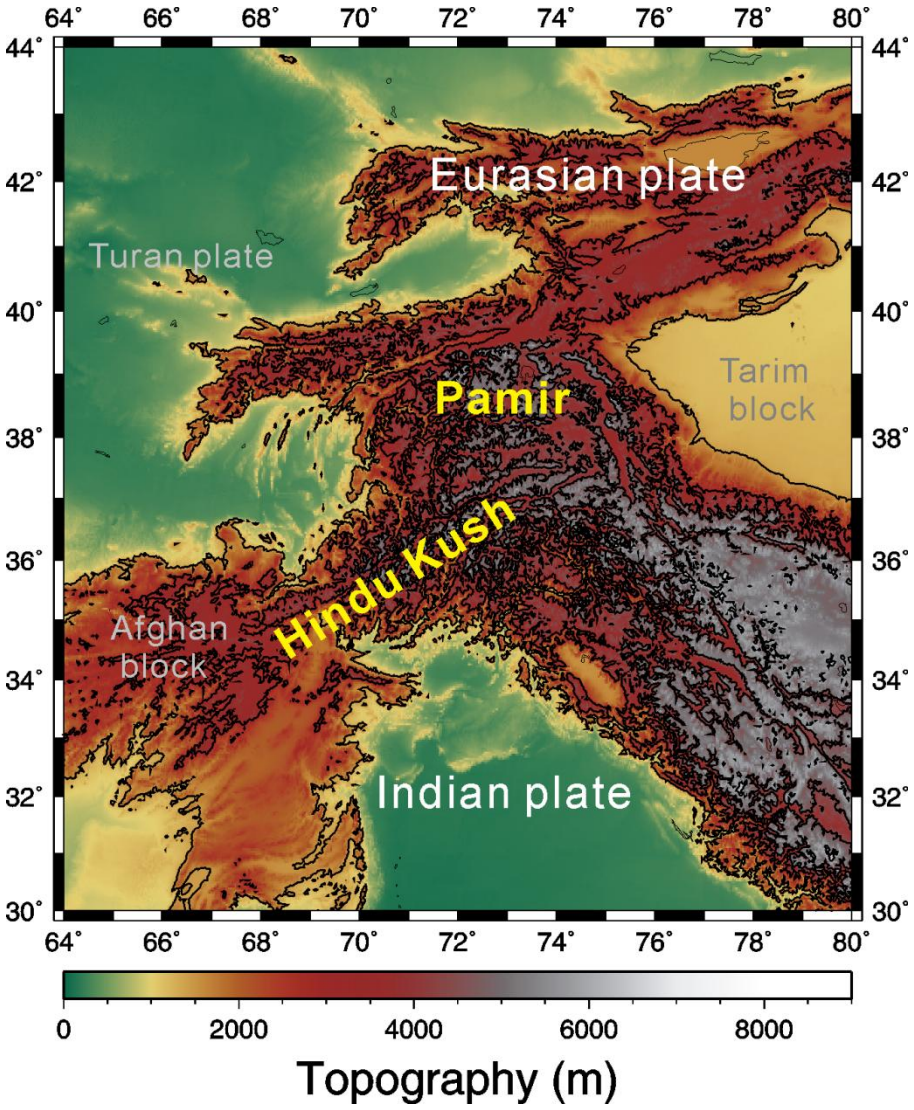

Figure 1: Topography map of the Pamir-Hindu Kush seismic zone. The Pamir-Hindu Kush mountain belt is deformed and created by the collision of the Indian plate with the Eurasian plate, and is surrounded by several blocks such as the Afghan block, the Turan plate, and the Tarim block (Koulakov and Sobolev, 2006).

Chapter 2. Literature Review

2.1 Intermediate-depth Earthquakes

Earthquakes consist of sudden energy released from sudden failures of the Earth's material. In general, earthquakes that happen in the depths between 0 and 70 km are known as shallow earthquakes, between 70 and 300 km are intermediate-depth earthquakes, and deeper than 300 km are deep-focus earthquakes. The origin of intermediate-depth and deep-focus earthquakes is still an open question.

The source regions of shallow and deep earthquakes are different in terms of the physical environment and perhaps material properties, which makes the origin of deeper earthquakes mysterious. The source region of the deeper earthquakes has higher pressure and temperature than that of shallow earthquakes. However, intermediate-depth and deep-focus earthquakes still share the similar rupture characteristic of double-couple focal mechanisms with shallow earthquakes (Scholz, 2002; Frohlich, 2006) even though the source regions are different. The stress drops calculated from shallow and deep earthquakes do not show big differences (Scholz, 2002).

2.1.1 Existence of Oceanic Crust

Dehydration and deformation in the subducting oceanic slab are two of the main factors commonly believed to be causing the earthquakes in subduction zones (McGinnis, 1971; Van der Voo, Spakman, and Bijwaard, 1999; Hacker, Abers, and Peacock, 2003; Zarifi and Havskov, 2003; Omori, Komabayashi, and Maruyama, 2004; Replumaz, Karason, van der Hilst, Besse, and Tapponnier, 2004; Hafkenscheid, Wortel, and Spakman, 2006; Koulakov and Sobolev, 2006; Lister, Kennett, Richards, and Marnie, 2008; Lou, Chen, Yu, and Ning, 2009; Replumaz, Negredo, Guillot, and Villaseñor, 2010; Brantut, Sulem, and Schubnel, 2011). Water released by dehydration of hydrous minerals within the old and cold subducted oceanic plate may cause local weakening at specific stress conditions (Omiri et al., 2004). Melting may break along fractures at great depths because, in general, melted rocks need more space than solid rocks. Dehydration reactions can increase the pore pressure at a specific temperature, and lead to reduced effective stress on the fault, which makes the system of rocks become unstable (Brantut et al., 2011). However, whether water can be stored at depths deeper than 200 km is still debatable.

The dense clustering of intermediate-depth earthquakes in the Pamir-Hindu Kush seismic zone, which occurs down to a depth of 250 km, has led several researchers to propose that there was once an oceanic lithosphere connected with the Indian plate margin with Eurasia (McGinnis, 1971; Van der Voo et al., 1999; Hacker et al., 2003; Zarifi and Havskov, 2003; Replumaz et al., 2004; Hafkenscheid et al., 2006; Koulakov and Sobolev, 2006; Lister et al., 2008; Lou et al., 2009; Replumaz et al., 2010). The existence of the oceanic slab is based on the observation of high velocity

anomalies deeper than 200 km depth. Since the density of the oceanic slab is higher than that of the continental slab, seismic waves propagate faster in the oceanic slab than in the continental slab. Depending on the seismic tomography model, P- and S-wave anomalies in the upper mantle beneath the Hindu Kush seismic zone show that there are high velocity anomalies below 200 km depth and low velocity anomalies above 200 km (Negredo, Replumaz, Villaseñor, and Guillot, 2007; Replumaz et al., 2010). This observation suggests a transition from continental to oceanic slabs as depth increases. The transition between continental and oceanic crust also allows the slab to be bent easily (Lou et al., 2009). Replumaz et al. (2010) indicated that the observed high velocity anomaly block might be caused by the late Mesozoic subducting oceanic slab, which broke off at ~45 Ma. The gravity field model around the Pamir-Hindu Kush region made by McGinnis (1971) showed negative free-air and isostatic anomalies in the eastern Hindu Kush region and in the Pamir area. This observation is consistent with a lower-density continental crust being pulled down into the denser mantle.

However, Hacker et al. (2003) indicated there are no water-containing minerals in the subducting slab at depths > 100 km, which means that intermediate-depth earthquakes that happen at depths between 100 and 250 km are not related to dehydration. Lister et al. (2008) used spherical trigonometry to map the distribution of epicenters in the Hindu Kush seismic zone, and suggested that earthquakes located in the interior of the subducting slab beneath the Hindu Kush region were located at a depth of 200 km. They found that there was no obvious orientation cluster for the slip vectors of active fault planes for earthquakes at depth between 75 and 180 km. However, they observed

that deeper earthquakes have obvious orientation clusters. The slip directions of the fault planes plunge steeply southwards, and are scattered at the range between 80° and 180° (Lister et al., 2008). As a result, they suggest that the subducting slab tends to stretch, tear, and then break off, which makes the slip directions migrate as a shape of boudinage. Warren (2008) suggested that a sausage-shaped feature of the subducting slab at the depth of ~200 km stretched and broke-off underneath the Hindu Kush area. This contention provides a possible explanation for the origin of intermediate-depth earthquakes in this collision zone without dehydration.

2.1.2 Orientation of Fault Planes

Well-known intermediate-depth seismic zones, such as Java, Vanuatu, Tonga-Kermadec, Alaska, Vrancea, Bucaramanga, and Hindu-Kush, are all located in regions where subduction happened (Zarifi and Havskov, 2003; Kiser, Ishii, Langmuir, Shearer, and Hirose, 2011). In the subduction zone, the shape of subducting slabs range from sub-horizontal to overturned, which makes their dip angle domain from 0° to > 90° (Luyendyk, 1970; Zarifi and Havskov, 2003; Cruciani, Carminati, and Doglioni, 2005; Warren, Hughes, and Silver, 2007; Warren, Langstaff, and Silver, 2008). As the plate bends, tensional stress in the oceanic crust creates normal faults, generally called outer-rise faults. Dip angles of the outer-rise faults on the Earth's surface are associated with the bending of the subducting plate. The fault planes on the outer-rise of the trench dip toward and away from the trench at angles between 30° and 60° (Masson, 1991). Understanding the dip angle of the outer-rise faults can help us to understand whether the preexisting slab structure can also influence the orientation of deep earthquakes.

Warren et al. (2007, 2008) suggested that most of the intraplate earthquakes occur near the top surface of the subducting slabs. Kiser et al. (2011) then used back projection analysis to determine the energy distribution of large intermediate-depth earthquakes and found that the fault planes of analyzed intermediate-depth earthquakes in their study tend to be horizontal.

2.2 Tectonic History of the Hindu Kush-Pamir Region

While intermediate-depth earthquakes occur in places with an oceanic trench, the Pamir-Hindu Kush seismic zone is a special area to study intermediate-depth earthquakes because, presently, it is a continent-continent collision. The tectonic history of the Hindu Kush has been reconstructed from tomography models, but there are still a number of unanswered questions. For example, are there one or two subducting slabs? Was oceanic crust connected with the former margin of the Indian plate before subduction happened? The Pamir-Hindu Kush seismic zone is characterized by a high concentration of intermediate-depth earthquakes at depths down to 250 km, which is related to the northward subducting Indian plate underneath the Eurasian plate. However, it is still controversial whether or not the Eurasian plate subducted underneath the Indian plate beneath the Pamir region. Some researchers suggested that there is only one northward subducting Indian plate, which overturns and breaks off beneath the Pamir-Hindu Kush region (Lukk and Vinnik, 1975; Billington, Isacks, and Barazangi, 1977; Vinnik, Lukk, and Nersesov, 1977; Pegler and Das, 1998; Van der Voo et al., 1999; Pavlis and Das, 2000; Zarifi and Havskov, 2003; Koulakov and Sobolev, 2006), whereas other studies suggested that there are

two distinct slabs underneath the Pamir-Hindu Kush region subducting in opposite directions (Lukk and Vinnik, 1975; Billington et al., 1977; Pegler and Das, 1998, Koulakov and Sobolev, 2006). These studies propose that the distribution of earthquakes in the Pamir-Hindu Kush seismic zone dips to the north under the Hindu Kush region and migrates southwards under the Pamir region.

Arguing for a single subducting slab, Koulakov and Sobolev (2006) used P- and S-wave velocity anomalies to calculate a seismic tomography model of the upper mantle beneath the area at latitude between 35°N–40°N, and longitude between 69°E–77°E. Their tomography model shows that a northward dipping slab of the Indian plate reaches to 500 km depth in the western part of the Pamir-Hindu Kush area (longitude between 67°E–68°E), and then gradually overturns and rotates at longitude between 70°E–72°E. Farther to the east, their model indicates that the subducting slab becomes thinner at ~200 km depth, which suggests that the slab break-off has developed gradually. Moreover, in the eastern part of the Pamir-Hindu Kush region, they do not observe any indication of the slab penetrating through the asthenosphere, which may indicate that the slab break-off has already occurred and the detached slab sank even deeper and cannot be detected by the seismic velocity methods in this region. Based on their tomographic model, the Indian plate subducted northward underneath the Eurasian plate and started to overturn and gradually break off towards the eastern part of the Pamir-Hindu Kush region. They also observed that most of the earthquakes are located coincidentally in the high seismic velocity blocks, which supports the supposition that the Indian slab overturns and gradually breaks off towards the east.

Negredo et al. (2007) and Replumaz et al. (2010) try to clarify the spatio-temporal evolution between the Indian and Eurasian plates. They proposed that the contact of the Indian plate and the Eurasian plate started at ~55 Ma. Based on the distribution of the high velocity anomalies today, they reconstructed the location of the Indian plate back to ~44 Ma and inferred that the evolution of the western part of the Indian plate was characterized by two episodes of steep subduction of the northern margin: the first subduction episode started at ~40 to 30 Ma and ended by a big slab break-off at ~15 Ma; the second episode of subduction beneath the Hindu Kush region started at ~8 Ma.

On the other hand, some studies suggested that there are two distinct slabs underneath the Pamir-Hindu Kush region subducting toward opposite directions. That is, the Indian plate subducts northward underneath the Eurasian plate in the Hindu Kush region, and the southward underthrusting Eurasian plate subducted beneath the Indian plate in the Pamir region (Chatelin, Roecker, Hatzfeld, and Molnar, 1980; Roecker, 1982; Verma and Sekhar, 1985; Hamburger, Sarewitz, Palvis, and Popandopulo, 1992, Burtman and Molnar, 1993; Fan, Ni, and Wallace, 1994; Zhu et al., 1997; Zarifi and Havskov, 2003; Lou et al., 2009).

Lou et al. (2009) used a double-difference algorithm (hypoDD) to relocate the earthquakes beneath the Pamir-Hindu Kush region between 1964 and 2003. The dip direction of the distribution of the relocated earthquakes overturned obviously at the region around latitude 37°N and longitude 71°E. To the west of this region, the Hindu Kush seismic zone dips northward with gradually increasing dip angle from west to

east. Underneath the Pamir seismic zone, the distribution of the earthquakes dips southward, with concentrated shallow earthquakes along the northern margin of the Pamir seismic zone and intermediate-depth earthquakes underneath this seismic region, as the dip direction varies from southeast to south from west to east. Furthermore, they proposed that the two-layered Wadati-Benioff zone underneath Pamir and Hindu Kush seismic zones are not connected with each other, which indicates that the intermediate-depth earthquakes beneath the Pamir-Hindu Kush region are caused by two slabs subducting in different directions.

The temperature distribution model made by Negredo et al. (2007) underneath the Pamir-Hindu Kush regions shows two different patterns of temperature distribution within the subducted slab(s) in each region. For example, the isotherms are more depressed within the slab under the Hindu Kush region than the slab underneath the Pamir region. This observation indicates that the subduction rate in the Hindu Kush region is higher than in the Pamir region, which is compatible with the presence of two subducting slabs.

To sum up, the mechanism and possible origin of the intermediate-depth earthquakes in the Pamir-Hindu Kush region is still controversial. Well-known intermediate-depth seismic zones are all located in regions where subduction happened. Today, the Pamir-Hindu Kush seismic zone is a continent-continent collision area, which makes it an interesting environment in which to study the intermediate-depth earthquakes. The intriguing questions are “Does dehydration occur in the oceanic crust underneath the Pamir-Hindu Kush seismic zone?” or “Does the slab detachment cause the

intermediate-depth earthquakes to occur?" Among the studies that have been mentioned, the boudinage-shaped subducted Indian slab (Lister et al., 2008; Warren, 2008) provides an appropriate explanation of the orientation of the fault planes for the intermediate-depth and deep-focus earthquakes in the Pamir-Hindu Kush region. In this paper, we would like to focus our study on the mechanism and behavior of the intermediate-depth earthquakes that occur in the Pamir-Hindu Kush region.

Chapter 3. Methodology

3.1 Fault Plane Ambiguity

Earthquakes are caused by the sudden release of accumulated strain energy within the Earth. There are several ways to analyze the rupture and identify the fault plane during an earthquake, such as measuring the visible fractures show on the Earth's surface, finding the distribution of the aftershocks since aftershocks preferentially occur along the fault plane, or studying the seismic waves via source finiteness. For intermediate-depth earthquakes, however, there is no evidence of apparent rupture on the surface.

There are two possible fault planes in a double-couple focal mechanism for each earthquake, because the P-wave radiation pattern has two nodal planes (Figure 2). Observed seismic signals from different locations can be used to resolve the fault plane ambiguity because the earthquake rupture process is finite in time and space. Fault length and duration of the rupture can be derived by studying the change in corner frequency in the frequency domain or the corresponding observed pulse width along the different ray paths from the source of the seismograms in the time domain (Ben-Menahem, 1962; Li, He, and Yao, 2006). Since intermediate-depth earthquakes have sufficient separation in time between the direct P and the pP or sP arrivals, the pulse width of the P-wave can be used to characterize the finiteness effect if the earthquakes are not too large. The constraint is that the rupture process must be less than the true difference between P and pP or sP.

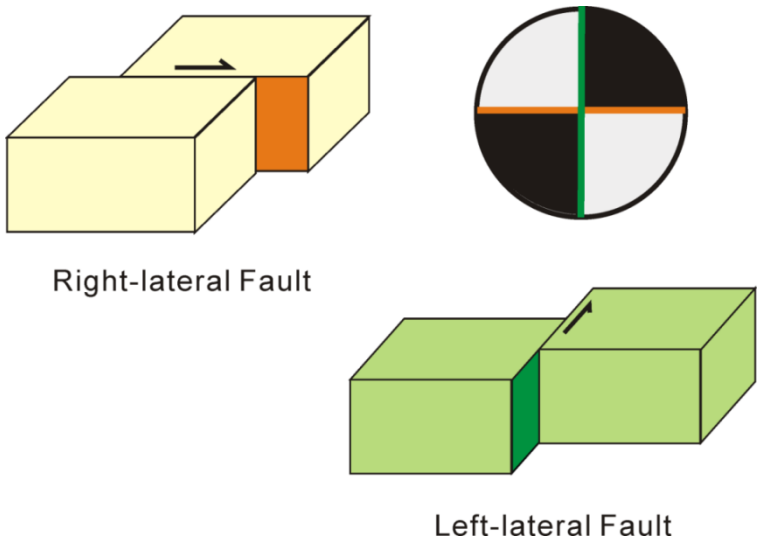

Figure 2: Example of the double-couple focal mechanism and the two possible rupture planes. Because of the P-wave radiation patterns, the double-couple focal mechanism acquired from the Global Harvard Centroid Moment Tensor (CMT) catalog provides two possible fault planes for an earthquake. The block diagrams show the two possible fault planes. The green line on the focal mechanism is the rupture plane of the left-lateral fault; the orange line is the rupture plane for the right-lateral fault.

3.2 Method for Fault Plane Identification

The method for identifying the fault plane relies on a change in the signal duration which depends on the rupture direction and the direction of the P-wave from the source to the seismograph station. For a unilateral earthquake rupture (Figure 3), rupture starts at one point and propagates in one direction at a constant velocity v_r until the rupture stops. L is the length of the total rupture. The apparent rupture duration, τ, varies with different rupture angles, θ, (θ is the angle between the direction of rupture propagation and the takeoff vector to the station), as can be seen in the following equation:

$$\begin{aligned}\tau(\theta) &= \frac{L}{v_r} - \frac{L}{c} \times \cos\theta \\ &= \frac{L}{v_r}\left(1 - \frac{v_r}{c} \times \cos\theta\right) \\ &= a\left(1 - \frac{v_r}{\alpha} \times \cos\theta\right)\end{aligned}$$

where c is local seismic velocity, α is the P-wave velocity, and a is the actual rupture duration. Note the apparent rupture duration τ increases with the rupture takeoff angle θ for unilateral rupture earthquake.

Similar to the Doppler effect, rupture duration for single-event ruptures and travel time delay between sub-events for complex ruptures are shortest in the direction where the rupture is propagating toward the seismic station, and longest where the rupture propagates in a direction away from the station.

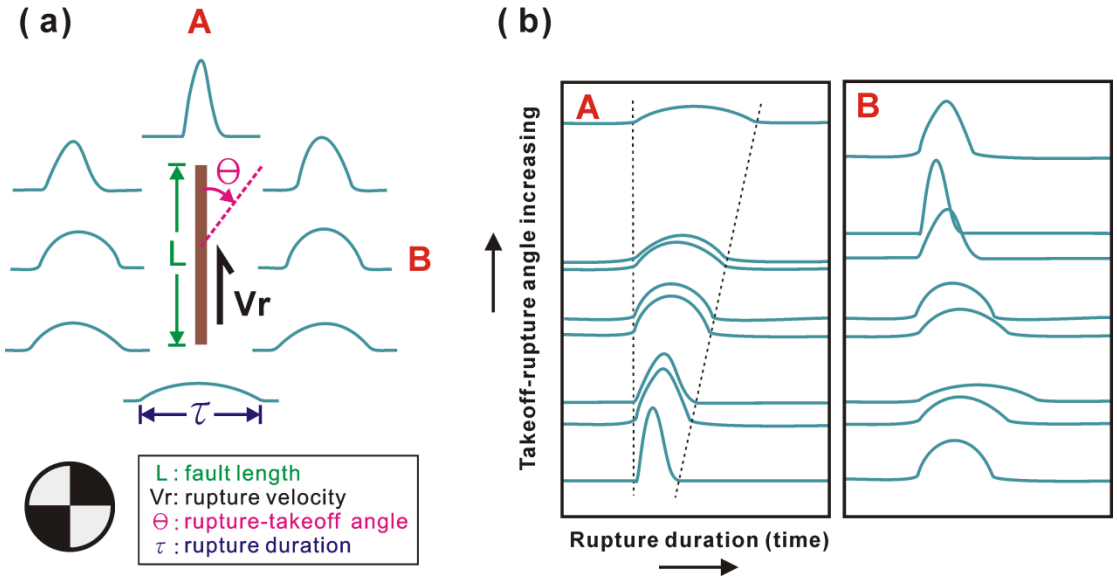

Figure 3: Map view of the rupture duration and the rupture-takeoff angle (azimuth for a special case with horizontal rupture to the north) between the direction of rupture propagation and the vector to the station for a simple unilateral rupture earthquake. As shown in Figure 2, there are two possible fault planes for a double-couple focal mechanism. In this study, we use the directivity of the rupture durations recorded by different stations with different rupture takeoff angles for each earthquake to determine the actual rupture direction. (a) For a left-lateral earthquake, the rupture duration τ varies with different azimuth θ. c is local seismic velocity, α is the P-wave velocity, and τ is the rupture duration shown on the seismogram. (b) From the map view, we know that the rupture of this earthquake propagating towards direction A. In direction A, the rupture duration increases with the rupture-takeoff angle for unilateral rupture earthquake. In direction B, there is no consistent pattern with increasing of the takeoff angle between the rupture and the seismic station.

The rupture during a bilateral earthquake symmetrically propagates in opposite directions, so the equation for a unilateral rupture earthquake can be changed to fit the bilateral rupture earthquake:

$$\tau(\theta) = \frac{L}{v_r} + \frac{L}{c} \times |\cos\theta|$$
$$= \frac{L}{v_r}\left(1 + \frac{v_r}{c} \times |\cos\theta|\right)$$
$$= a\left(1 + \frac{v_r}{\alpha} \times |\cos\theta|\right)$$

Based on the rupture duration show on each seismogram, we investigate the rupture directivity instead of measuring the actual rupture duration of each intermediate-depth earthquake. The rupture durations shown on seismograms recorded at takeoff angles θ_i and θ_j (θ_i is the angle between the direction of rupture propagating and the takeoff vector to the station I, just as θ_j is for station j) are related by the stretching factor S_{ij}, where $\tau(\theta_i) = S_{ij}\,\tau(\theta_j)$. For a unilateral rupture event, the stretching factor is

$$S_{ij} = \frac{1 - \frac{v_r}{\alpha}\cos\theta_i}{1 - \frac{v_r}{\alpha}\cos\theta_j}$$

If $S_{ij} > 1$, the rupture duration is longer at station i than at station j; if $S_{ij} < 1$, the rupture duration is longer at station j than at station i. Also, if $S_{ij} = 1$, the rupture duration recorded at station i and j are the same (Figure 4). We estimate the stretching factor by cross-correlating different time offsets with different stretching factors between each station, which can help us to analyze the distribution of differential rupture durations over the focal sphere.

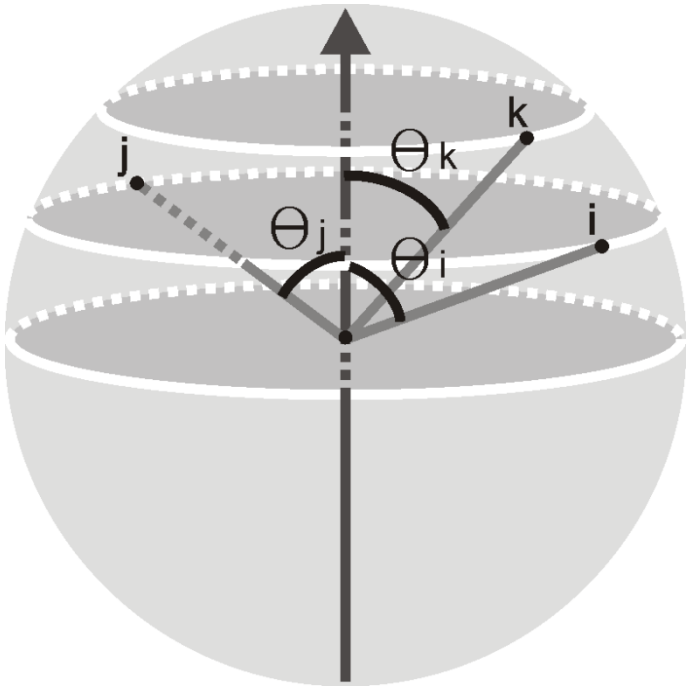

Figure 4: An ideal model for a unilateral earthquake rupture and three seismic stations deployed on the surface of the Earth. The gray arrow indicates the direction of the rupture in the sphere. Here we use i, j, and k to represent the seismic station at different locations with its takeoff angle θ_i, θ_j, and θ_k, separately. The rupture durations shown on seismograms recorded at takeoff angles θ_i, θ_j, and θ_k are related by the stretching factor S_{ij}, where $\tau(\theta_i) = S_{ij}\,\tau(\theta_j)$. If $S_{ij} > 1$, the rupture duration recorded at station k is longer than station i, which makes the stretching factor S_{ki} (or S_{ij}) > 1. Also, the apparent rupture duration recorded at station i and j are the same, which makes the stretching factor $S_{ij} = 1$.

The standard cross-correlation technique was developed by VanDecar and Crosson (1990) and extended by Warren and Silver (2006) by adding the stretching factor to measure the differential rupture durations of P-wave arrivals between each pair of seismograms.

We distinguished the rupture direction by running the semi-automated program developed by Warren and Silver (2006), which applies each step described above. Subsequently, we compared the results obtained for each nodal plane of the double-couple focal mechanism acquired from the Global CMT catalog.

For each earthquake analyzed, we used a grid search method to determine the best-fitting rupture vector. We search rupture vectors over the entire focal sphere and, for each candidate rupture vector, we search over rupture velocities between 0% and 80% of alpha. For each candidate rupture vector and rupture velocity, we calculate the root mean square (RMS) misfit M as follows:

$$M\left(\hat{v}, \frac{v_r}{\alpha}\right) = \sqrt{\frac{1}{m}\sum_{i=1}^{N-1}\sum_{j=i+1}^{N}\left[S_{ij}^{measured} - S_{ij}^{predicted}\right]^2}$$

where $\hat{v}$ is the unit vector at rupture velocity v_r, N is the number of seismic stations that recorded signals for the earthquake, and m is the number of measured stretching factors for each earthquake. Since we use every possible pair of stations to measure any possible stretching factor for each earthquake, we will have $m \leq N(N-1)/2$ measured stretching factors. The range of the misfit is between 0.0 and 1.0. The smaller the misfit, the better the rupture model can explain the observed signal duration. For each candidate rupture direction, the misfit and corresponding rupture

velocity are recorded. The lowest misfit values for each nodal plane are compared, and the plane with the lower misfit is identified as the rupture plane.

To increase confidence in the rupture vector that has been determined, we perform bootstrap resampling to estimate the error in the determined rupture direction. In this step, the analysis was run 1000 times with randomly-resampled subsets of the seismic data and, for each iteration, the best-fitting rupture vector was recorded. Confidence regions for the rupture direction then are drawn at 80% and 95% confidence levels on the sphere by considering the distribution of rupture directions. The 95% confidence region should only overlap one nodal plane for that plane to be identified as the rupture plane for the earthquake.

Synthetic data sets allow us to test whether the determined rupture vector can be identified or if the station distribution results in some kind of bias. For earthquakes with an identified fault plane, the misfit of the actual rupture plane should be lower than the misfit for the auxiliary nodal plane. We input the estimated seismic parameters for each earthquake, such as rupture velocity, the rupture duration, and the rupture vector, back into the directivity analysis to build up the synthetic seismograms for each earthquake. The synthetics must show observable directivity on the seismogram. Furthermore, all of the synthetic criteria must match the criteria of the real data. Afterward, we can use the distribution of differential rupture durations to distinguish the rupture direction for unilateral and bilateral rupture earthquakes.

3.3 Data Selection

The Pamir-Hindu Kush seismic zone is characterized by a high concentration of intermediate-depth earthquakes. In order to understand the physical mechanism of intermediate-depth earthquakes in this region, we chose earthquakes with moment magnitudes (Mw) > 5.5 that occurred in the region between latitude 35°N–40°N and longitude 69°E–77°E, and depths from 60 to 250 km for the 1990 to 2009 time period. In total, there are 52 earthquakes that fit these parameters (Figure 5, See Appendix A for Table A1-A2).

For each earthquake, we selected P-wave arrivals recorded by broadband seismometers located at distances between 0° and 95° from the epicenters to study the directivity. These parameters were chosen to make sure the P-wave arrivals for each earthquake would not be mixed up by other seismic phases, and to provide a good signal distribution of the seismic data. We used the vertical-component of each seismogram. Data were obtained from Incorporated Research Institutions for Seismology (IRIS) archive. The instrument response was removed to make displacement seismograms. The resultant vertical component seismograms are used for the analysis.

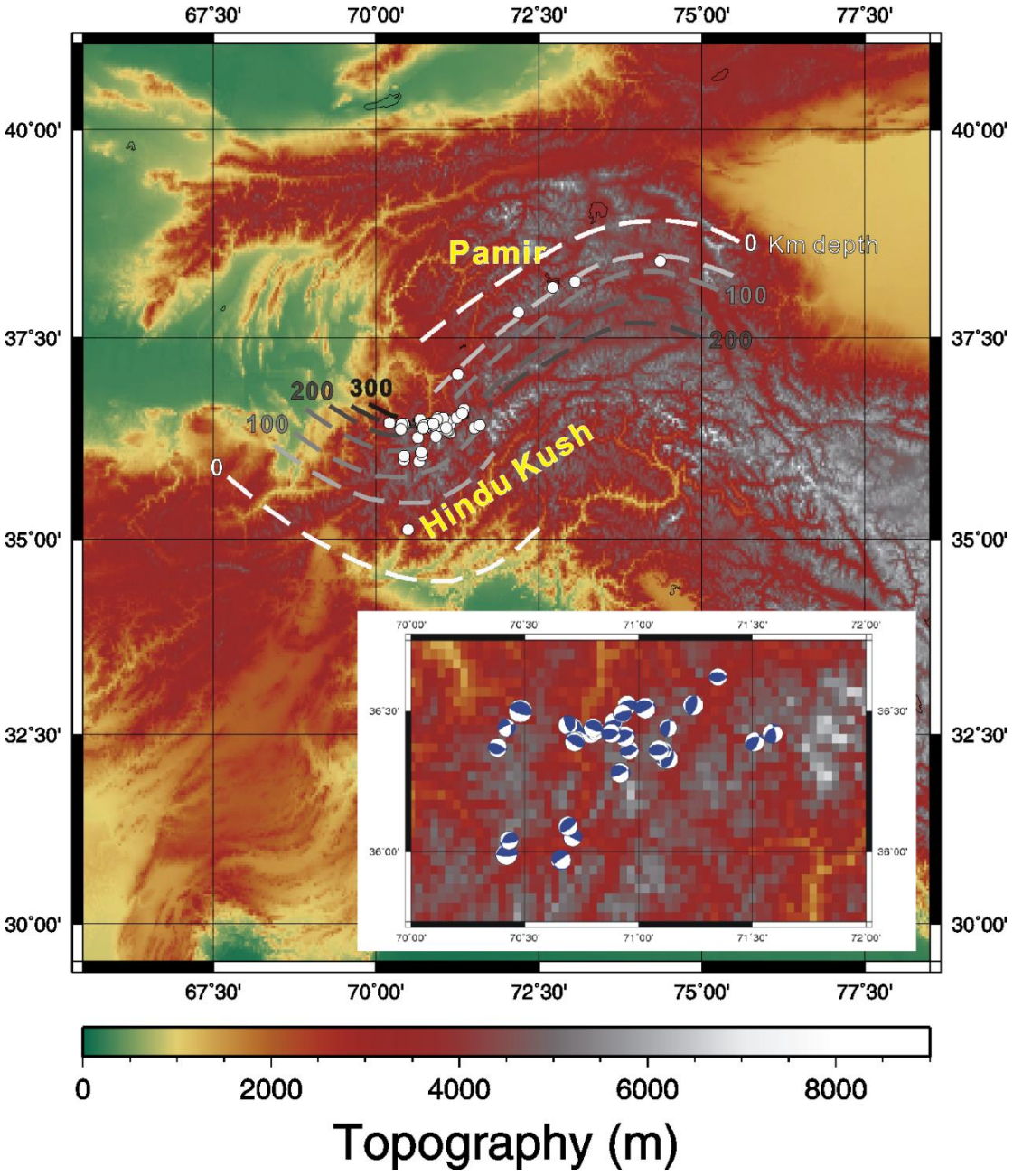

Figure 5: Slab contours and distribution of the 52 intermediate-depth earthquakes (white dots) for the 1990 to 2009 time period used in this study. These earthquakes with magnitudes (Mw) > 5.5 occurred in the region between latitude 35°N–40°N and longitude 69°E–77°E, and depths from 60 to 250 km. Dashed lines represent the slab contours (Gudmundsson and Sambridge, 1998) of the subducted slab(s) in different depths. The inset plot shows focal mechanisms of earthquakes in the Hindu Kush region.

Chapter 4. Results

Overall, there were 52 intermediate-depth earthquakes with moment magnitudes (Mw) $\geq$ 5.5 that occurred between 1990 and 2009 in the Pamir-Hindu Kush seismic zone (Figure 5). Among the 52 intermediate-depth earthquakes analyzed, we observed that 13 earthquakes showed directivity (Please see Appendix A and B for more details). For earthquakes that show directivity, the rupture duration increases as the angle between the directions of rupture propagation and the take-off vector to the station increases (Figure 3(b)). Almost all of the earthquakes with observable directivity have Mw > 6, except for one earthquake with Mw 5.5. For the remaining 39 earthquakes, we did not observe directivity (Appendix A: Table A2).

4.1 Ruptures on the North-dipping Plane

We observed that two of the earthquakes with directivity have their rupture propagation on the north-dipping fault plane (Appendix A: Table A1). The two earthquakes are the 31 January 1991 earthquake (Mw 6.9, depth 118 km) and the 13 May 1997 earthquake (Mw 6.5, depth 196 km).

For the 13 May 1997 earthquake (Mw 6.5, depth 96 km), the rupture duration increases as the angle between the station and the rupture vector increases (Figure 6; Appendix B: Figure B19-B21). The north-dipping fault plane is more likely the actual rupture plane since the north-dipping fault plane (nodal plane (1)) provides lower misfit than the southeast-dipping fault plane (nodal plane (2)) (Appendix A: Table A1). Azimuth of the rupture direction is ~320° (NW) on the north-dipping nodal plane.

Moreover, the 95% confidence rupture vector region covered only the north-dipping plane for this earthquake, which supports that the north-dipping plane is the rupture plane. In order to see if the rupture vector and inferred rupture plane estimated are reliable, we also make the synthetic model to see if we can recover the real data. Our synthetic model for the north-dipping nodal plane can replicate the rupture pattern seen for the earthquake than the southeast-dipping nodal plane, so we can identify the north-dipping nodal plane as the fault plane.

For the 31 January 1991 earthquake with observable directivity, we observed that there are three sub-events during this earthquake (Figure 7; Appendix B: Figure B4). As shown in Table A1, the bootstrap results for this earthquake provides lower misfit for the north-dipping fault plane (nodal plane (1)) than for the south-dipping fault plane (nodal plane (2)). The rupture azimuth is ~320° (NW) on the north-dipping nodal plane. The bootstrap-resampling result, however, shows that the 95% confidence rupture vector region (Figure 7; Appendix B: Figure B4-B6) covered rupture propagation on both synthetic planes.

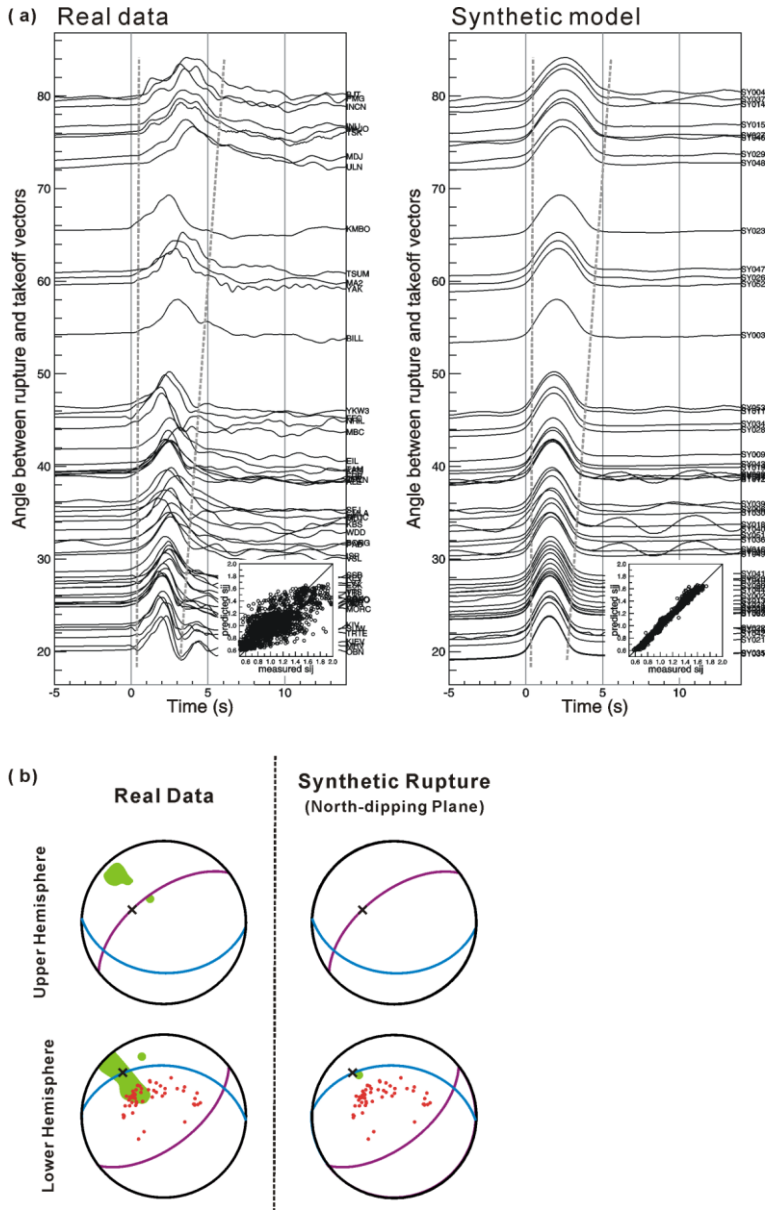

Figure 6: Seismograms of the 13th May 1997 earthquake (Mw 6.5, 196 km depth) with rupture propagation on the north-dipping plane. (a) The synthetic seismograms recovered the rupture direction perfectly for this earthquake. We can also see directivity in this earthquake. (b) The azimuth of its rupture direction is ~320° (NW) on the north-dipping nodal plane. Orientation of the 95% confidence rupture vector region covered on the synthetic north-dipping plane but not on the synthetic southeast-dipping plane. The coherent increase in the rupture duration with increasing angle from the rupture vector, and the match to synthetic rupture all show the north-dipping nodal plane is the fault plane. Thus, we identify the north-dipping nodal plane as the fault plane for this earthquake.

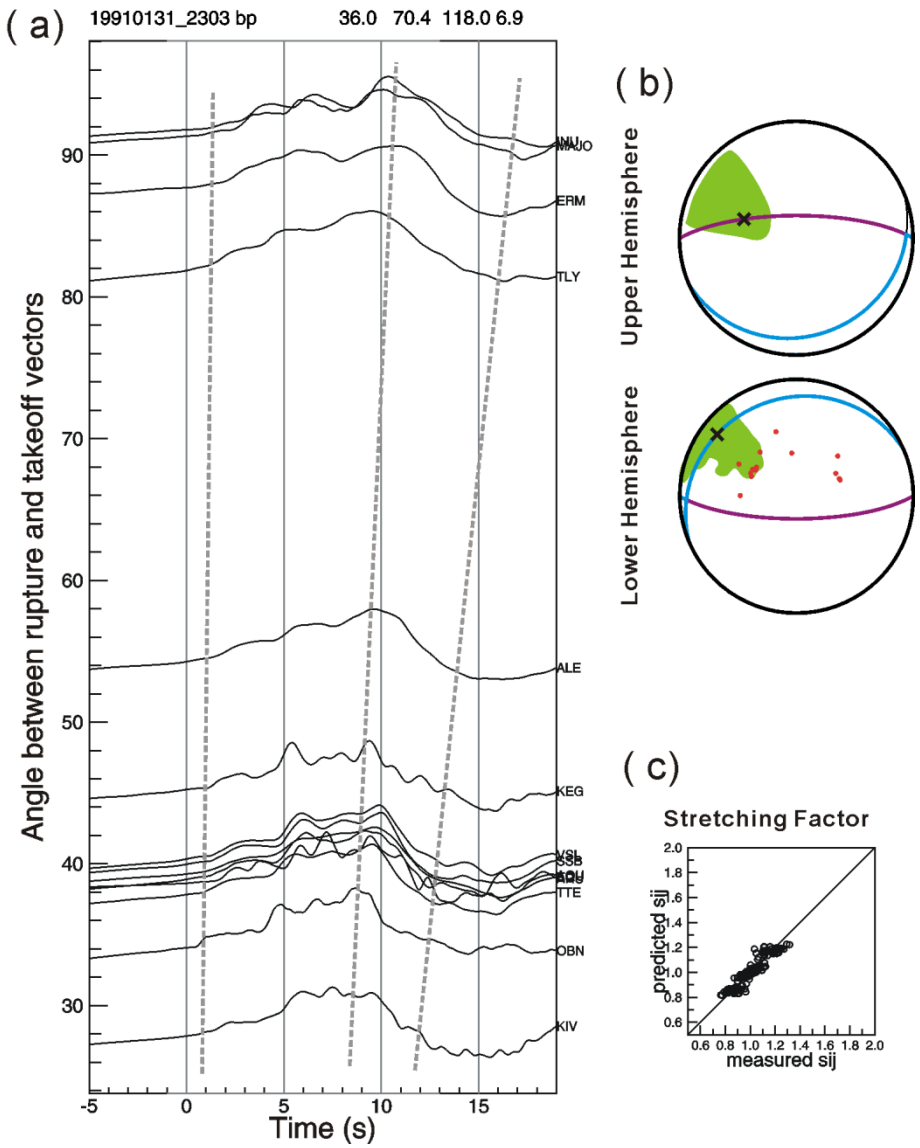

Figure 7: The 31 January 1991 23:03:33.67 earthquake (Mw 6.9, depth 118 km). As shown in figure (a), overall, there are three sub-events in this earthquake. The rupture duration increases as the angle between the direction of rupture propagation and the take-off vector to the station increases. (b) The azimuth of its rupture direction is ~320° (NW) on the north-dipping nodal plane (Appendix A: Table A1), even though the 95% confidence region (green) overlaps two nodal planes. (c) The relation of the measured and predicted stretching factors. The measured stretching factors are proportional to the predicted stretching factors.

4.2 Ruptures on the South-dipping Plane

We observed that the 13 July 1990 earthquake (Mw 6.4, depth 216 km) has its rupture propagation on the south-dipping fault plane. As shown in Table A1, the bootstrap results of the 13 July 1990 earthquake provides lower misfit for the south-dipping fault plane (nodal plane (2)) than for the north-dipping fault plane (nodal plane (1)). The azimuth of its rupture direction is ~270° (SW) on the south-dipping nodal plane. Furthermore, the bootstrap resampling result for this earthquake shows that the rupture direction on the south-dipping (purple) nodal plane can be better covered by the 95% confidence region than the north-dipping nodal plane (Figure 8). However, the station distribution is not good for this earthquake, which makes the result of resampling unable to recover the real data.

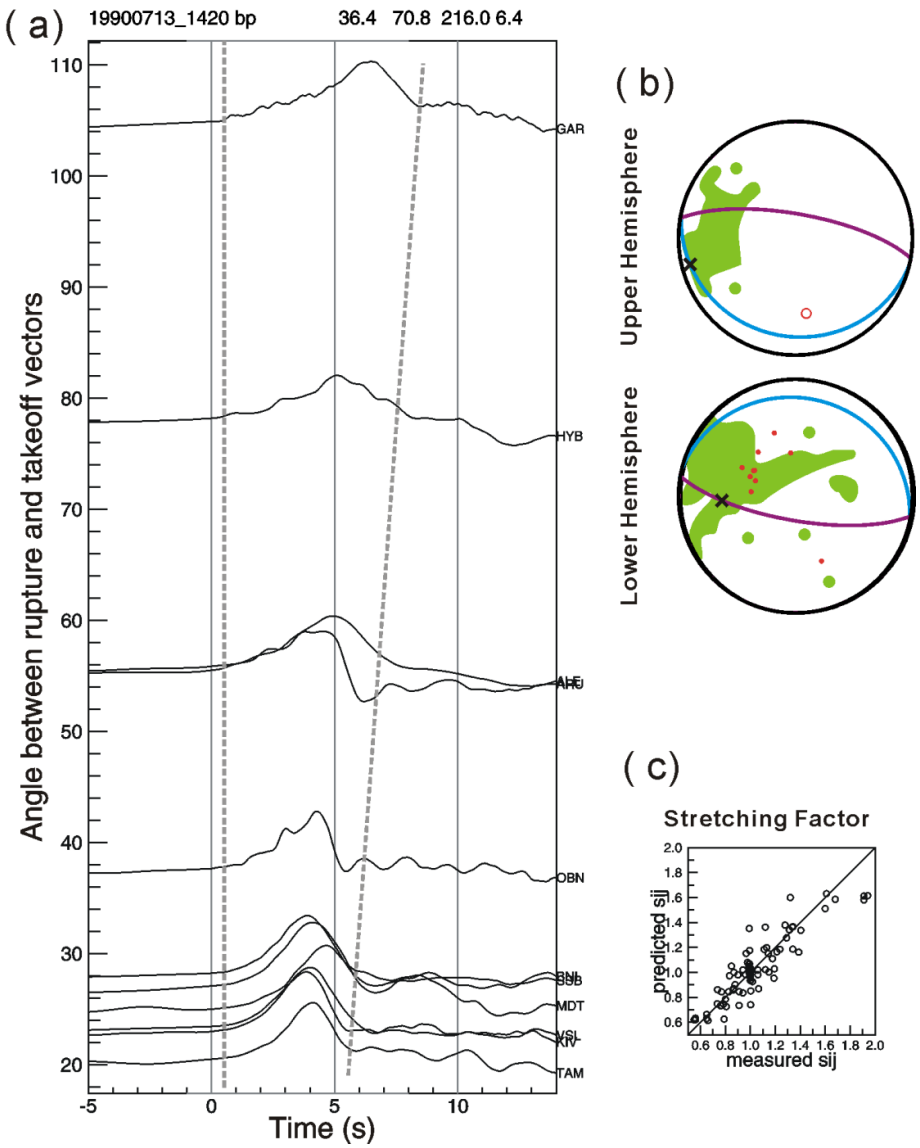

Figure 8: The 13 July 1990 14:20:43.47 earthquake (Mw 6.4, depth 216 km). (a) The seismograms of the real data shows that the rupture duration increases as the angle between the directions of rupture propagation and the take-off vector to the station increases. (b) In Table A1, the azimuth of its rupture direction is ~270° (SW) on the south-dipping nodal plane since the south-dipping nodal plane has lower misfit that the north-dipping nodal plane. Thus, we identify the south-dipping nodal plane as the fault plane for this earthquake. In the bootstrap resampling method, however, the 95% confidence region covers both nodal planes. (c) The measured stretching factors are proportional to the predicted stretching factors.

4.3 Rupture Propagation towards the Nodal Plane Intersection

Among the 13 earthquakes that show directivity, we found that six of them have their rupture propagating towards the intersection of the nodal planes (Appendix A: Table A1). These earthquakes occurred on 9 August 1993 (Mw 6.3, 204 km depth), 30 June 1994 (Mw 6.3, depth 226 km), 12 May 2000 (Mw 6.3, depth 107 km), 23 November 2011 (Mw 6.1, depth 106 km), 3 March 2002 (Mw 7.4, depth 225 km), and 12 December 2005 (Mw 6.5, depth 224 km) (Please see Appendix B for more details about the seismograms of each events.)

Station distributions for these 6 intermediate-depth earthquakes allow good resolution of the rupture vector for rupture on either nodal plane. We also computed synthetic seismograms for each earthquake and reran the analysis to test resolution of the rupture vector. The 95% confidence region for the rupture vector covered the rupture directions on both possible fault planes. As a result, the actual rupture plane cannot be identified.

4.4 Earthquakes with Rupture Directions that cannot be interpreted

Among the 13 earthquakes that show directivity, we cannot determine the rupture plane for the 14 July 1991 earthquake (Mw 6.4, depth 212 km), the 25 October 1994 earthquake (Mw 6.0, depth 238 km), the 14 February 1998 (Mw 5.5, depth 218 km), and the 22 October 2009 earthquake (Mw 6.2, depth 185 km), even though their ruptures are not toward the intersection of the nodal planes (Appendix A: Table A1). The results of bootstrap resampling for the 95% confidence rupture regions cannot provide us information on the rupture direction. The confidence region may overlap

both nodal planes, or may be well constrained in azimuth but not plunge. We found that the magnitudes (Mw) of these earthquakes are ≤ 6.0, the station distribution for these earthquakes are not good, or the misfits of these earthquakes are ≥ 0.8.

In addition, there are 39 earthquakes without observable directivity (Appendix A: Table A2). The apparent rupture duration does not increase as the angle between the directions of rupture propagation and the take-off vector to the station increases. Since our method is based on the source finiteness, we cannot identify the behavior of these earthquakes. The lack of observed directivity could mean that the rupture process was effectively a point source for these earthquakes.

Chapter 5. Discussion

In this study, we analyzed intermediate-depth earthquakes in the Pamir-Hindu Kush region with magnitudes (Mw) $\geq$ 5.5. These large magnitude events were selected to ensure that the P-wave arrivals would not be contaminated by other seismic phases and that the seismic waves would be well recorded by many seismic stations at teleseismic distances. We identified 52 intermediate-depth earthquakes within the 1990-2009 time period. Most of the earthquakes are located in the Hindu-Kush seismic zone, which suggests that seismicity in the Pamir region is not as active as in the Hindu Kush region (Figure 5). Among the 52 earthquakes chosen, only one quarter of them show observable directivity.

5.1 Earthquakes that Show Directivity

5.1.1 Focal Mechanisms

In Appendix B, we present 13 focal mechanisms of the intermediate-depth earthquakes that show observable directivity (Appendix A: Table A1). As shown in Figure 9, these earthquakes are all located within the Indian slab. There are three earthquakes that located shallower than 150 km depth. We did not observe any kind of trend for these earthquakes. On the other hand, we did notice that some of the earthquakes have similar orientations of their fault planes. The first cluster of earthquakes consists of the 13 July 1990 earthquake (Mw 6.4, 216 km depth), the 9 August, 1993 earthquake (Mw 6.3, 204 km depth), and the 3 March 2002 earthquake (Mw7.4, 225 km) (Appendix A: Table A1, and Figure 10). In cluster I, earthquakes are located in the region of latitude ~36.5°N, longitude ~70.5°E, and depth of ~210 km.

The strike, dip, rake, and rupture velocity of the earthquakes are similar. However, the azimuth and dip of the best fitting rupture directions, indicated by the “x” in Figure 10, differ.

(a)

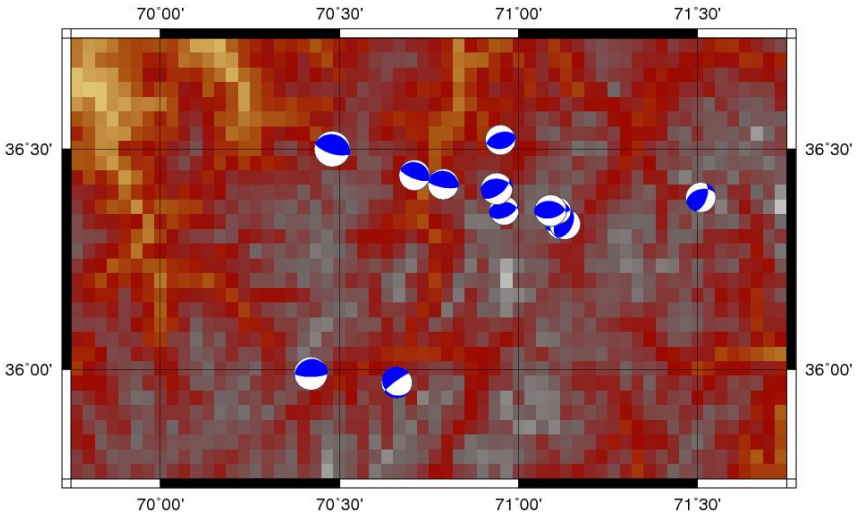

(b)

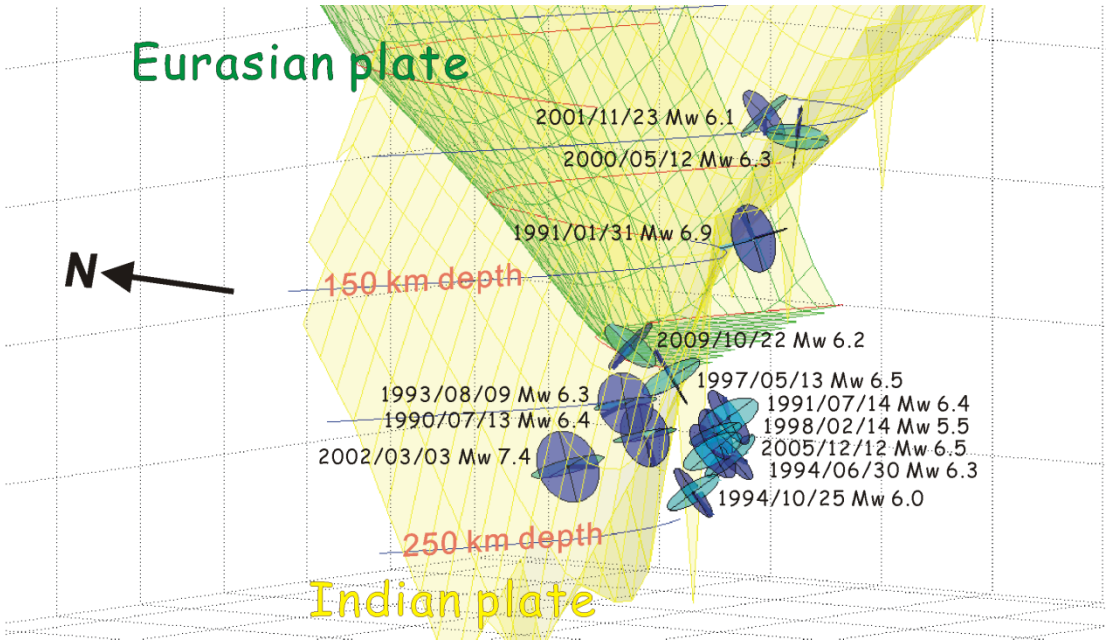

Figure 9: Relative locations and focal mechanisms of the 13 intermediate-depth earthquakes (Appendix A: Table A1) that show observable directivity and the subducted slabs. Each focal mechanism represents an earthquake. (a) Map view of the focal mechanisms. (b) Relative location of the focal mechanisms in a 3-D view. The green and yellow grids show the slab contours of the Eurasian slab and the Indian slab, respectively (Gudmundsson and Sambridge, 1998). The cyan and deep blue colored planes indicate the two possible fault planes for each earthquake.

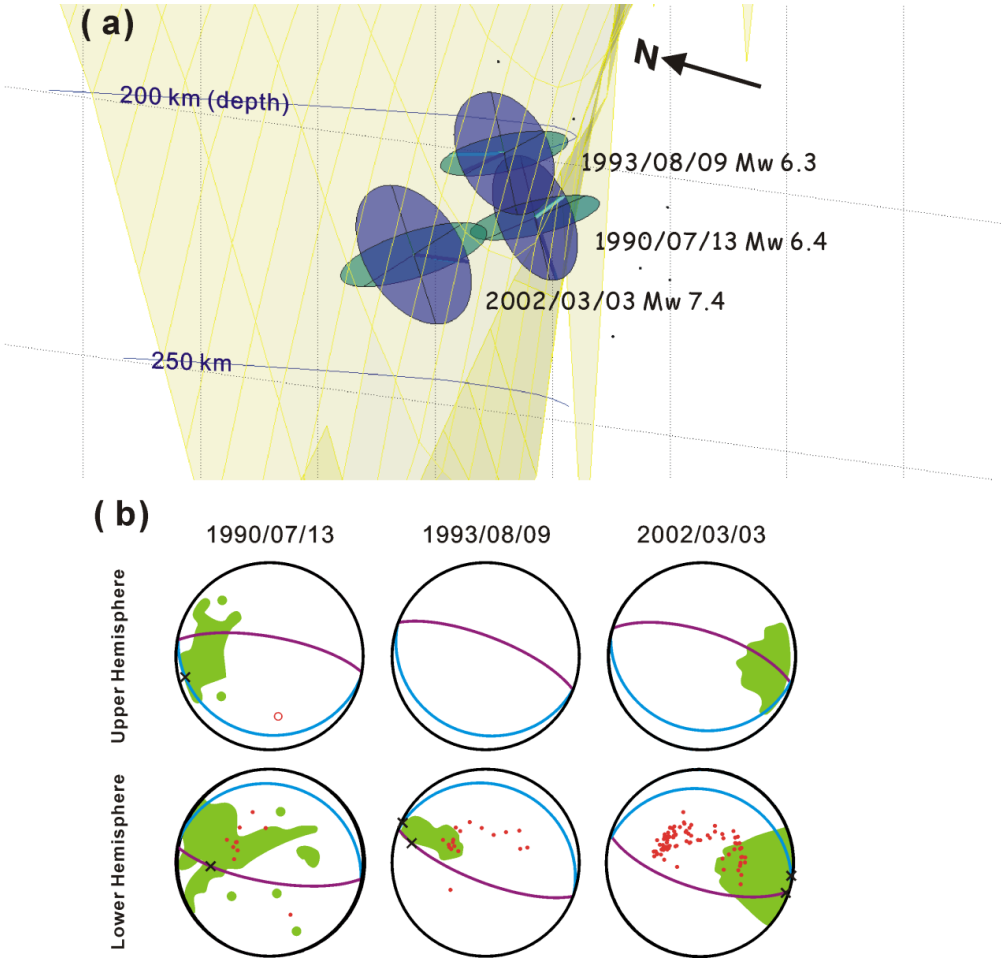

Figure 10: Focal mechanisms of earthquakes in cluster I. (a) A closer view of the focal spheres in cluster I, which was shown in Figure 9. The orientations of nodal planes for these earthquakes are similar. The cyan color planes dip northward, and the deep blue planes dip southward. The cyan and deep blue color lines point out the possible rupture direction on the cyan and deep blue fault planes, accordingly. (b) Results of the bootstrap resampling for earthquakes in cluster I. Black crosses indicate the best fitting rupture directions on the two possible nodal planes for each earthquake. Green color indicates the 95% confidence region for the possible rupture directions. We observed that the ruptures point into the intersection of nodal planes for these three earthquakes.

The second cluster is composed of the 14 July 1991 earthquake (Mw 6.4, 212 km depth), the 25 October 1994 earthquake (Mw 6.0, 238 km depth), the 14 February 1998 (Mw 5.5, 218 km depth), and the 12 May 2000 earthquake (Mw 6.3, 107 km depth) (Figure 11). In cluster II, the earthquakes are located in the region of latitude ~36°N, longitude ~71°E, and depth between 100 and 240 km. In cluster II, the strike, dip, rake, and rupture velocity are slightly different. We note that the orientation of the fault planes varies slightly with the shape of the Indian slab.

Our observation agrees with Lister et al. (2008) study. They found that there is no obvious orientation for the earthquakes in the depth between 75 and 180 km. Furthermore, they observed that earthquakes at the depths between 180 and 280 km show obvious orientation clusters, which is similar to our observation. The two clusters of earthquakes with well-ordered orientations in our study are located between 180 and 240 km depth. Lister et al.(2008) suggested that the slab stretches and breaks off to form a boudinage-shaped subducting slab, and that the intermediate-depth earthquakes may happen in pre-existing weak zones of the slab.

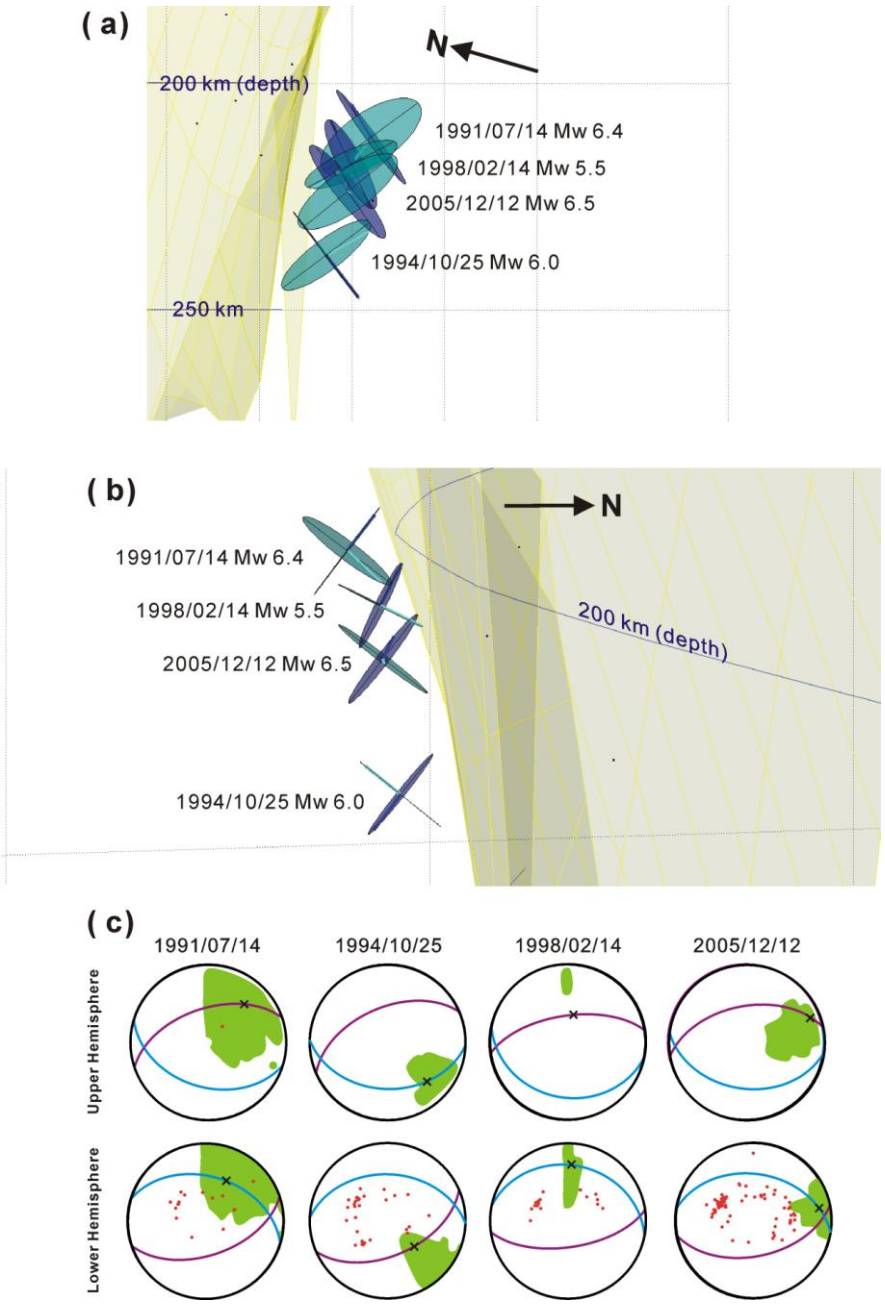

Figure 11: Close view of the focal spheres in cluster II, which was shown in Figure 9, and the focal mechanisms for earthquakes in cluster II. (a) and (b) show the same cluster of earthquakes from different perspectives. (c) Results of the bootstrap resampling for earthquakes in cluster II. Black crosses indicate the best fitting rupture directions on the two possible nodal planes for each earthquake. The green color indicates the 95% confidence region for the rupture direction. The orientations of rupture planes for these earthquakes are identical. We observe that the orientations of the fault planes migrate with the shape of Indian slab.

5.1.2 Rupture Directions

Rupture towards the nodal plane null axis is a common feature of intermediate-depth earthquakes in the Pamir-Hindu Kush region. Among the 13 earthquakes that show directivity, six of them have their rupture directions pointing into the intersection of the nodal planes, two of the earthquakes have their rupture direction as ~320° (NW) on a north-dipping fault plane, and one has its rupture direction as ~270° (W) on the steep south-dipping fault plane. We found that almost all of the earthquakes that show directivity (except the 14 February 1998 earthquake) have magnitudes (Mw) > 6. However, for the remaining four earthquakes it is hard to determine the rupture plane because the rupture dip is not well resolved.

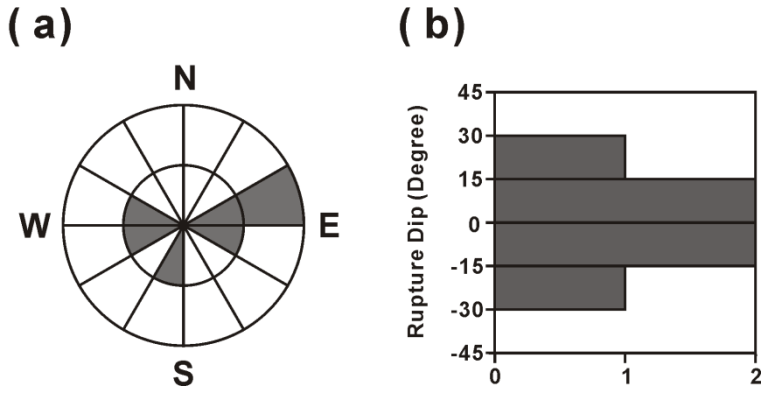

Figure 12: Histograms showing the distribution of rupture propagation for the six earthquakes with their ruptures propagating toward the intersection of the nodal planes (Appendix A: Table A1). For each earthquake, we average the azimuth and dip for the best fitting rupture vector on each possible fault plane. (a) Azimuth of rupture propagation. (b) Dip of rupture propagation. We observed that the dips of rupture propagation tend to be horizontal for the earthquakes with their ruptures toward the intersection of the nodal planes.

In figure 12, we plot histograms to show the dip of rupture propagation for the six earthquakes with their rupture directions toward the intersection of the nodal planes. We observed that the dips of rupture propagation tend to be horizontal for the earthquakes with their rupture towards the intersection of the nodal planes.

5.1.3 3 March 2002 (Mw 7.4, Depth 225 km) Earthquake

The 3 March 2002 12:08:19.74 earthquake (36.50°N, 70.48°E, 225 km depth, Mw 7.4) is a special event (Appendix B: Figures B31-B33). It was preceded by 12 seconds by another earthquake (3 March 2002 12:08:07.81, 36.43°N, 70.44°E, 209 km depth, Mw 6.3). The origin times of these two earthquakes are so close so that the amplitude of the Mw 6.3 earthquake may be ignored easily because of the Mw 7.4 earthquake. We used several ways to analyze these two earthquakes. We considered these two earthquakes as one earthquake with several subevents. We studied these two earthquakes together, and the result shows the rupture direction of this "one" earthquake is towards the intersection of the nodal planes (Figure 14).

Kiser et al.'s study (2011) suggested that a large earthquake occurred on 3 March 2002 12:08:19.74 (Mw 7.4) with two strong subevents separated by 75 km in depth (225 and 300 km depth) and 8.5 seconds in time. They suggested that there are two horizontal fault planes separated by 75 km, not just one fault plane for this earthquake. However, their result is dissimilar with our result. If we put their result into our study, we would say the rupture direction of the Mw 7.4 earthquake is vertical. Afterwards, the fault plane is not horizontal but vertical (Figure 13). On the other hand, we observe two subevents for the Mw 7.4 earthquake, which means the two fault planes

studied by Kiser et al. are only related to the Mw 7.4 earthquake but not the Mw 6.3 earthquake. So far, we cannot study the rupture behavior of the Mw 6.3 earthquake. It is still not clear that if the Mw 6.3 earthquake is the foreshock of the Mw 7.4 earthquake, and whether there is any relation between these two earthquakes.

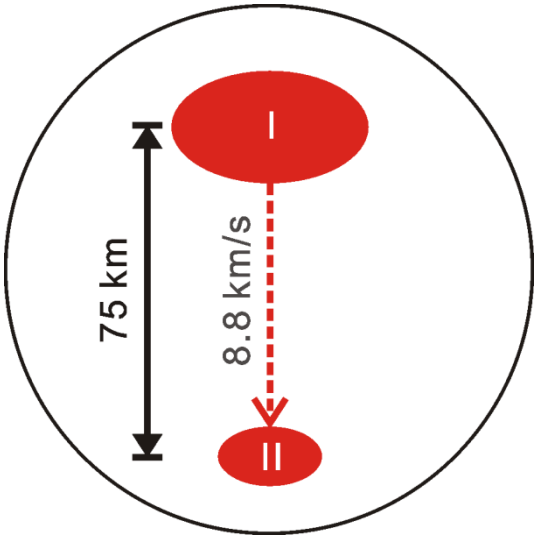

Figure 13: A simple cartoon shows a vertical view of the relative location of the two subevents of the 3 March 2002 Mw 7.4 earthquake in the Kiser et al. (2011) study. Red ovals show the relative positions of subevent I and subevent II, which were separated by 75 km. During the earthquake, subevent II occurred 8.5 s after the occurrence of subevent I. The red dashed line indicates the possible rupture direction for this earthquake in our interpretation. Based on their study, the rupture plane of this earthquake tends to be vertical rather than horizontal.

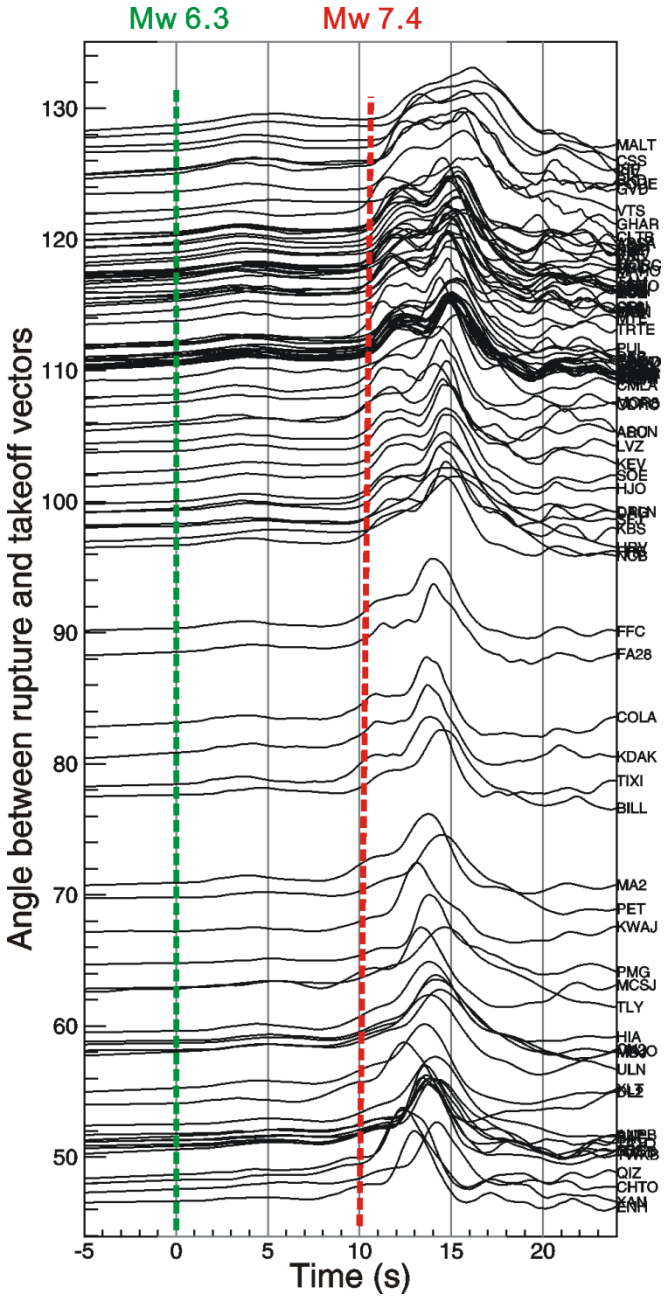

Figure 14: The seismograms of 3 March 2002 12:08:07.81 (Mw 6.3, depth 216 km) and 12:08:19.74 (Mw 7.4, depth 225 km) earthquakes. The Mw 7.4 event was preceded by 12 seconds by the Mw 6.3 event. The origin times of these two earthquakes are so close so that the amplitude of the Mw 6.3 earthquake may be ignored easily because of the Mw 7.4 earthquake. We use the green and red dashed lines, respectively, to indicate the first motion for these two earthquakes. We can directly observe two subevents for the Mw 7.4 earthquake.

5.2 Earthquakes without Directivity

For the earthquakes that didn't show directivity, the rupture durations do not increase with the increasing angle between the direction of rupture propagation and the station, takeoff vector. This could mean that the rupture process was stationary and acted as a point source. Among the 39 earthquakes without directivity (Appendix A: Table A2), 23 have magnitudes less than 6. For the rest of the earthquakes with Mw $\leq$ 6.0, most do not have good data quality. Taking the coverage of seismic stations into account, there were only seven intermediate-depth earthquakes that occurred in the Hindu Kush area between 1990 and 2009 which have good station coverage and observable directivity. It is not easy to find large intermediate-depth earthquakes with good station distributions, which makes the number of analyzable earthquakes small. The reason why we did not observe directivity for earthquakes with Mw > 6.0 is because there was a poor distribution of stations recording the event, or the signal to noise ratio is too small for the remaining events, or a bigger earthquake contaminated the seismic signal.

Chapter 6. Conclusions

We interpreted 52 intermediate-depth earthquakes between 1990 and 2009 and found that there are 13 earthquakes that show observable directivity. All earthquakes that show directivity are located in the western part of the Pamir-Hindu Kush region. Six of the earthquakes that show directivity have their rupture directions toward the intersection of nodal planes, so it is hard to tell which of the two nodal planes is the real rupture plane. We found that the dip of the rupture propagation of these six earthquakes tends to be horizontal. However, we still need to use another method to map the distribution of slip over the fault plane and therefore identify the fault plane. We classify the earthquakes with observable directivity at the depths between 180 and 240 km into two clusters based on the orientation of the fault planes. Earthquakes in cluster I have similar rupture behavior. The earthquakes in cluster II have their fault planes follow the shape of descending Indian slab. For the earthquakes that do not show directivity, it might suggest that the rupture process during this earthquake was stationary or, equivalently, that the earthquake was a point source.

Appendix A

Table A1: Earthquake rupture parameters for the 13 earthquakes that show directivity.

Date yyyy/mm/dd	Time (UTC) hh:mm:ss	Lat (°N)	Lon (°E)	Depth (km)	M_W	NP (No.)	Misfit	Strike (deg)	Dip (deg)	Rake (deg)	$\frac{Vr}{\alpha}$	Azimuth (deg)	Dip (deg)	N
1990/07/13	14:20:43.47	36.42	70.79	216	6.4	(1)	0.73	283	17	93	0.56±0.21	256	8	11
						(2)	**0.44**	**100**	**73**	**89**	**0.42±0.13**	**267**	**-37**	
1991/01/31	23:03:33.67	35.99	70.42	142	6.9	**(1)**	**0.36**	**247**	**17**	**68**	**0.20±0.03**	**308**	**-15**	14
						(2)	0.39	90	74	97	0.29±0.09	290	51	
1991/07/14	09:09:11.91	36.33	71.12	212	6.4	(1)	0.85	287	42	118	0.40±0.15	27	-41	16
						(2)	0.85	72	54	68	0.41±0.19	43	33	
*1993/08/09	11:38:30.53	36.44	70.71	204	6.3	(1)	0.31	290	17	89	0.51±0.05	296	-2	18
						(2)	0.31	111	73	90	0.47±0.05	285	-19	
*1994/06/30	09:23:21.35	36.33	71.13	226	6.3	(1)	0.73	216	40	97	0.38±0.08	199	14	47
						(2)	0.73	27	51	84	0.32±0.04	201	-7	
1994/10/25	00:54:34.30	36.36	70.96	238	6.0	(1)	0.64	272	40	110	0.61±0.16	310	-27	35
						(2)	0.67	67	53	74	0.42±0.08	314	51	
1997/05/13	14:13:45.74	36.41	70.94	196	6.5	**(1)**	**0.86**	**273**	**38**	**124**	**0.29±0.01**	**302**	**-20**	51
						(2)	0.87	52	60	66	0.65±0.06	292	56	
1998/02/14	00:08:07.80	36.36	71.11	218	5.5	(1)	0.72	281	29	107	0.59±0.12	3	-28	16
						(2)	0.88	82	63	81	0.77±0.11	11	61	
*2000/05/12	23:10:29.98	35.97	70.66	107	6.3	(1)	0.64	118	18	-27	0.51±0.12	110	3	24
						(2)	0.77	233	82	-106	0.80±0.03	65	55	

Table A1: Continued

Date yyyy/mm/dd	Time (UTC) hh:mm:ss	Lat (°N)	Lon (°E)	Depth (km)	M_W	NP (No.)	Misfit	Strike (deg)	Dip (deg)	Rake (deg)	$\frac{Vr}{\alpha}$	Azimuth (deg)	Dip (deg)	N
*2001/11/23	20:43:03.55	36.39	71.51	106	6.1	(1)	0.71	254	45	133	0.44±0.11	65	-9	32
						(2)	0.76	22	59	56	0.44±0.11	57	-44	
*2002/03/03	12:08:19.74	36.50	70.48	225	7.4	(1)	0.79	282	22	85	0.09±0.01	98	-2	127
						(2)	0.79	108	68	92	0.10±0.03	109	-3	
*2005/12/12	21:47:46.07	36.36	71.09	224	6.5	(1)	0.65	279	40	106	0.26±0.03	259	16	100
						(2)	0.64	80	52	77	0.31±0.08	249	-14	
2009/10/22	19:51:27.52	36.52	70.95	185	6.2	(1)	0.83	83	41	99	0.65±0.21	175	-41	11
						(2)	0.84	252	49	82	0.52±0.17	173	49	

UTC, Coordinated Universal Time; Lat, latitude; Lon, longitude; Mw, moment magnitude; NP, nodal planes;

Vr/α, rupture velocity divided by P wave velocity; N, number of stations

* Earthquakes with their rupture towards the intersection of the nodal planes

Table A2: Earthquake rupture parameters for the 39 earthquakes that do not show directivity.

Date yyyy/mm/dd	Time (UTC) hh:mm:ss	Lat (°N)	Lon (°E)	Depth (km)	M_W	NP (No.)	Misfit	Strike (deg)	Dip (deg)	Rake (deg)	$\frac{Vr}{\alpha}$	Azimuth (deg)	Dip (deg)	N	Note
1990/02/25	05:16:46.15	37.05	71.25	109	6.1	-	-	-	-	-	-	-	-	-	low signal-to-noise ratio
1990/05/15	14:25:20.69	36.04	70.43	113	5.9	(1)	0.74	216	36	48	0.67±0.14	315	-36	8	bad station coverage
						(2)	0.72	84	64	116	0.74±0.14	300	51		
1990/05/17	13:21:07.48	38.43	74.36	114	5.7	-	-	-	-	-	-	-	-	-	bad station coverage
1990/10/25	12:18:06.23	35.12	70.49	113	5.8	-	-	-	-	-	-	-	-	-	low signal-to-noise ratio
1991/02/23	17:19:47.14	36.27	70.64	154	5.5	-	-	-	-	-	-	-	-	-	low signal-to-noise ratio
1992/11/12	20:41:04;69	36.45	70.85	198	5.6	-	-	-	-	-	-	-	-	-	low signal-to-noise ratio
1992/12/04	11:36:36.20	37.81	72.19	120	5.8	-	-	-	-	-	-	-	-	-	low signal-to-noise ratio
1993/07/2	11:50:06.80	36.44	70.42	272	5.7	(1)	0.52	354	48	-154	0.78±0.09	112	-43	12	bad station coverage
						(2)	0.24	246	71	-45	0.59±0.19	37	-55		
1993/09/04	11:38:38.93	36.43	70.81	194	6.0	(1)	1.00	268	24	121	0.22±0.16	134	17	21	bad station coverage
						(2)	0.98	54	70	77	0.31±0.23	293	67		
1993/09/18	05:02:27.01	36.42	71.59	112	6.3	(1)	0.96	233	48	144	0.23±0.10	166	46	17	good station coverage
						(2)	0.94	349	64	48	0.31±0.18	156	-25		
1995/05/16	03:35:02.61	36.46	70.89	186	5.9	(1)	0.90	52	21	67	0.25±0.14	314	21	20	bad station coverage
						(2)	0.92	256	70	99	0.44±0.23	198	68		
1995/08/17	23:14:19.03	36.44	71.13	233	5.6	(1)	0.94	239	24	141	0.21±0.14	333	-24	17	bad station coverage
						(2)	0.92	5	75	71	0.50±0.25	320	70		
1995/10/18	09:30:38.50	36.43	70.39	222	6.3	-	-	-	-	-	-	-	-	-	low signal-to-noise ratio

Table A2: Continued

Date yyyy/mm/dd	Time (UTC) hh:mm:ss	Lat (°N)	Lon (°E)	Depth (km)	M_W	NP (No.)	Misfit	Strike (deg)	Dip (deg)	Rake (deg)	$\frac{Vr}{\alpha}$	Azimuth (deg)	Dip (deg)	N	Note
1995/12/25	03:19:44.91	36.45	70.21	228.2	5.6	-	-	-	-	-	-	-	-	11	low signal-to-noise ratio
1996/09/14	08:01:03.75	36.05	70.71	119	5.9	(1)	0.83	230	8	23	0.56±0.15	323	-8	10	bad station coverage
						(2)	0.94	118	87	97	0.61±0.21	296	-37		
1997/12/17	05:51:29.22	36.39	70.77	207	6.3	-	-	-	-	-	-	-	-	-	low signal-to-noise ratio
1998/02/20	12:18:06.23	36.48	71.09	235	6.4	-	-	-	-	-	-	-	-	-	low signal-to-noise ratio
1998/12/11	20:16:24.04	36.51	71.02	222	5.7	(1)	0.89	126	54	136	0.37±0.18	301	52	20	bad station coverage and low signal-to-noise ratio
						(2)	0.91	246	56	46	0.34±0.15	57	-13		
1999/06/21	17:37:27.18	36.39	70.71	230	5.5	-	-	-	-	-	-	-	-	-	low signal-to-noise ratio
1999/06/29	23:18:05.56	36.62	71.35	189	5.7	(1)	0.87	279	45	102	0.34±0.08	199	45	40	good station coverage
						(2)	0.89	81	46	78	0.52±0.20	208	-40		
1999/11/08	16:45:43.02	36.52	71.24	228	6.5	(1)	0.95	203	27	97	0.15±0.05	254	-21	65	good station coverage
						(2)	0.96	16	64	87	0.18±0.07	223	42		
2000/01/19	07:09:33.58	36.37	70.38	206	6.0	(1)	0.86	83	33	65	0.36±0.18	53	18	25	good station coverage but low signal-to-noise ratio
						(2)	0.98	293	60	106	0.39±0.20	86	-39		
2000/05/01	18:41:41.80	38.18	73.05	140	5.6	(1)	0.88	81	75	178	0.44±0.21	286	59	20	bad station distribution
						(2)	0.94	171	80	15	0.36±0.21	353	35		
2000/07/17	22:53:47.30	36.28	70.92	141	6.3	(1)	0.92	310	26	153	0.25±0.10	221	26	52	good station coverage
						(2)	0.91	64	79	67	0.54±0.25	170	-59		

Table A2: Continued

Date yyyy/mm/dd	Time (UTC) hh:mm:ss	Lat (°N)	Lon (°E)	Depth (km)	M_W	NP (No.)	Misfit	Strike (deg)	Dip (deg)	Rake (deg)	$\frac{Vr}{\alpha}$	Azimuth (deg)	Dip (deg)	N	Note
2001/02/25	02:21:59.59	36.42	70.88	202	6.2	(1)	0.88	60	49	57	0.29±0.10	83	-25	44	good station coverage
						(2)	0.88	285	51	122	0.31±0.10	94	-13		
2002/01/03	07:05:27.67	36.09	70.69	129	6.2	(1)	0.94	216	27	72	0.21±0.07	61	12	28	bad station coverage
						(2)	0.93	56	64	99	0.45±0.23	25	47		
2002/03/03	12:08:07.81	36.43	70.44	209	6.3	-	-	-	-	-	-	-	-	-	too close to the Mw 7.4 earthquake which occurred 12 seconds after this earthquake
2004/03/12	22:45:19.00	36.40	70.77	218	5.8	-	-	-	-	-	-	-	-	-	low signal-to-noise ratio
2004/04/05	21:24:04.00	36.51	71.03	187	6.6	(1)	0.90	290	28	139	0.32±0.12	354	-25	31	good station coverage
						(2)	0.99	58	72	68	0.48±0.26	334	58		
2004/08/10	01:47:32.81	36.44	70.80	207	6.0	(1)	0.93	277	20	74	0.30±0.15	302	-9	23	bad station coverage
						(2)	0.92	114	71	96	0.40±0.20	272	-47		
2005/02/25	23:04:04.02	38.11	72.71	114	5.7	(1)	0.89	343	45	-36	0.72±0.18	351	-7	17	bad station coverage
						(2)	0.91	100	66	-129	0.56±0.20	20	65		
2005/07/01	03:48:28.69	36.57	71.32	63	5.6	-	-	-	-	-	-	-	-	-	low signal-to-noise ratio
2005/07/23	14:40:25.01	36.39	70.72	209	5.5	-	-	-	-	-	-	-	-	-	low signal-to-noise ratio
2007/04/03	03:35:07.28	36.45	70.69	222	6.2	(1)	0.92	30	32	141	0.31±0.15	287	31	19	bad station coverage
						(2)	0.98	155	71	64	0.49±0.27	319	-37		

Table A2: Continued

Date yyyy/mm/dd	Time (UTC) hh:mm:ss	Lat (°N)	Lon (°E)	Depth (km)	M_W	NP (No.)	Misfit	Strike (deg)	Dip (deg)	Rake (deg)	$\frac{Vr}{\alpha}$	Azimuth (deg)	Dip (deg)	N	Note
2008/09/06	05:47:39.91	36.49	70.93	191	5.8	(1)	0.96	85	18	104	0.32±0.24	247	-6	11	bad station coverage
						(2)	0.81	250	72	85	0.68±0.15	21	-67		
2008/10/26	01:28:56.06	36.49	70.68	210	5.7	-	-	-	-	-	-	-	-	-	low signal-to-noise ratio
2008/12/29	03:37:41.03	36.39	71.07	151	5.8	-	-	-	-	-	-	-	-	-	low signal-to-noise ratio
2009/01/03	20:23:20.18	36.42	70.74	204	6.6	-	-	-	-	-	-	-	-	-	a bigger earthquake contaminated the signal
2009/01/04	23:12:59.29	36.44	70.88	186	5.7	-	-	-	-	-	-	-	-	-	low signal-to-noise ratio
2009/10/29	17:44:31.23	36.39	70.72	202	6.2	(1)	0.99	282	25	75	0.16±0.09	255	12	41	good station coverage
						(2)	0.99	119	66	97	0.43±0.25	238	-62		

UTC, Coordinated Universal Time; Lat, latitude; Lon, longitude; Mw, moment magnitude; NP, nodal planes; Vr/α, rupture velocity divided by P wave velocity; N, number of stations

Appendix B

The figures in this appendix show the results for all earthquakes that show directivity. For each earthquake there are three figures: one for the actual data set and one each for synthetics assuming rupture on each of the two nodal planes. In each figure, a) shows the projection of the upper (top) and lower (bottom) hemispheres of the focal mechanism. Blue and red triangles represent the best fitting rupture directions on the more horizontal and more vertical nodal planes, respectively. The dashed black line on each focal sphere shows the 95% confidence region for the possible rupture direction, and the solid black curve denotes the 80% confidence region. Open circles indicate seismic station locations as they relate to the hypocenter. Part b) shows the relation between predicted and measured stretching factors for horizontal (top) and vertical (bottom) nodal planes, separately. The more the measured stretching factors are proportional to the predicted stretching factors, the better the bootstrap resampling results. Part c) shows the seismograms arranged by increasing angle between the rupture vector and takeoff vector to each seismic station.

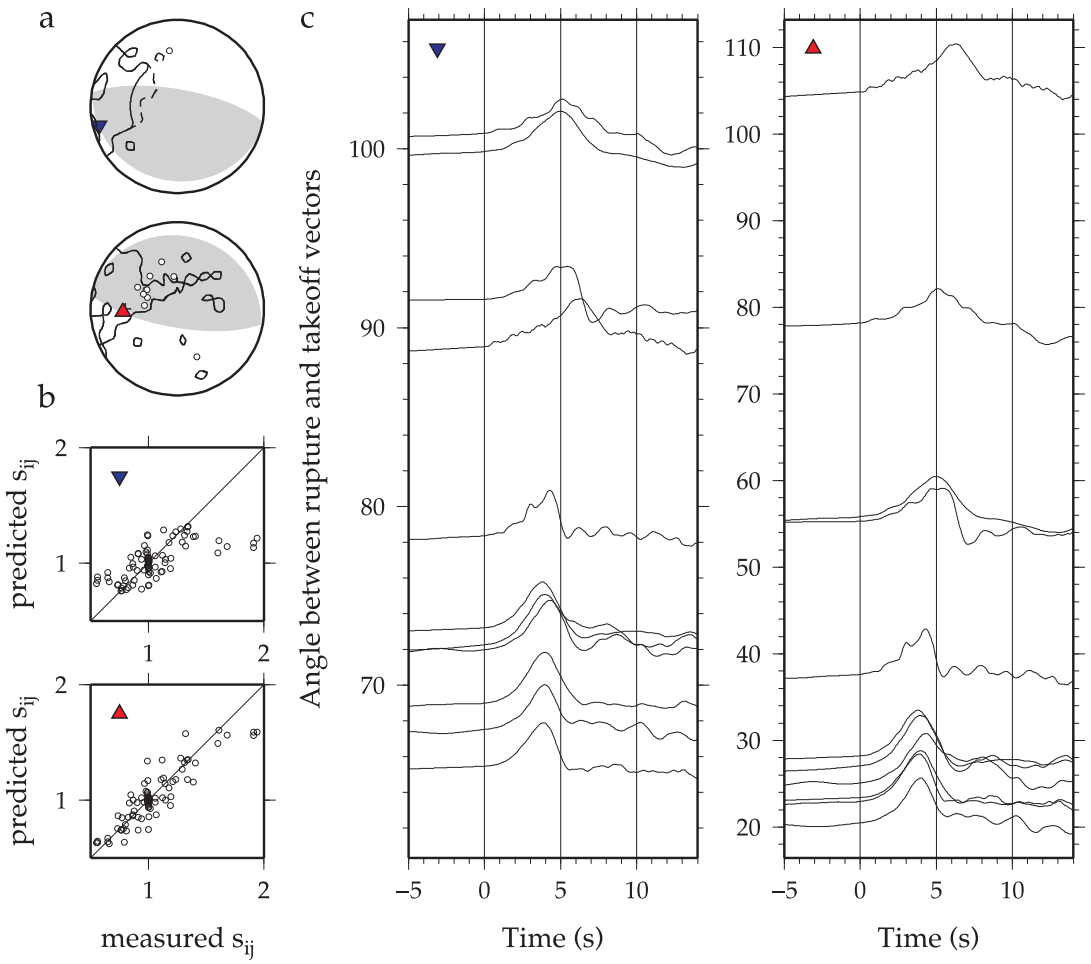

Figure B1: Results for the 13 July 1990, Mw 6.4 earthquake, which occurred at 36.42°N 70.79°E and 216 km depth. Subplots are as described at the beginning of the Appendix. For this event, our result prefer that rupture propagated to the southeast on the south-dipping near-vertical nodal plane.

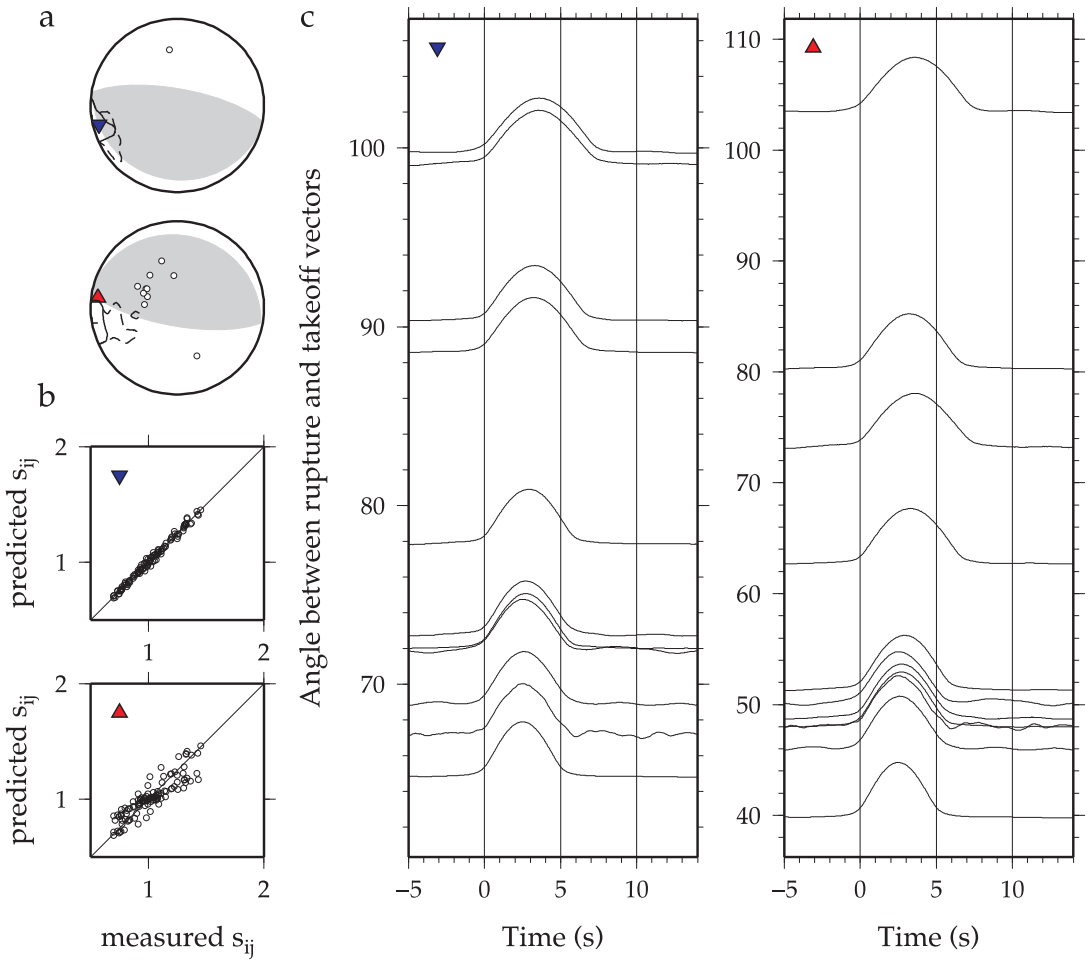

Figure B2: Synthetics for the north-dipping subhorizontal plane for the 13 July 1990, Mw 6.4 earthquake. Subplots are as described at the beginning of the Appendix. Synthetics replicate little from the rupture pattern seen for the earthquake.

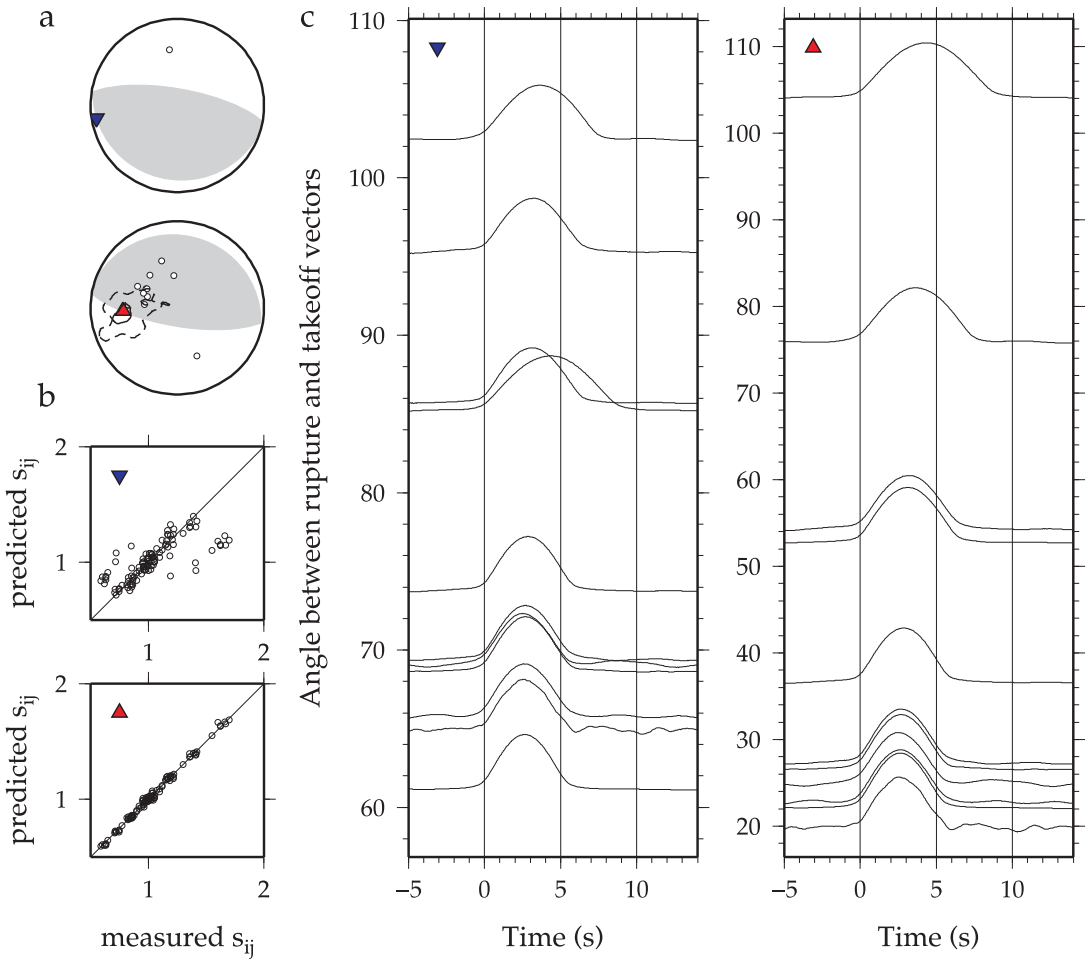

Figure B3: Synthetics for the south-dipping near-vertical plane for the 13 July 1990, Mw 6.4 earthquake. Subplots are as described at the beginning of the Appendix. Synthetics replicate little from the rupture pattern seen for the earthquake.

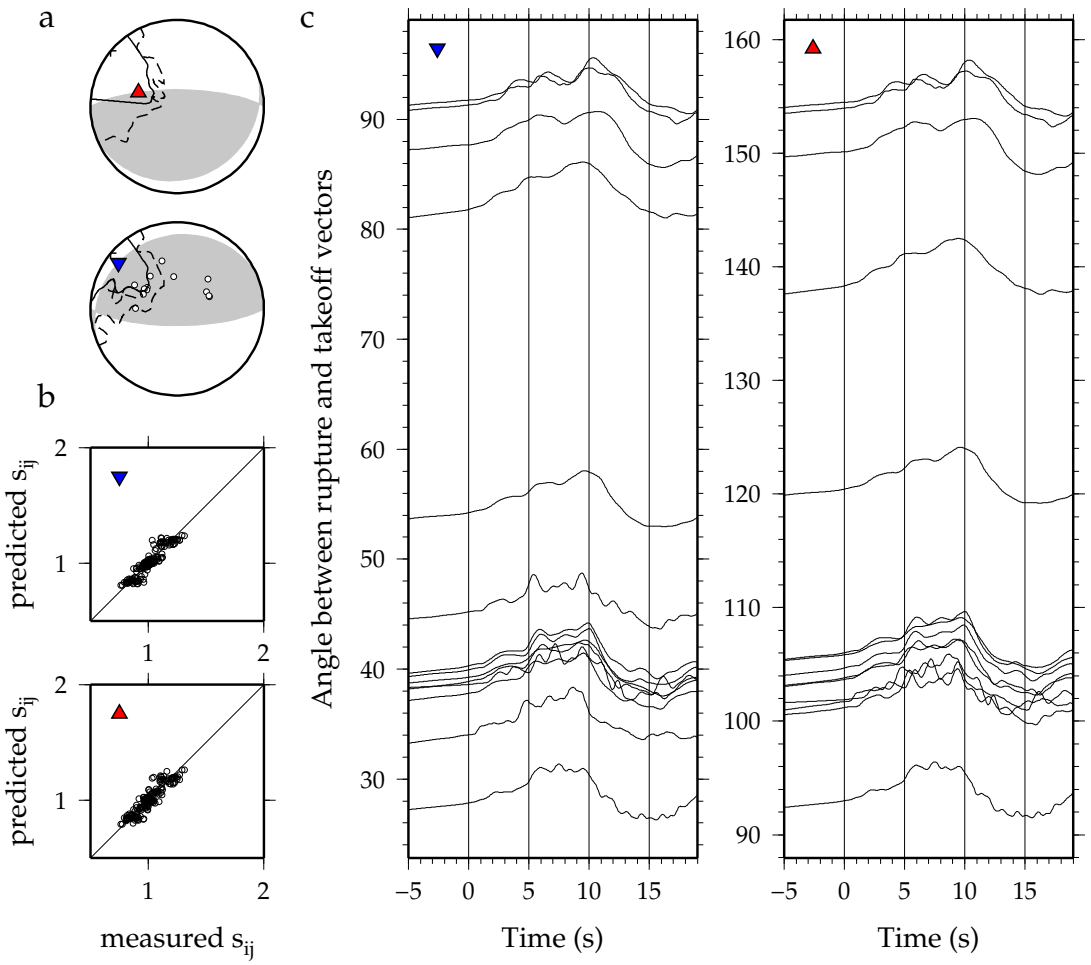

Figure B4: Results for the 31 January 1991, Mw 6.9 earthquake, which occurred at 35.99°N 70.42°E and 142 km depth. Subplots are as described at the beginning of the Appendix. For this event, our result prefer that rupture propagated to the northwest on the north-dipping subhorizontal nodal plane.

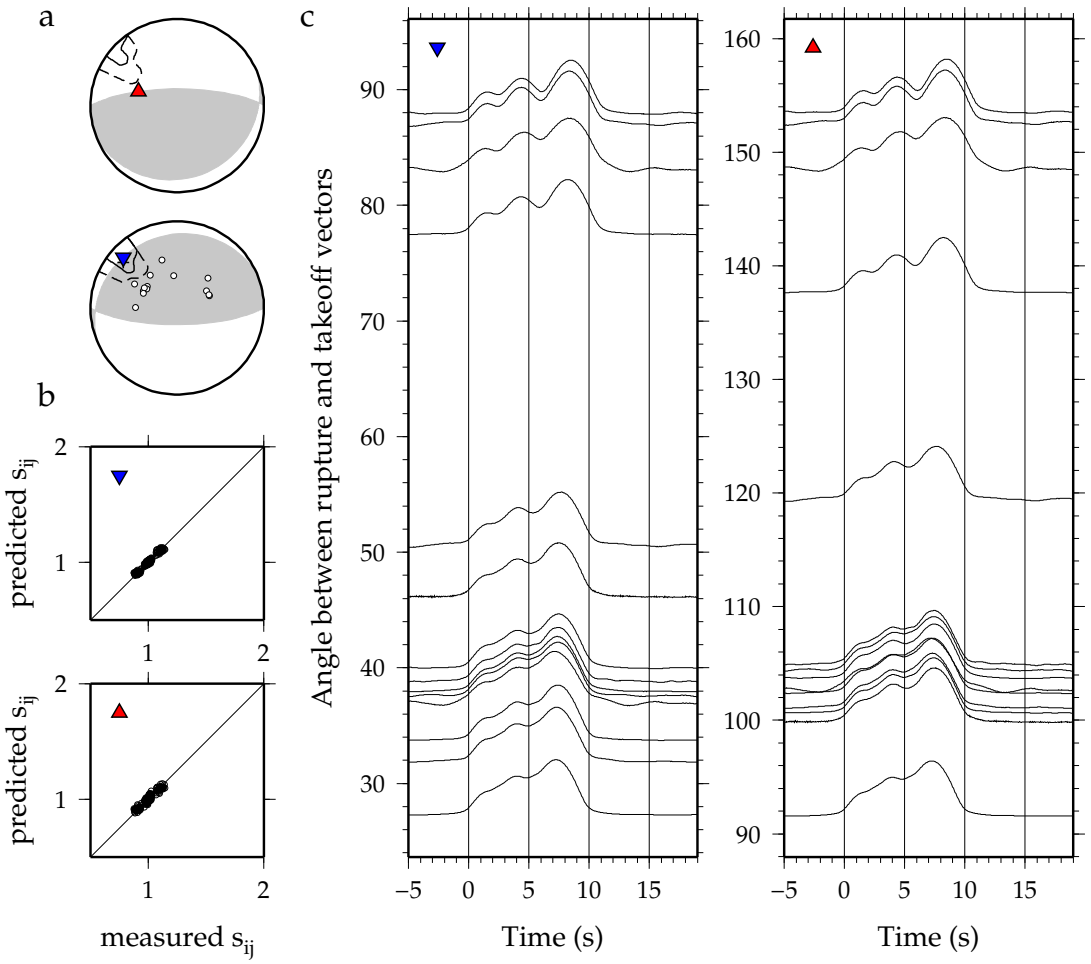

Figure B5: Synthetics for the north-dipping subhorizontal plane for the 31 January 1991, Mw 6.9 earthquake. Subplots are as described at the beginning of the Appendix. Synthetics replicate the rupture pattern seen for the earthquake.

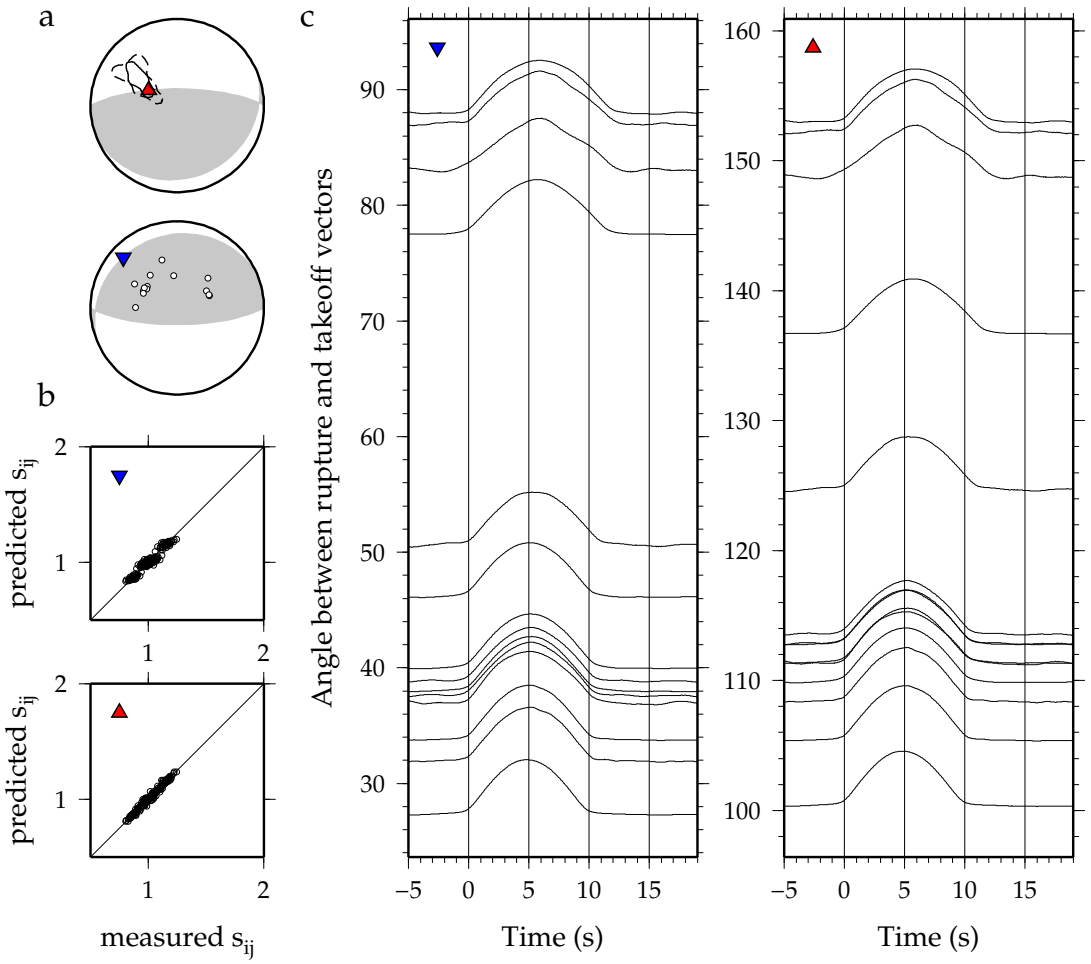

Figure B6: Synthetics for the south-dipping near-vertical plane for the 31 January 1991, Mw 6.9 earthquake. Subplots are as described at the beginning of the Appendix. Synthetics replicate the rupture pattern seen for the earthquake.

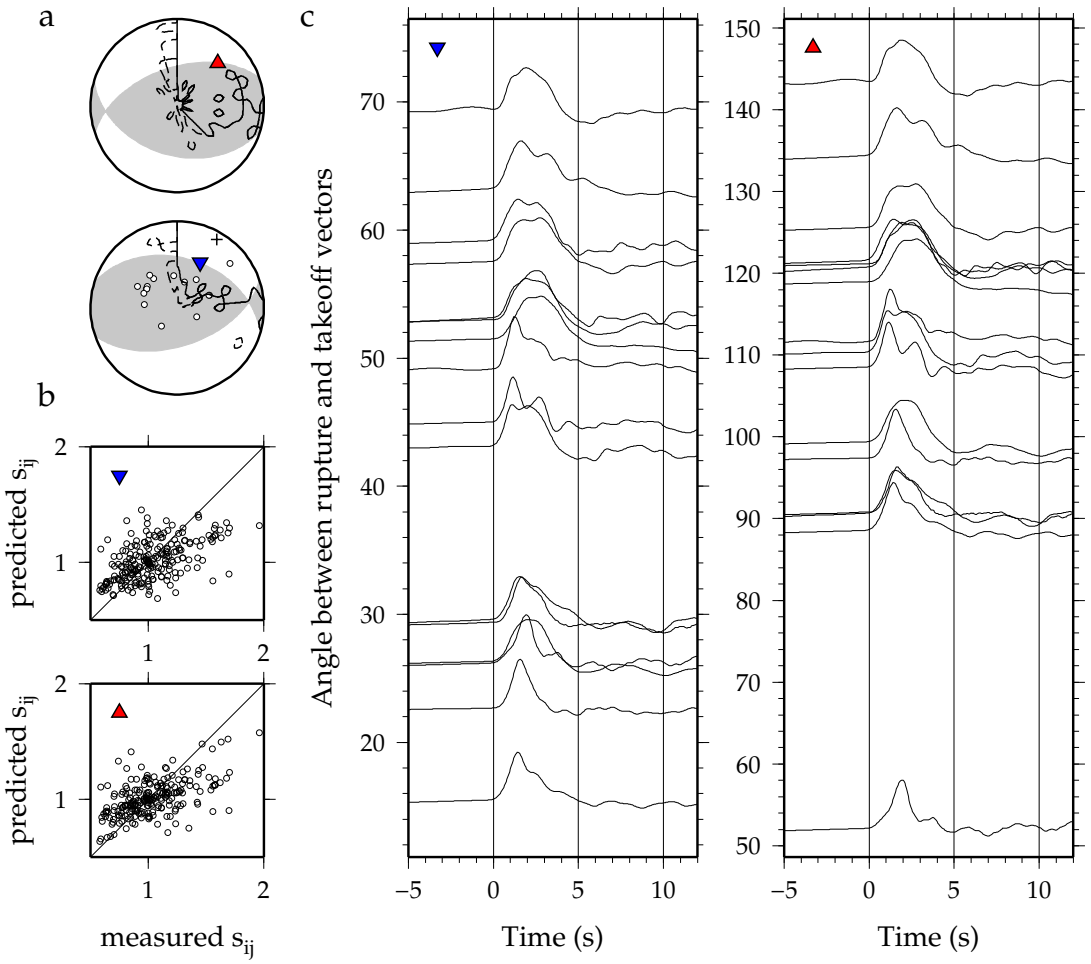

Figure B7: Results for the 14 July 1991, Mw 6.4 earthquake, which occurred at 36.33°N 71.12°E and 212 km depth. Subplots are as described at the beginning of the Appendix. For this event, we cannot tell which of the nodal planes is the fault plane.

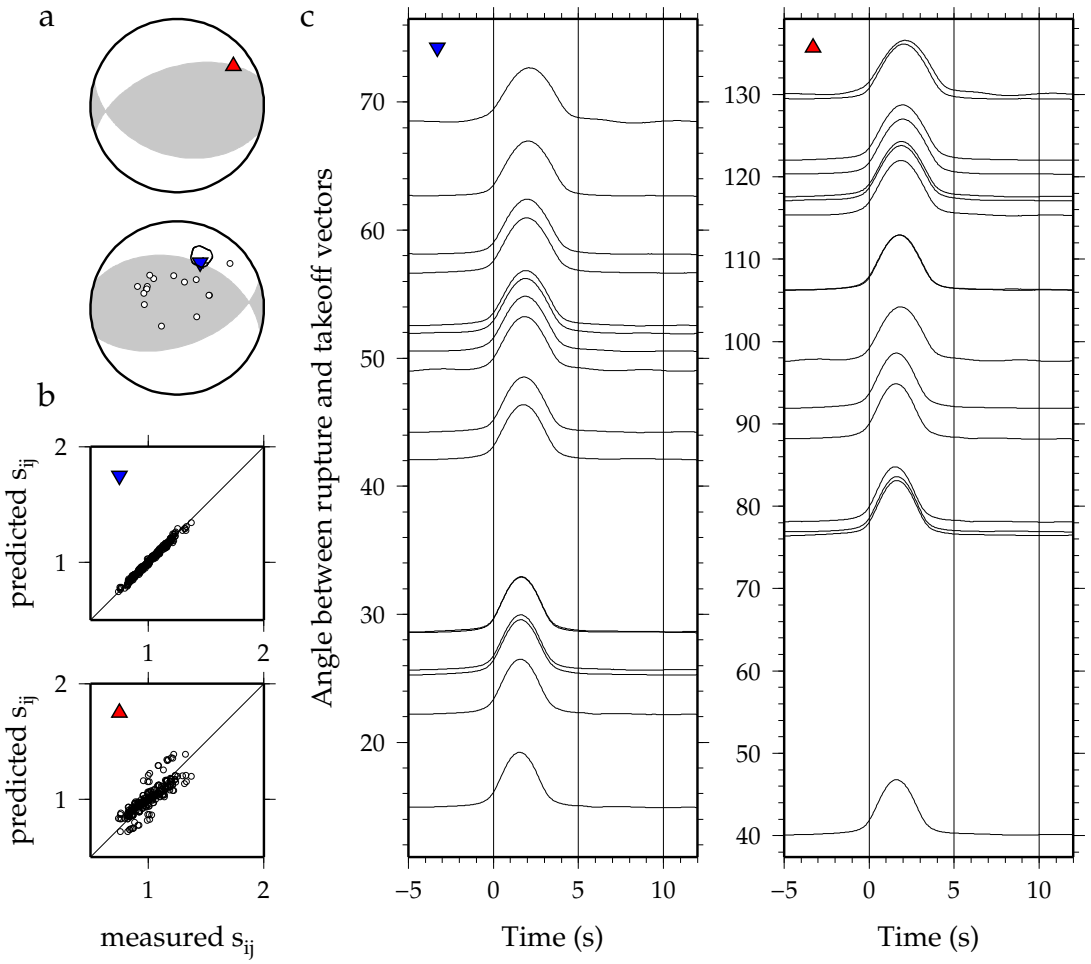

Figure B8: Synthetics for the north-dipping plane for the 14 July 1991, Mw 6.4 earthquake. Subplots are as described at the beginning of the Appendix. Synthetics replicate little from the rupture pattern seen for the earthquake.

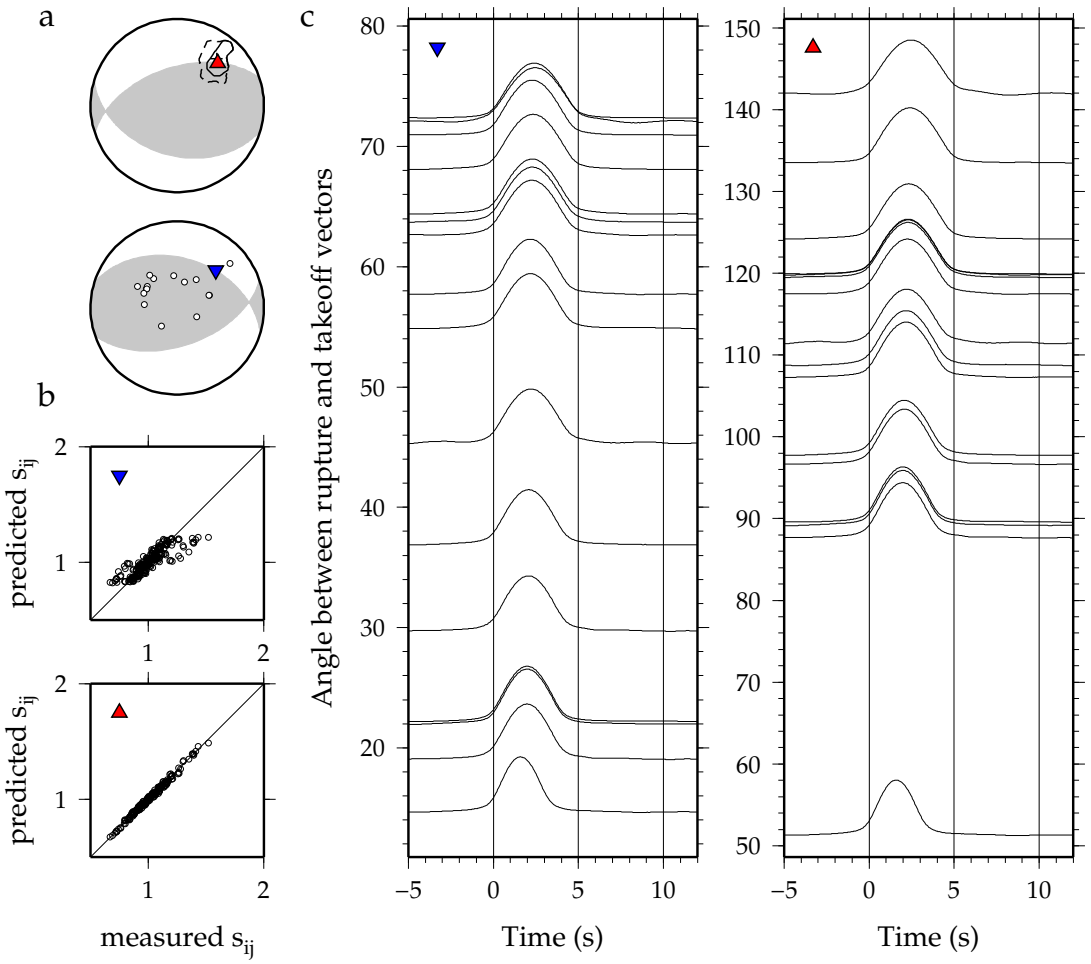

Figure B9: Synthetics for the south-dipping plane for the 14 July 1991, Mw 6.4 earthquake. Subplots are as described at the beginning of the Appendix. Synthetics replicate little from the rupture pattern seen for the earthquake.

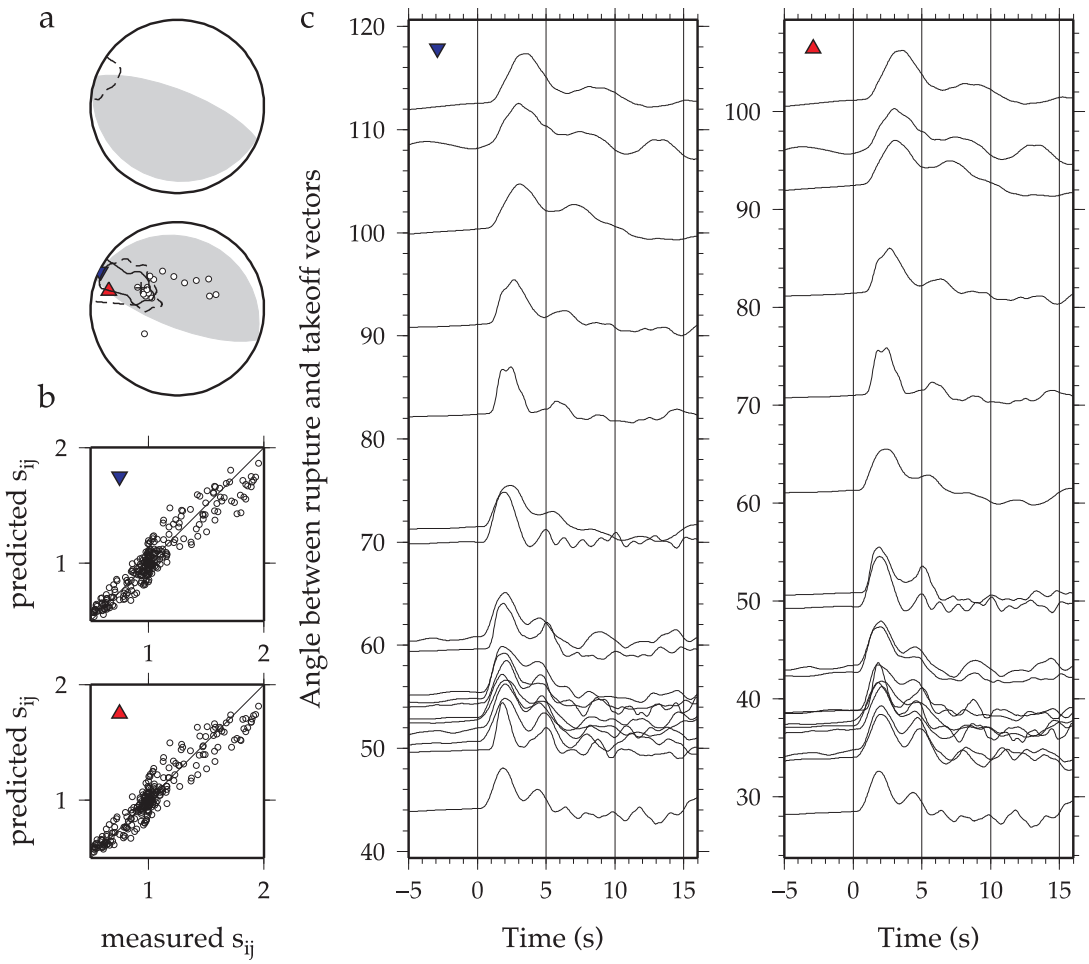

Figure B10: Results for the 9 August 1993, Mw 6.3 earthquake, which occurred at 36.44°N 70.71°E and 204 km depth. Subplots are as described at the beginning of the Appendix. For this event, we cannot tell which of the nodal planes is the fault plane, since the rupture propagated towards the intersection of the nodal planes.

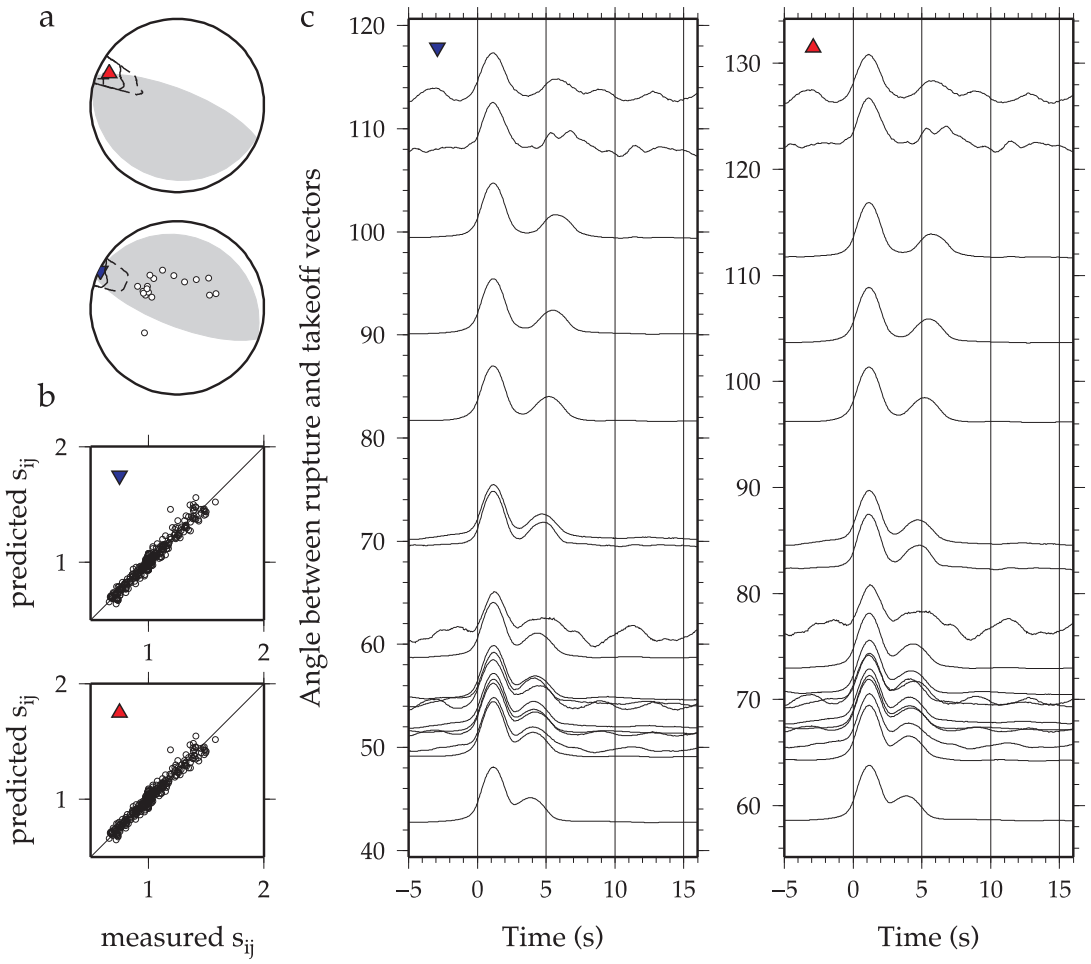

Figure B11: Synthetics for the north-northeast-dipping subhorizontal plane for the 9 August 1993, Mw 6.3 earthquake. Subplots are as described at the beginning of the Appendix. Synthetics do not replicate the rupture pattern seen for the earthquake.

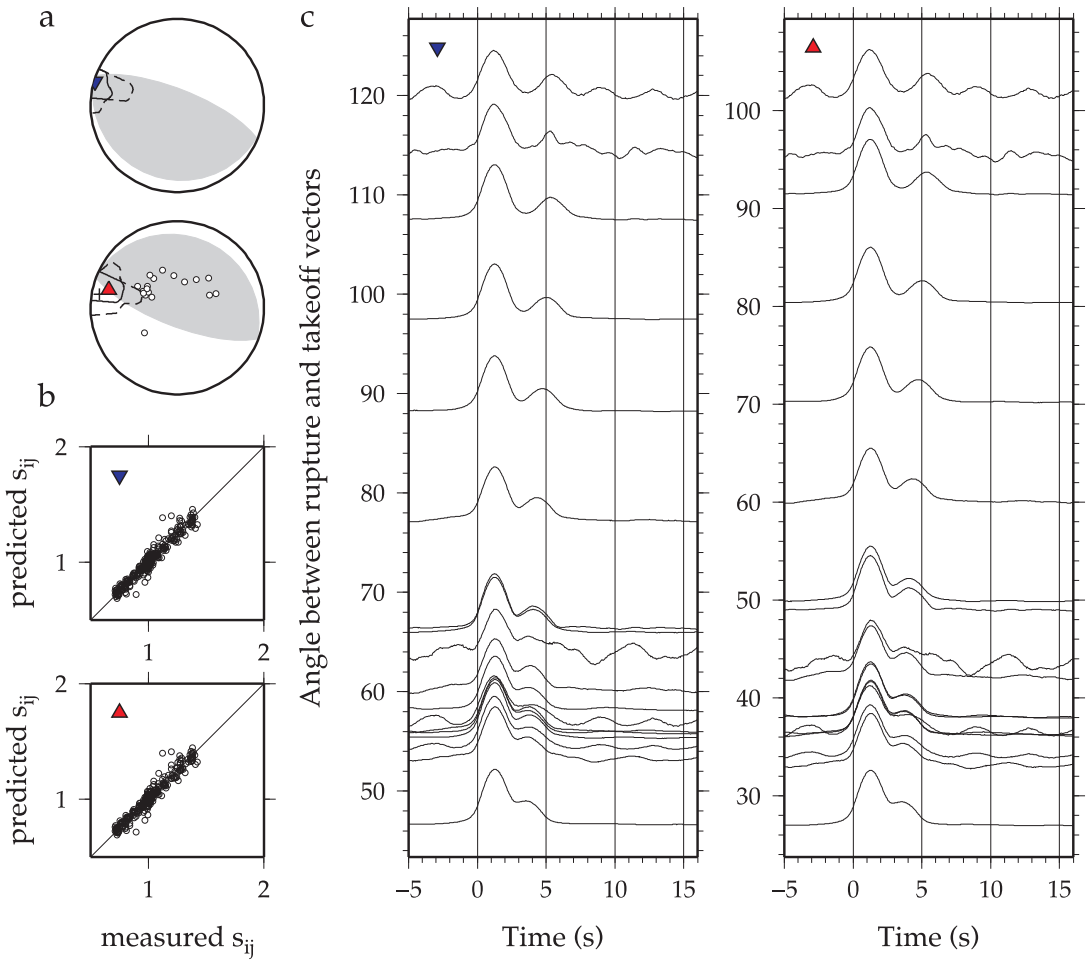

Figure B12: Synthetics for the south-southwest-dipping near-vertical plane for the 9 August 1993, Mw 6.3 earthquake. Subplots are as described at the beginning of the Appendix. Synthetics do not replicate the rupture pattern seen for the earthquake.

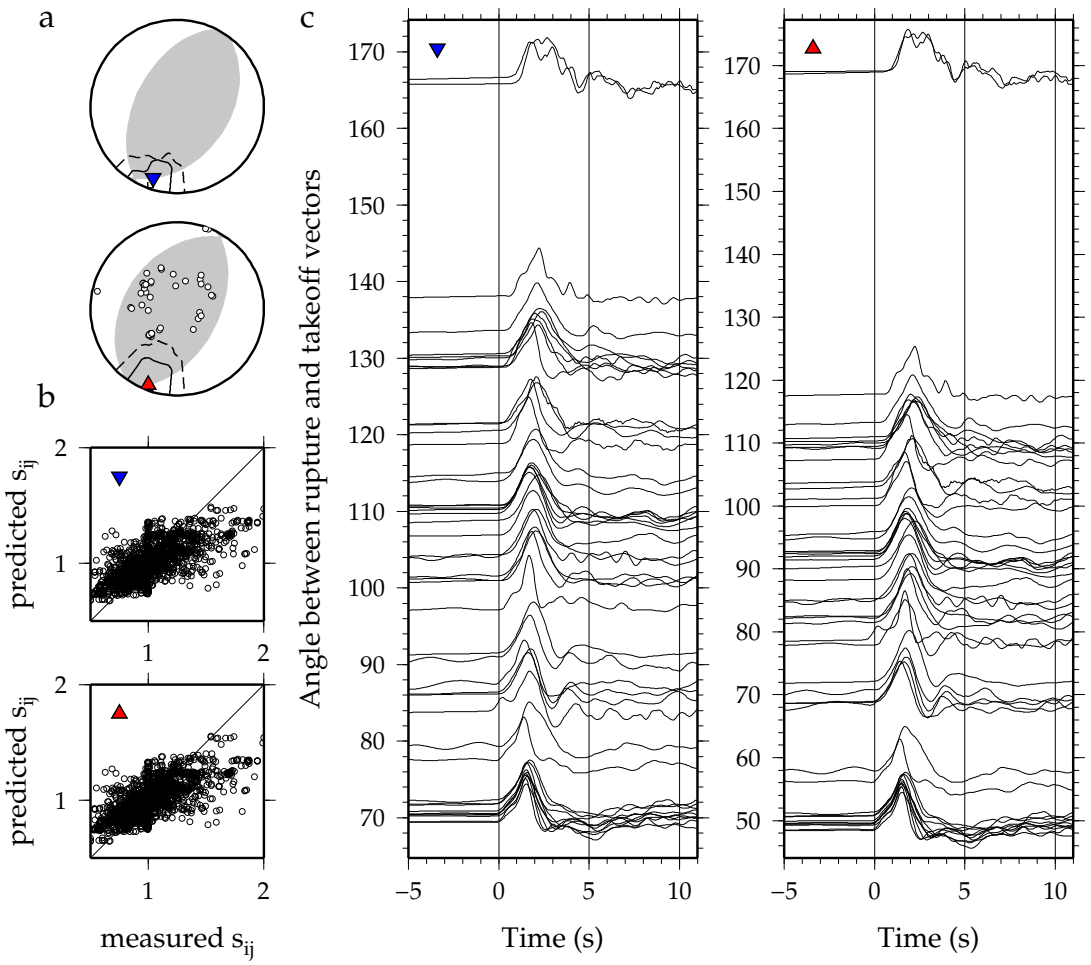

Figure B13: Results for the 30 June 1994, Mw 6.3 earthquake, which occurred at 36.33°N 71.13°E and 226 km depth. Subplots are as described at the beginning of the Appendix. For this event, we cannot tell which of the nodal planes is the fault plane, since the rupture propagated towards the intersection of the nodal planes.

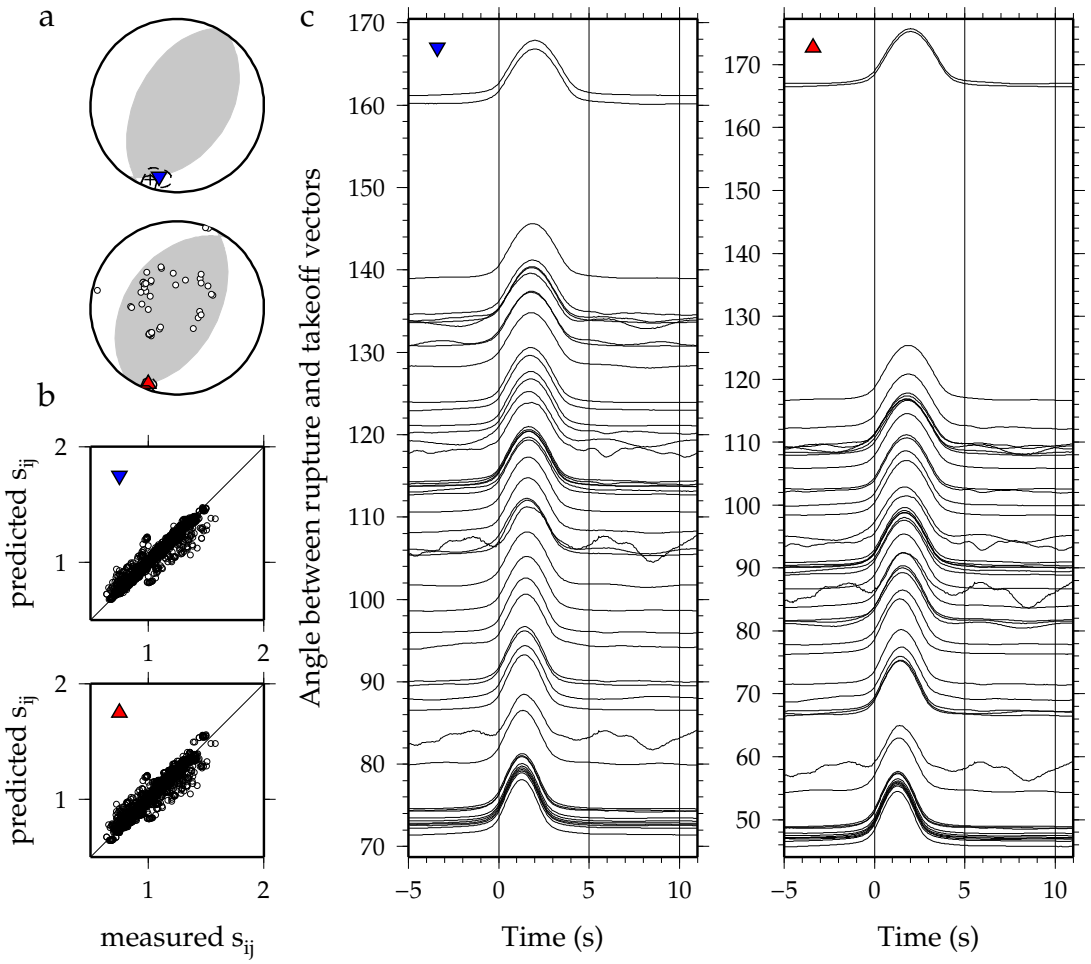

Figure B14: Synthetics for the more west-northwest-dipping plane for the 30 June 1994, Mw 6.3 earthquake. Subplots are as described at the beginning of the Appendix. Synthetics replicate the rupture pattern seen for the earthquake.

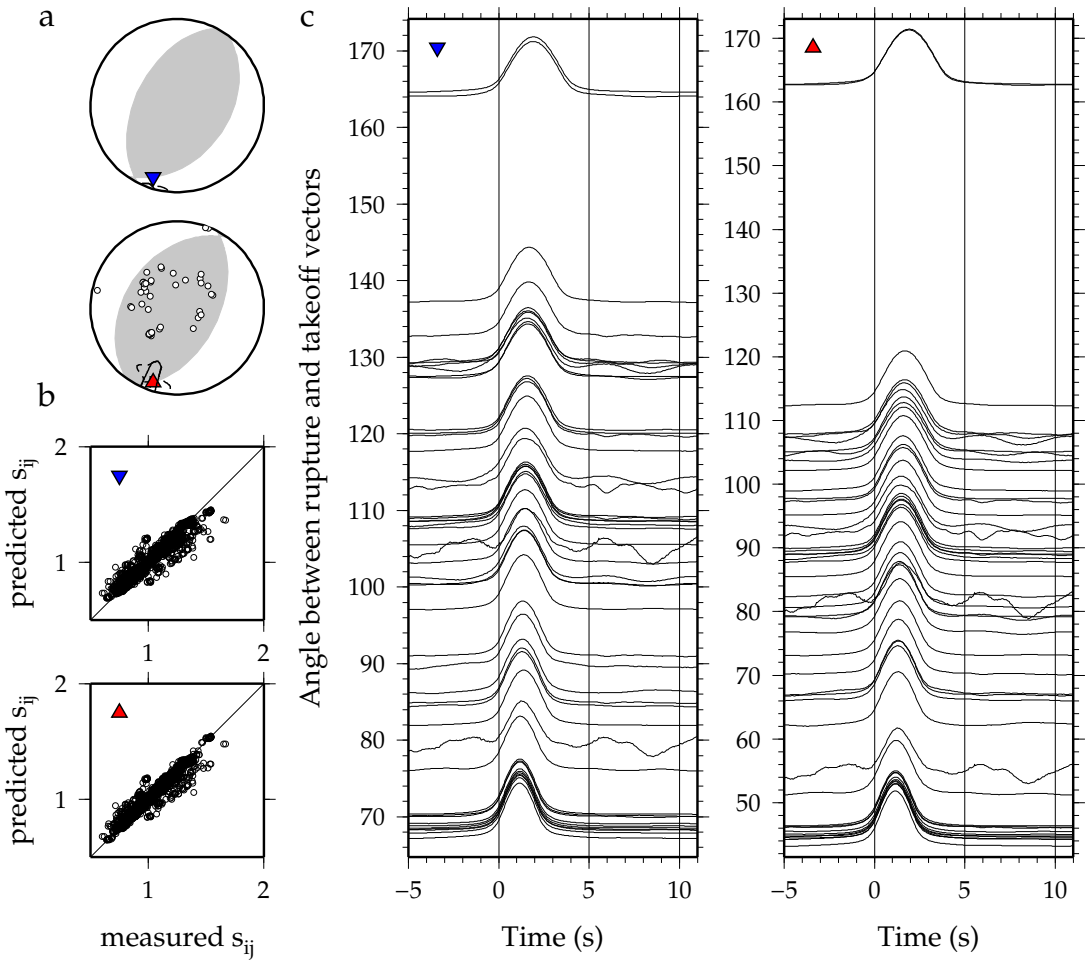

Figure B15: Synthetics for the more vertical east-southeast-dipping plane for the 30 June 1994, Mw 6.3 earthquake. Subplots are as described at the beginning of the Appendix. Synthetics replicate the rupture pattern seen for the earthquake.

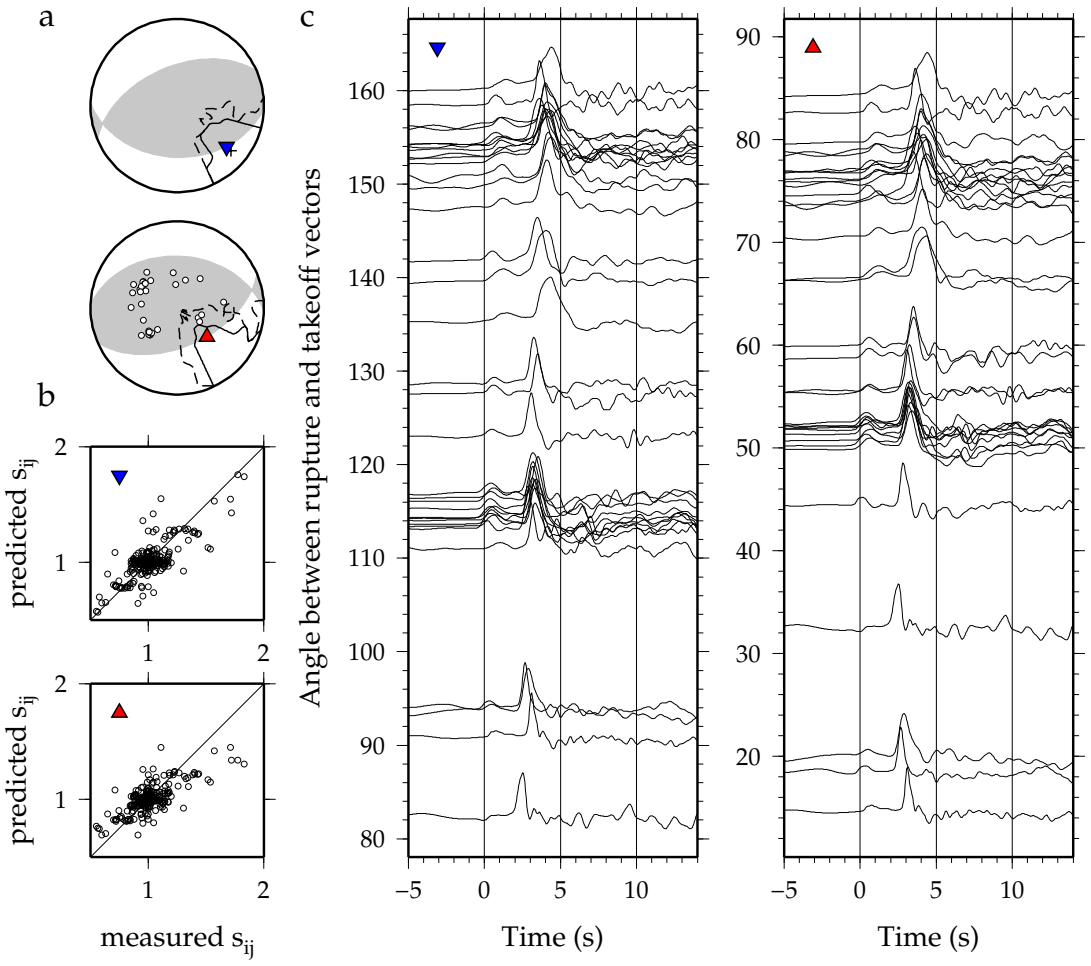

Figure B16: Results for the 25 October 1994, Mw 6.0 earthquake, which occurred at 36.36°N 70.96°E and 238 km depth. Subplots are as described at the beginning of the Appendix. For this event, we cannot tell which of the nodal planes is the fault plane.

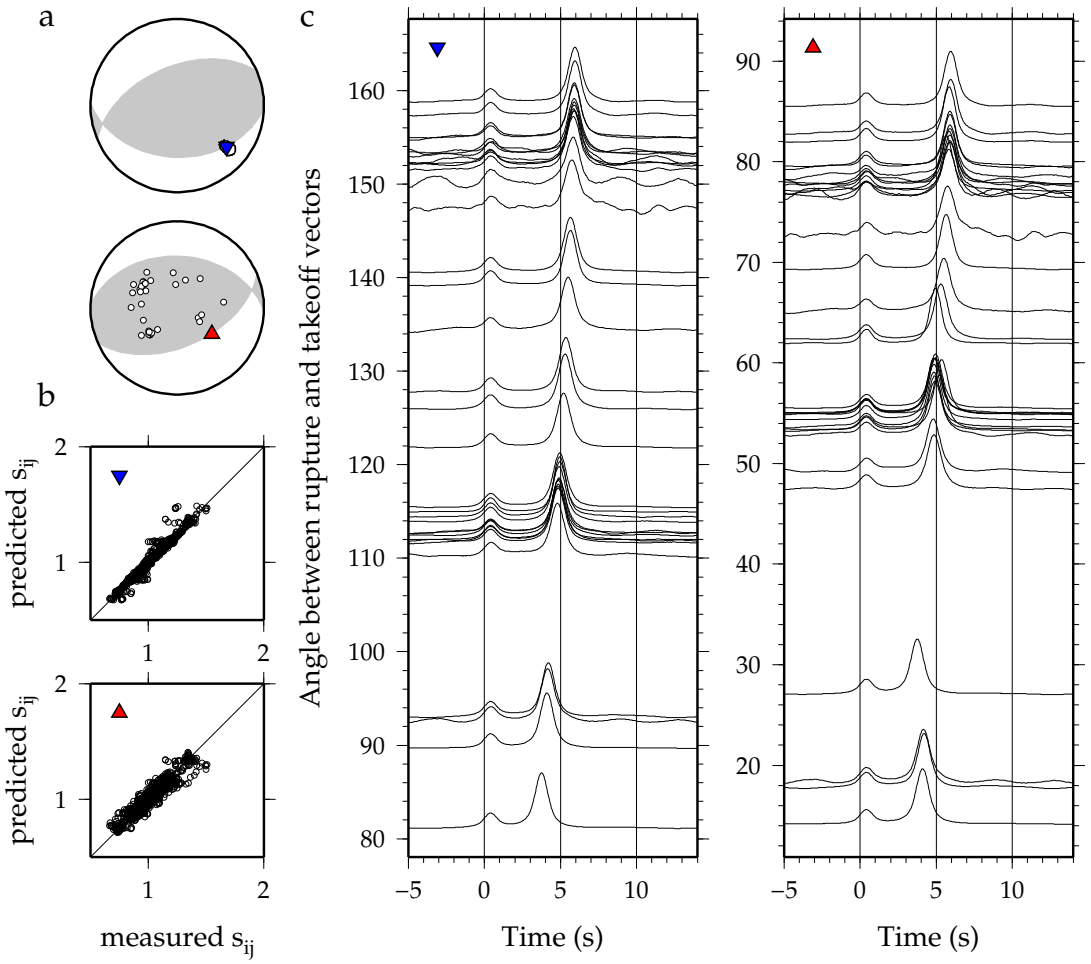

Figure B17: Synthetics for the north-dipping plane for the 25 October 1994, Mw 6.0 earthquake. Subplots are as described at the beginning of the Appendix. Synthetics replicate the rupture pattern seen for the earthquake.

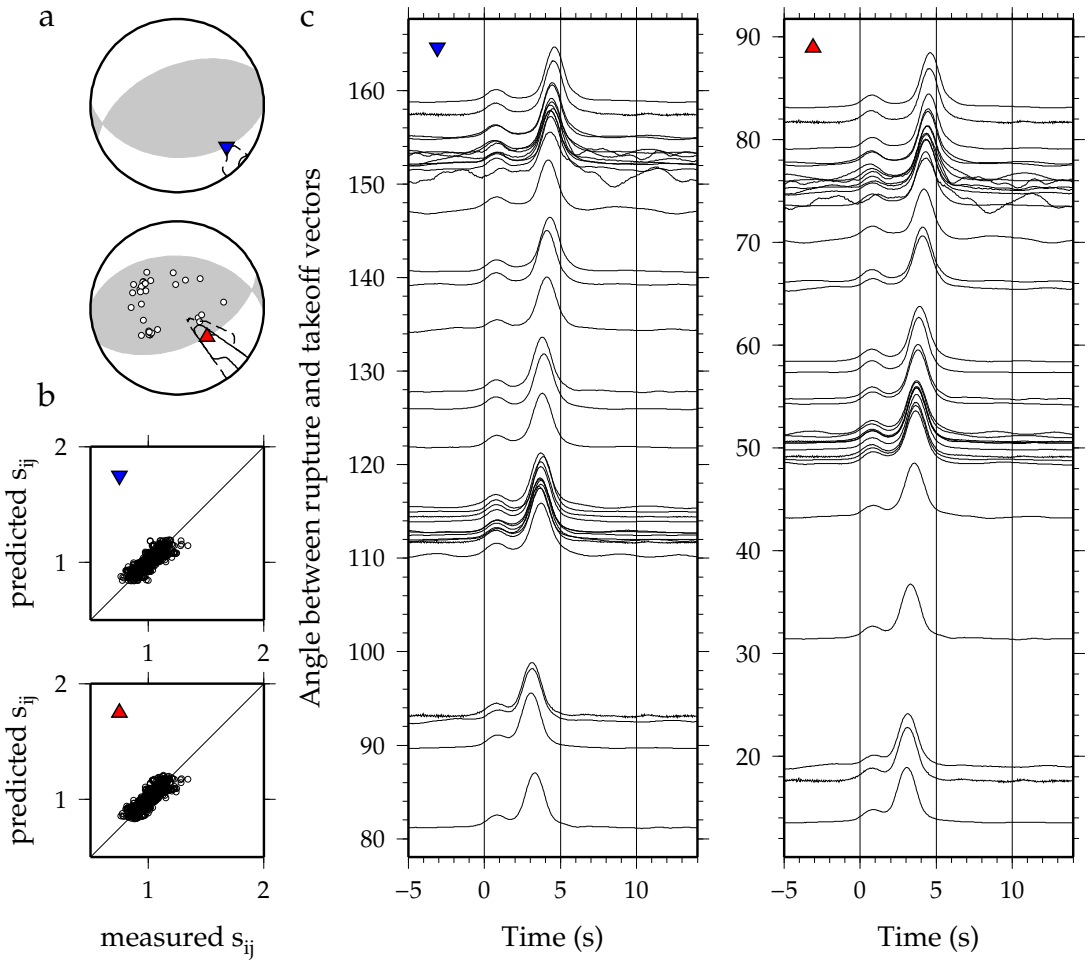

Figure B18: Synthetics for the south-southeast-dipping plane for the 25 October 1994, Mw 6.0 earthquake. Subplots are as described at the beginning of the Appendix. Synthetics replicate the rupture pattern seen for the earthquake.

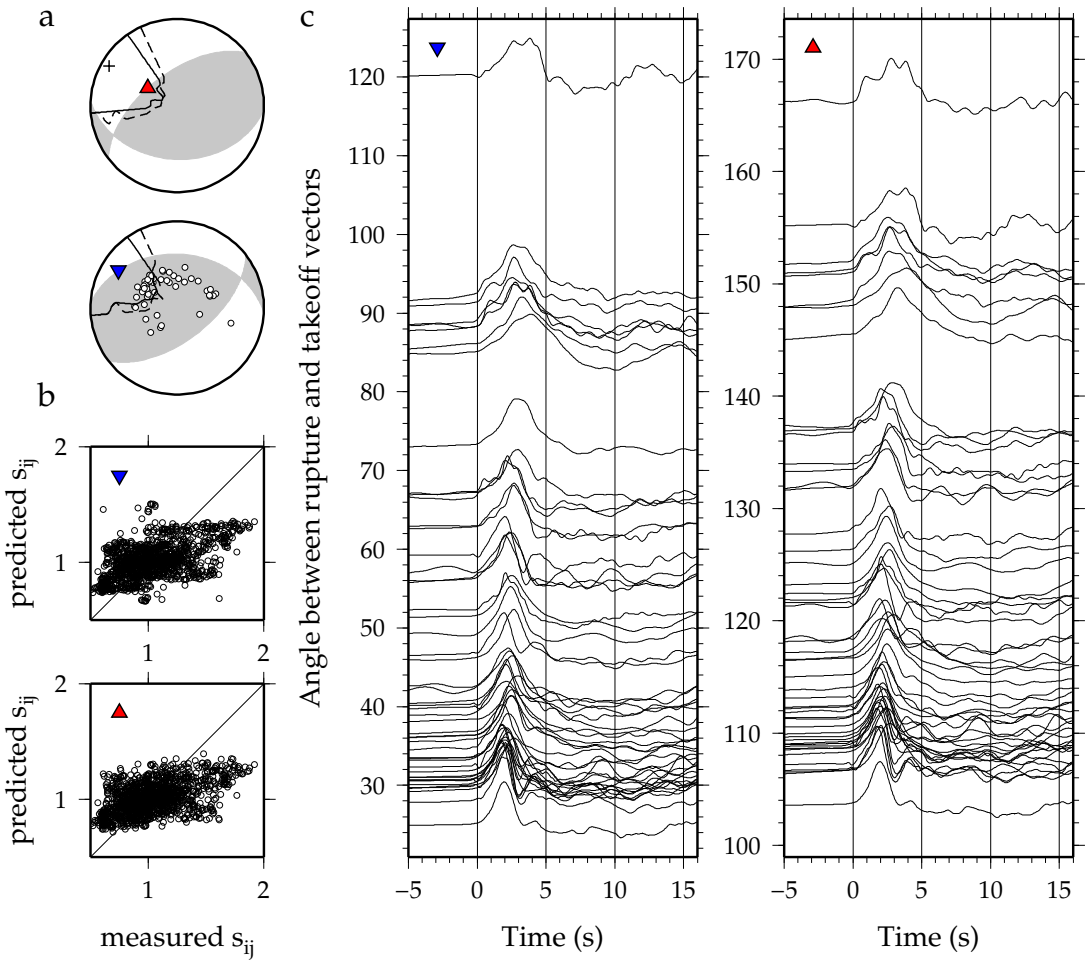

Figure B19: Results for the 13 May 1997, Mw 6.5 earthquake, which occurred at 36.41°N 70.94°E and 196 km depth. Subplots are as described at the beginning of the Appendix. For this event, our results indicate that rupture propagated to the northwest on the north-dipping nodal plane.

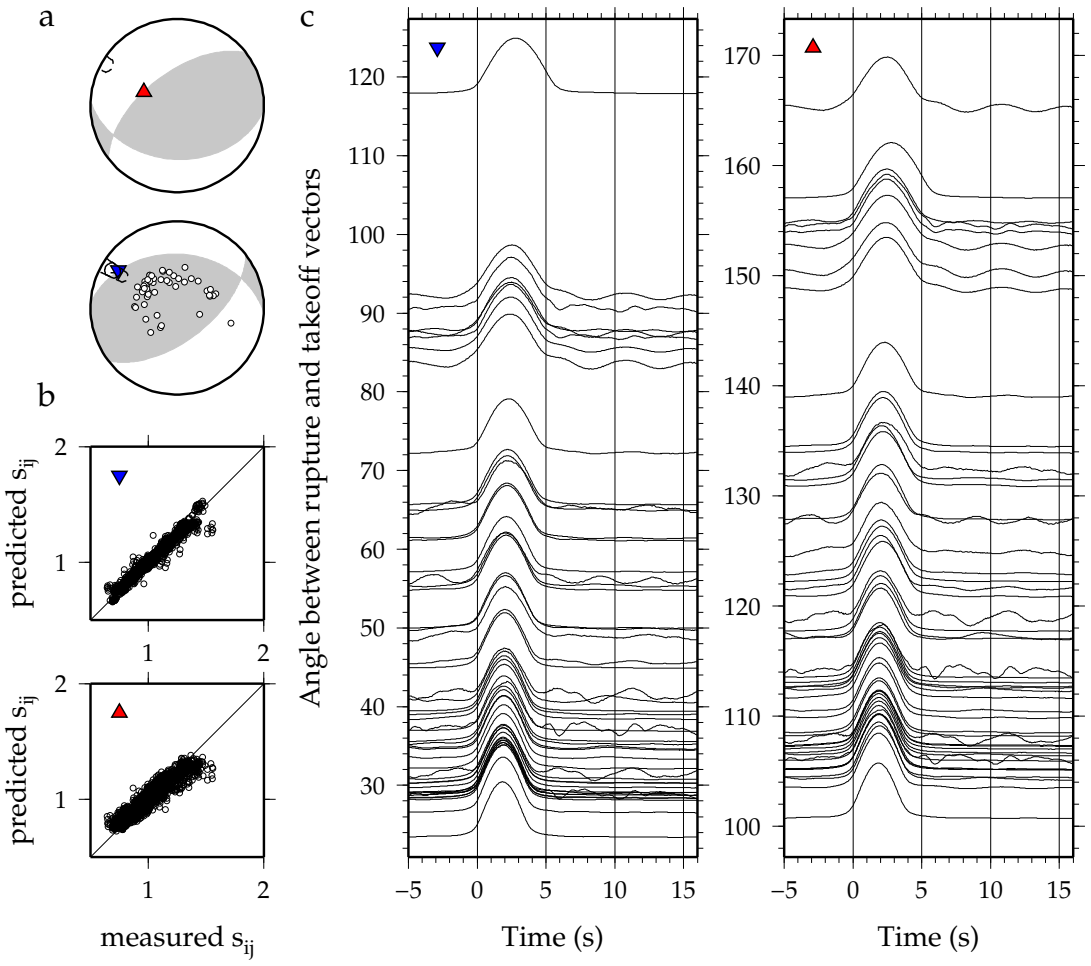

Figure B20: Synthetics for the north-dipping plane for the 13 May 1997, Mw 6.5 earthquake. Subplots are as described at the beginning of the Appendix. Synthetics replicate the rupture pattern seen for the earthquake.

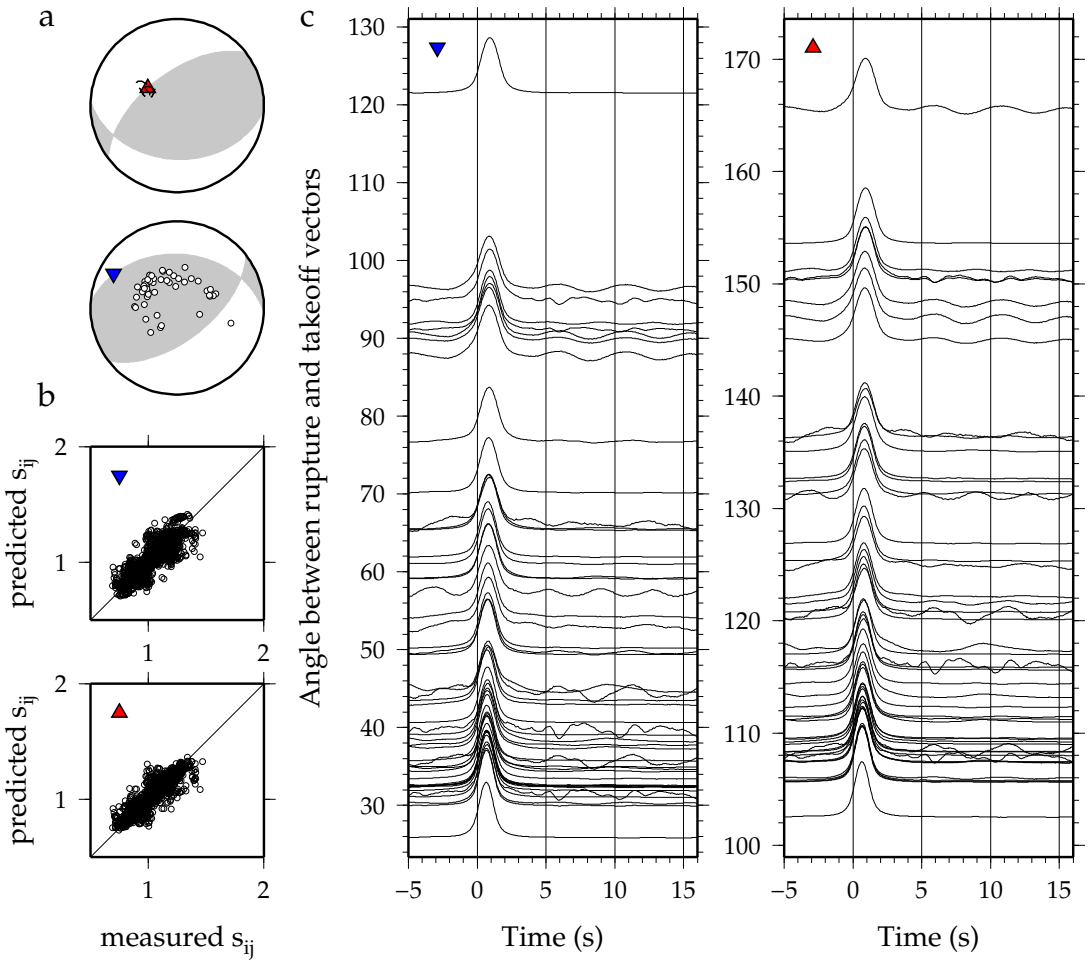

Figure B21: Synthetics for the southeast-dipping plane for the 13 May 1997, Mw 6.5 earthquake. Subplots are as described at the beginning of the Appendix. Synthetics replicate the rupture pattern seen for the earthquake.

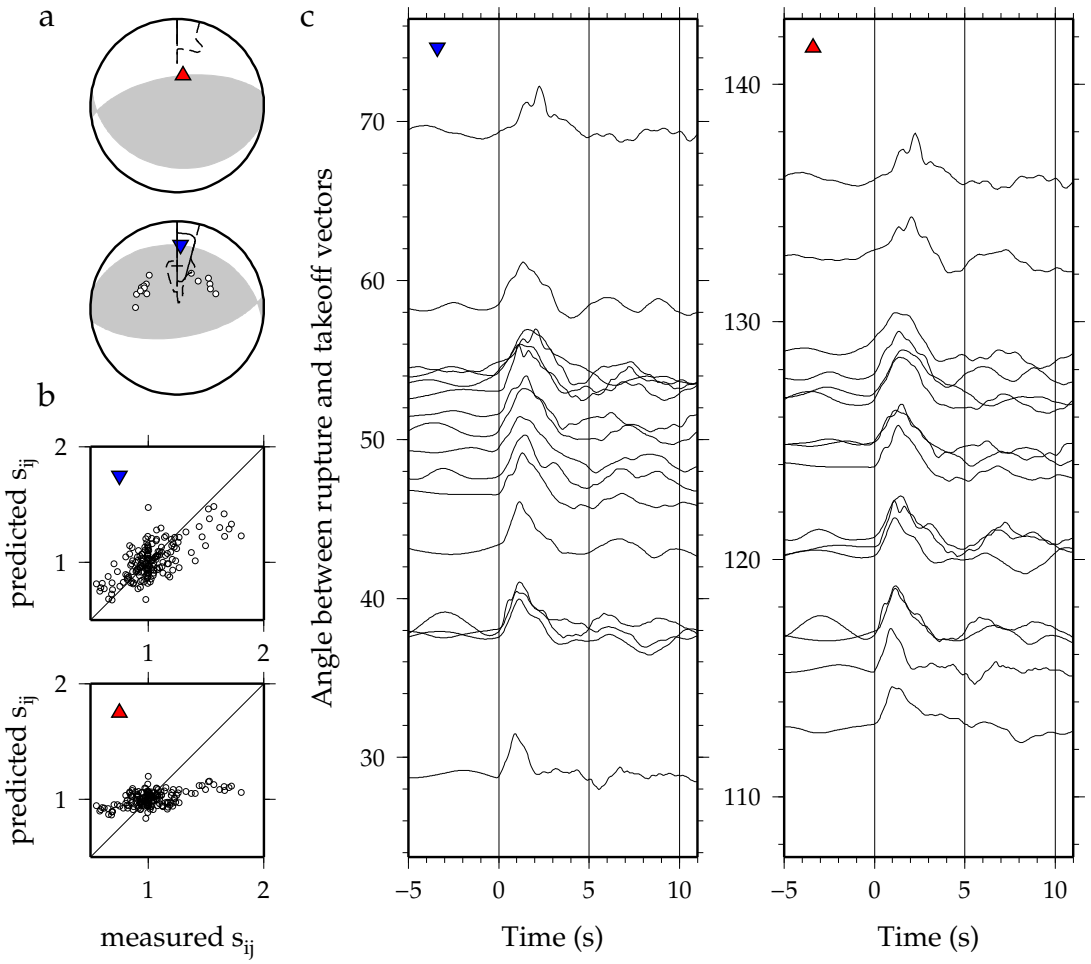

Figure B22: Results for the 14 February 1998, Mw 5.5 earthquake, which occurred at 36.36°N 71.11°E and 218 km depth. Subplots are as described at the beginning of the Appendix. For this event, we cannot tell which of the nodal planes is the fault plane.

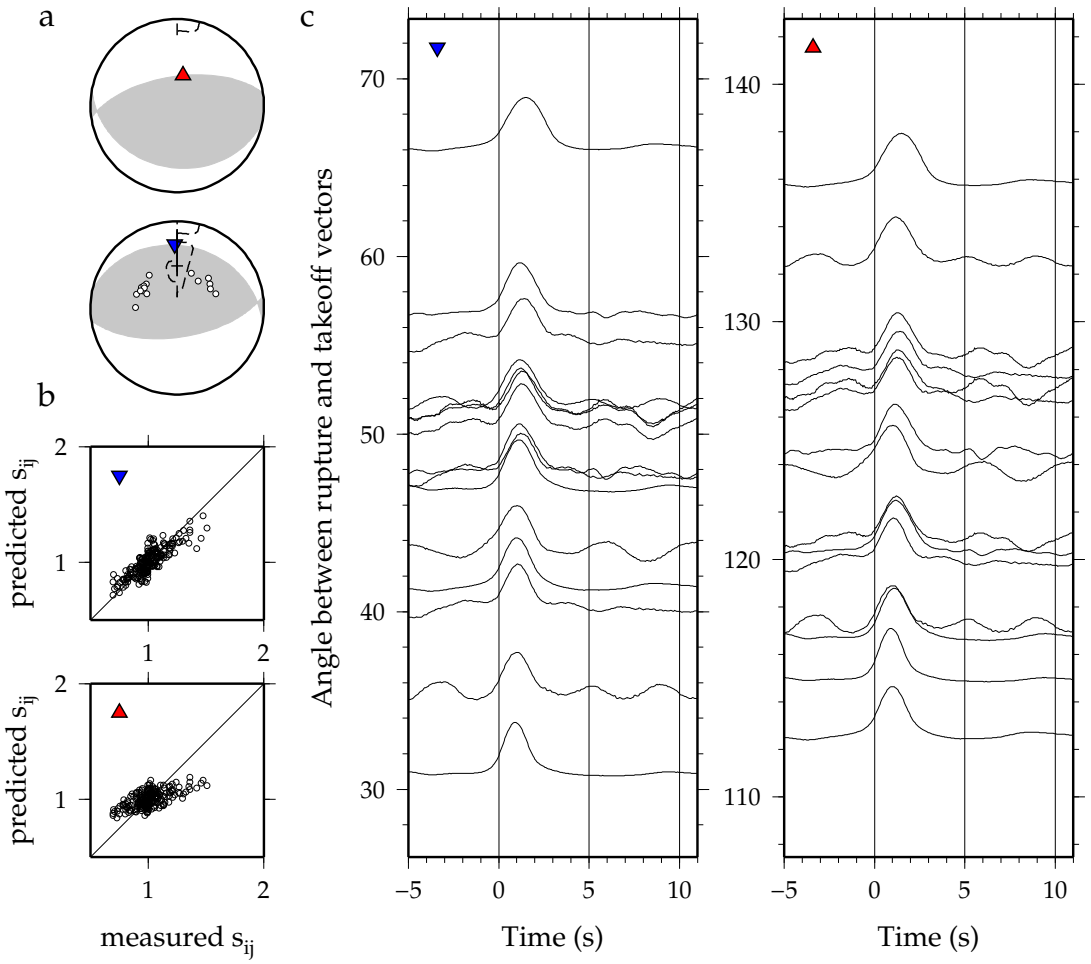

Figure B23: Synthetics for the north-dipping subhorizontal plane for the 14 February 1998, Mw 5.5 earthquake. Subplots are as described at the beginning of the Appendix. Synthetics replicate the rupture pattern seen for the earthquake.

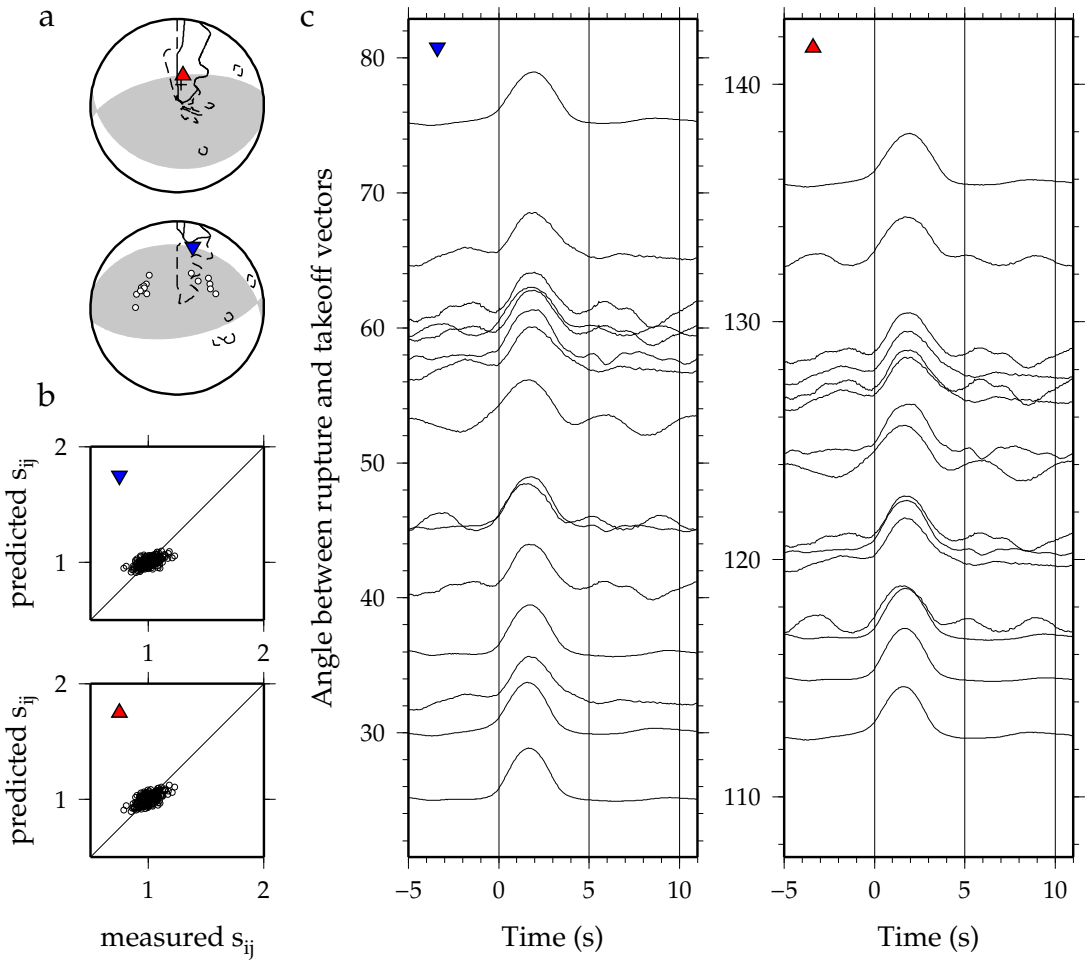

Figure B24: Synthetics for the south-dipping near-vertical plane for the 14 February 1998, Mw 5.5 earthquake. Subplots are as described at the beginning of the Appendix. Synthetics replicate the rupture pattern seen for the earthquake.

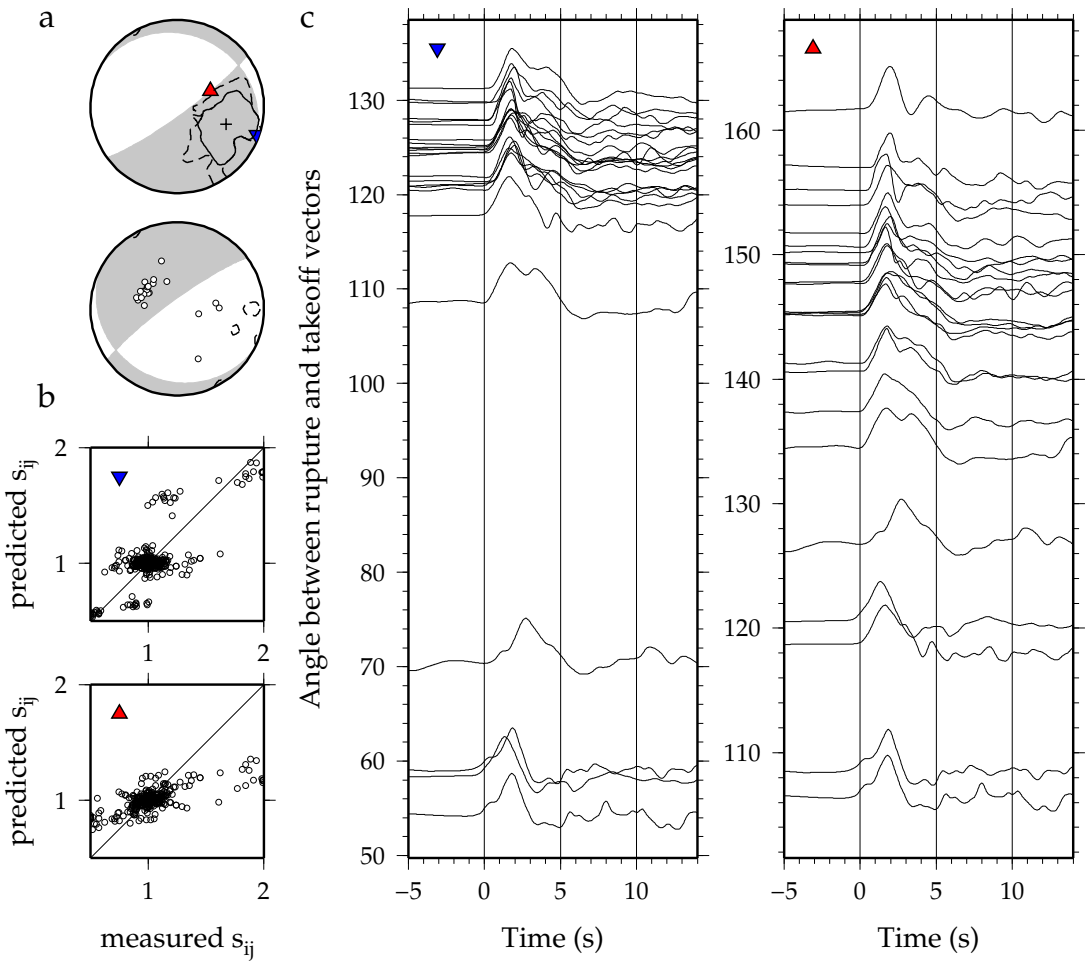

Figure B25: Results for the 12 May 2000, Mw 6.3 earthquake, which occurred at 35.97°N 70.66°E and 107 km depth. Subplots are as described at the beginning of the Appendix. For this event, we cannot tell which of the nodal planes is the fault plane, since the rupture propagated towards the intersection of the nodal planes.

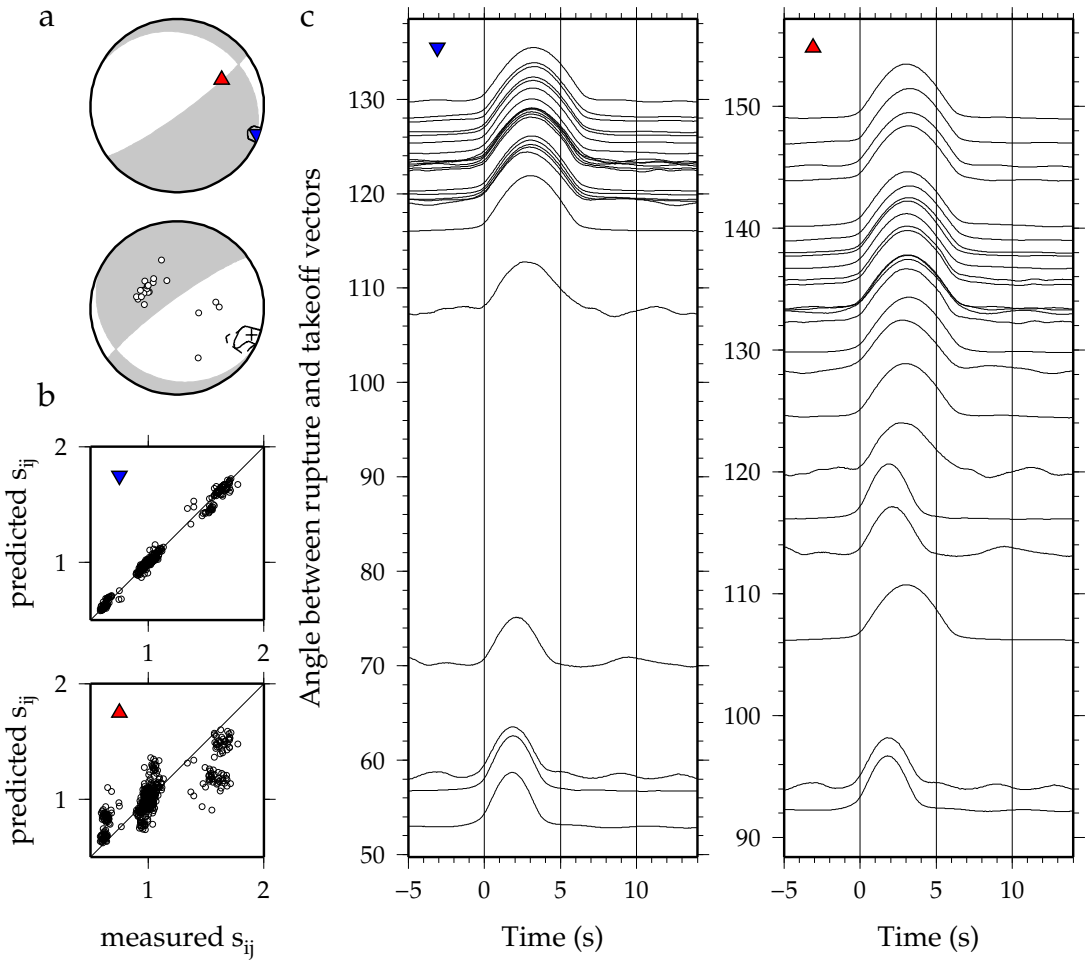

Figure B26: Synthetics for the southwest-dipping subhorizontal plane for the 12 May 2000, Mw 6.3 earthquake. Subplots are as described at the beginning of the Appendix. Synthetics replicate the rupture pattern seen for the earthquake.

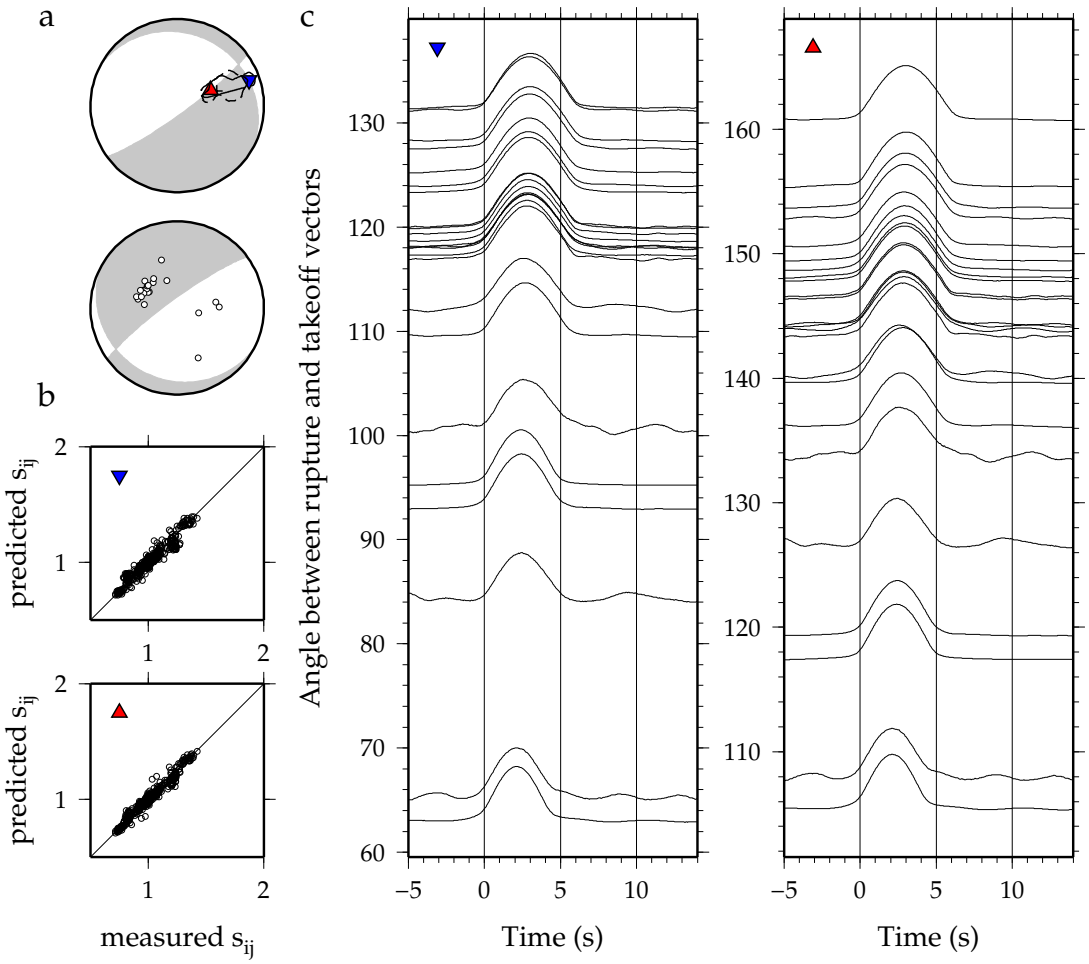

Figure B27: Synthetics for the northwest-dipping near-vertical plane for the 12 May 2000, Mw 6.3 earthquake. Subplots are as described at the beginning of the Appendix. Synthetics do not replicate the rupture pattern seen for the earthquake.

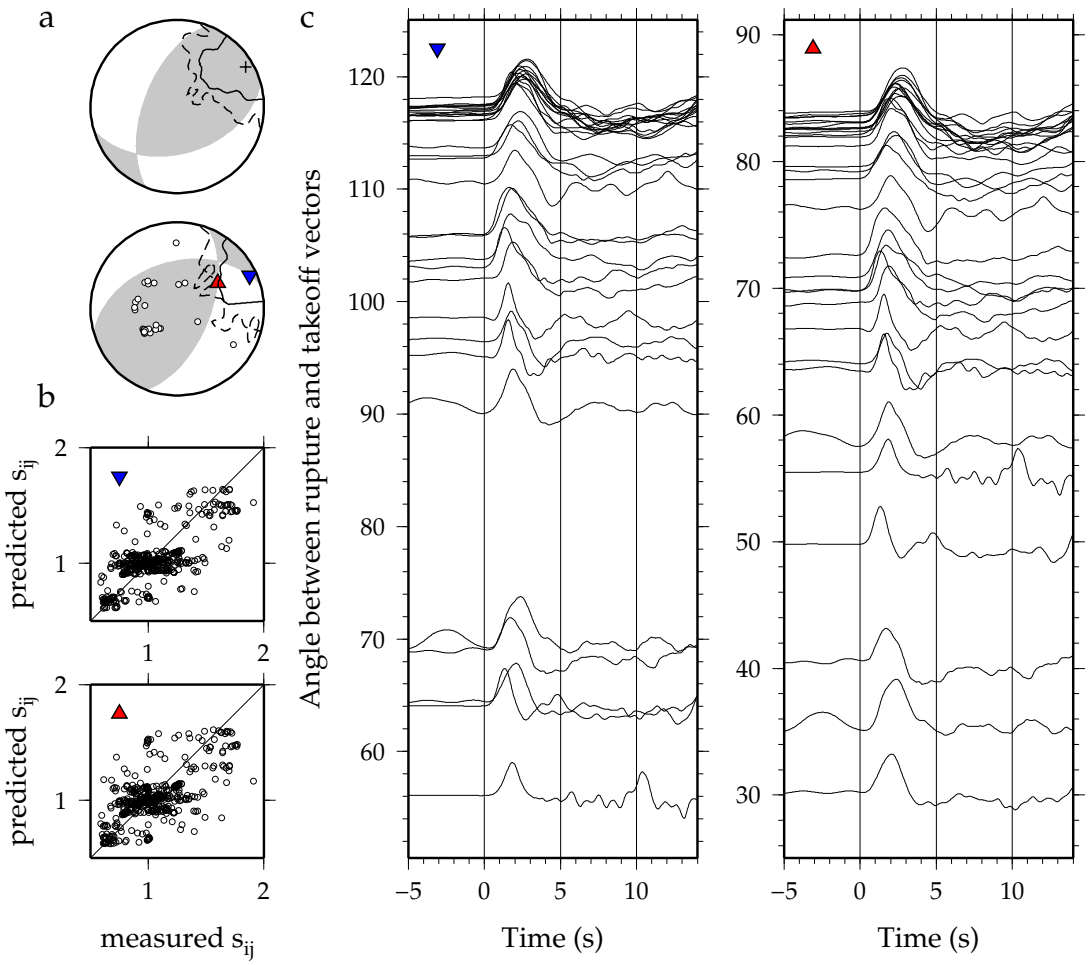

Figure B28: Results for the 23 November 2001, Mw 6.1 earthquake, which occurred at 36.39°N 71.51°E and 106 km depth. Subplots are as described at the beginning of the Appendix. For this event, we cannot tell which of the nodal planes is the fault plane, since the rupture propogated to the intersection of the nodal planes.

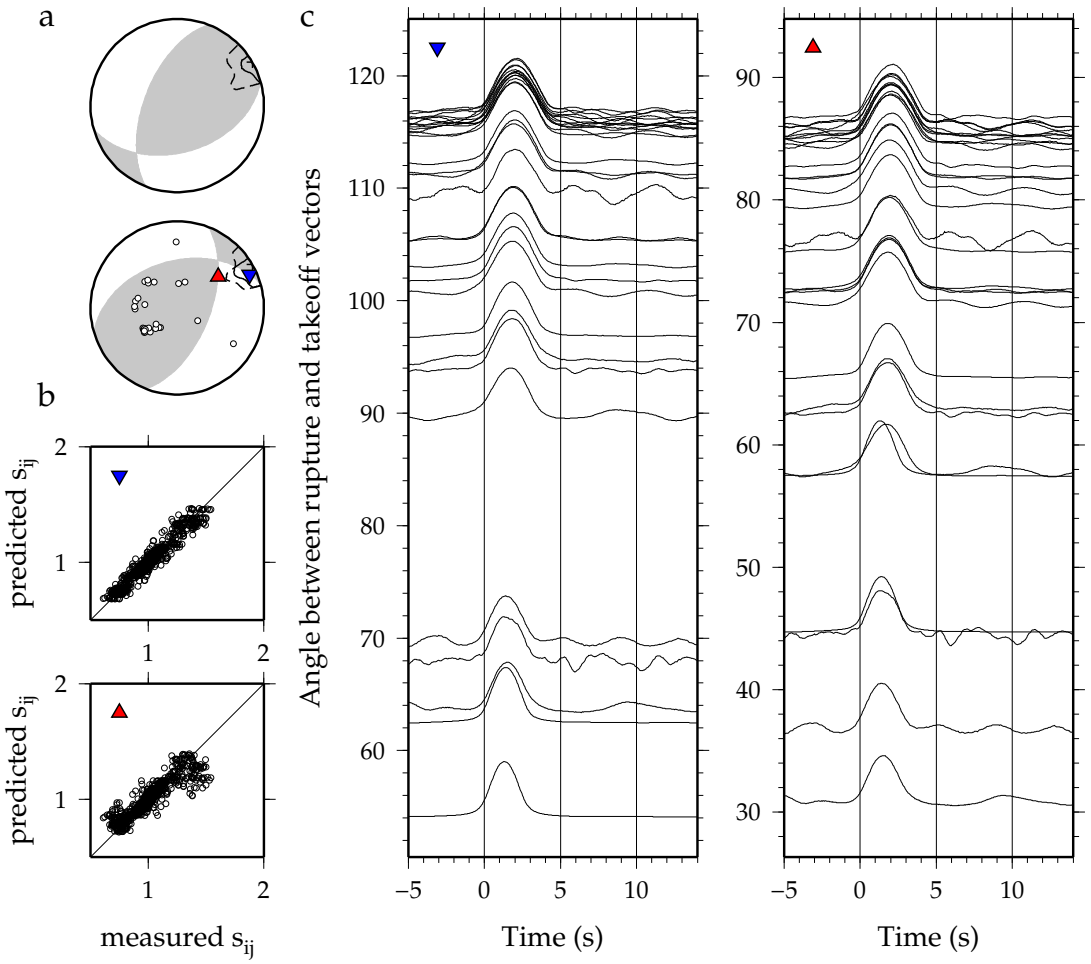

Figure B29: Synthetics for the north-northwest-dipping plane for the 23 November 2001, Mw 6.1 earthquake. Subplots are as described at the beginning of the Appendix. Synthetics replicate the rupture pattern seen for the earthquake.

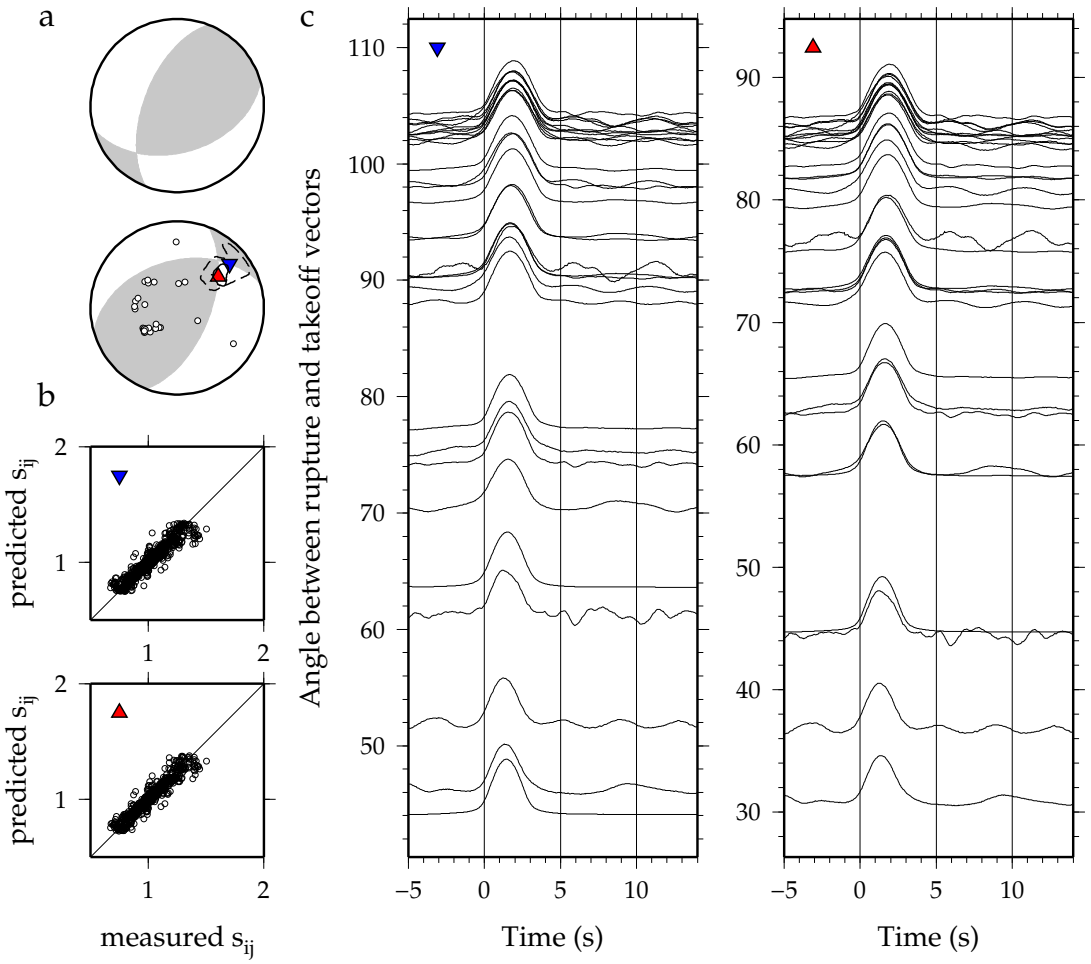

Figure B30: Synthetics for the south-southeast-dipping plane for the 23 November 2001, Mw 6.1 earthquake. Subplots are as described at the beginning of the Appendix. Synthetics replicate little from the rupture pattern seen for the earthquake.

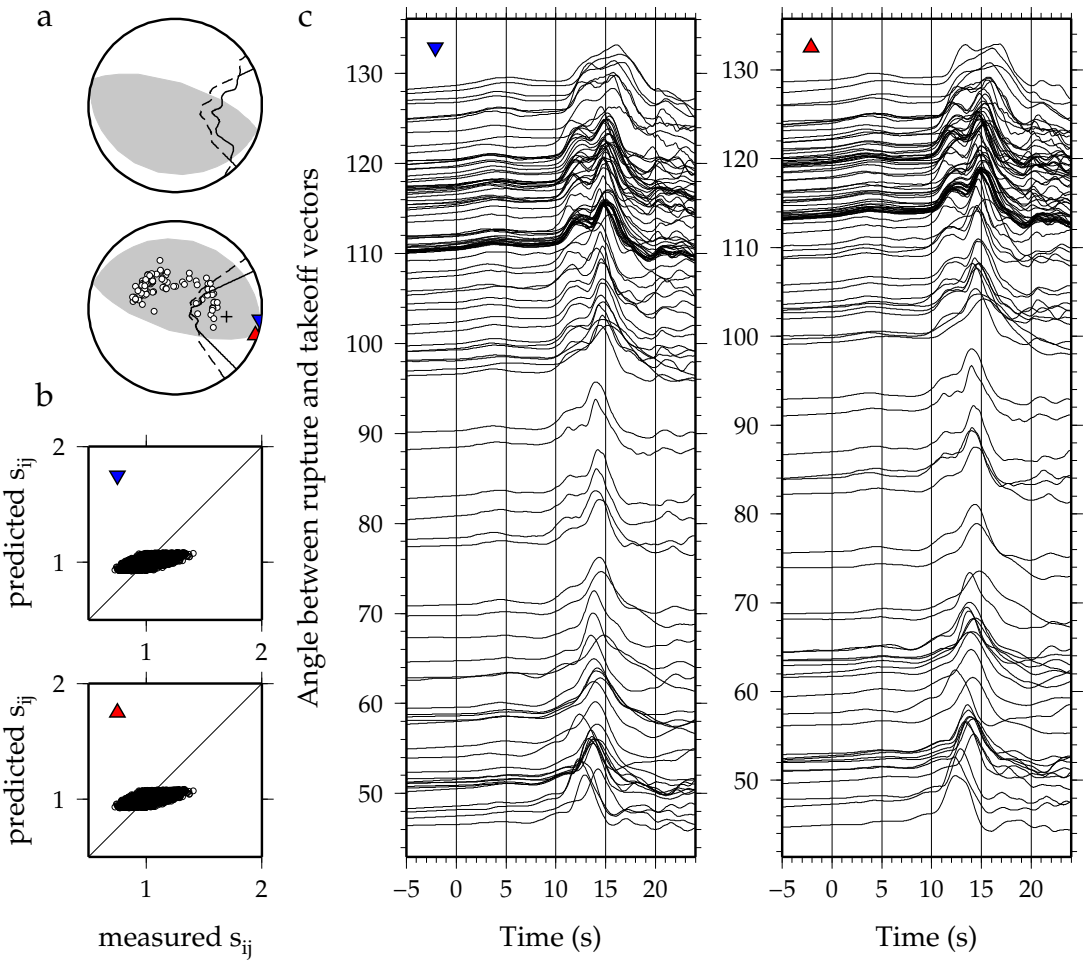

Figure B31: Results for the 3 March 2002, Mw 6.3 and Mw 7.4 earthquakes, which occured at 36.43°N 70.44°E 209 km depth and 36.50°N 70.48°E 225 km depth, separately. The Mw 6.3 earthquake occurred 12 seconds earlier than the Mw 7.4 earthquake. Subplots are as described at the beginning of the Appendix. For this event, we cannot tell which of the nodal planes is the fault plane, since the rupture propagated towards the intersection of the nodal planes.

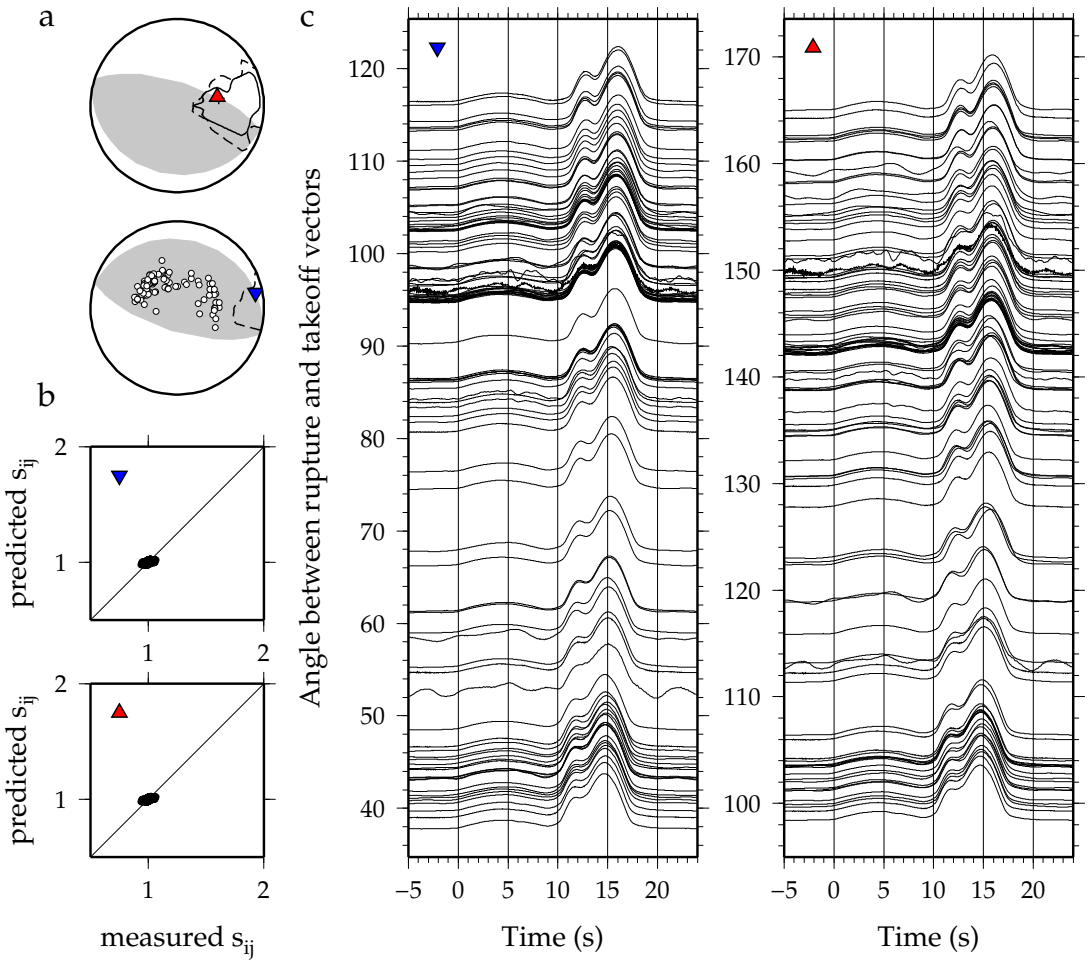

Figure B32: Synthetics for the north-northeast-dipping subhorizontal plane for the 3 March 2002 Mw 6.3 and Mw 7.4 earthquakes. Subplots are as described at the beginning of the Appendix. Synthetics do not replicate the rupture pattern seen for the earthquake.

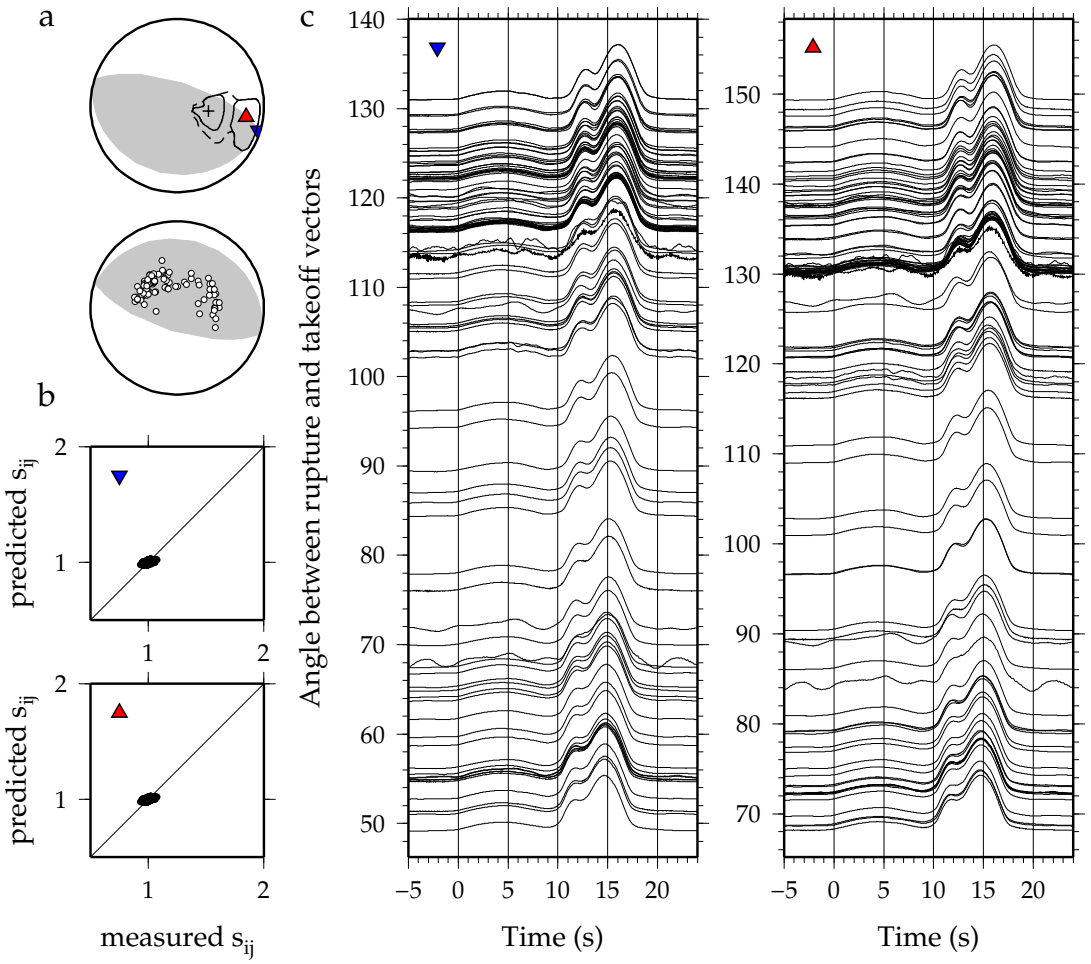

Figure B33: Synthetics for the south-southwest-dipping near-vertical plane for the 3 March 2002 Mw 6.3 and Mw 7.4 earthquakes. Subplots are as described at the beginning of the Appendix. Synthetics replicate little from the rupture pattern seen for the earthquake.

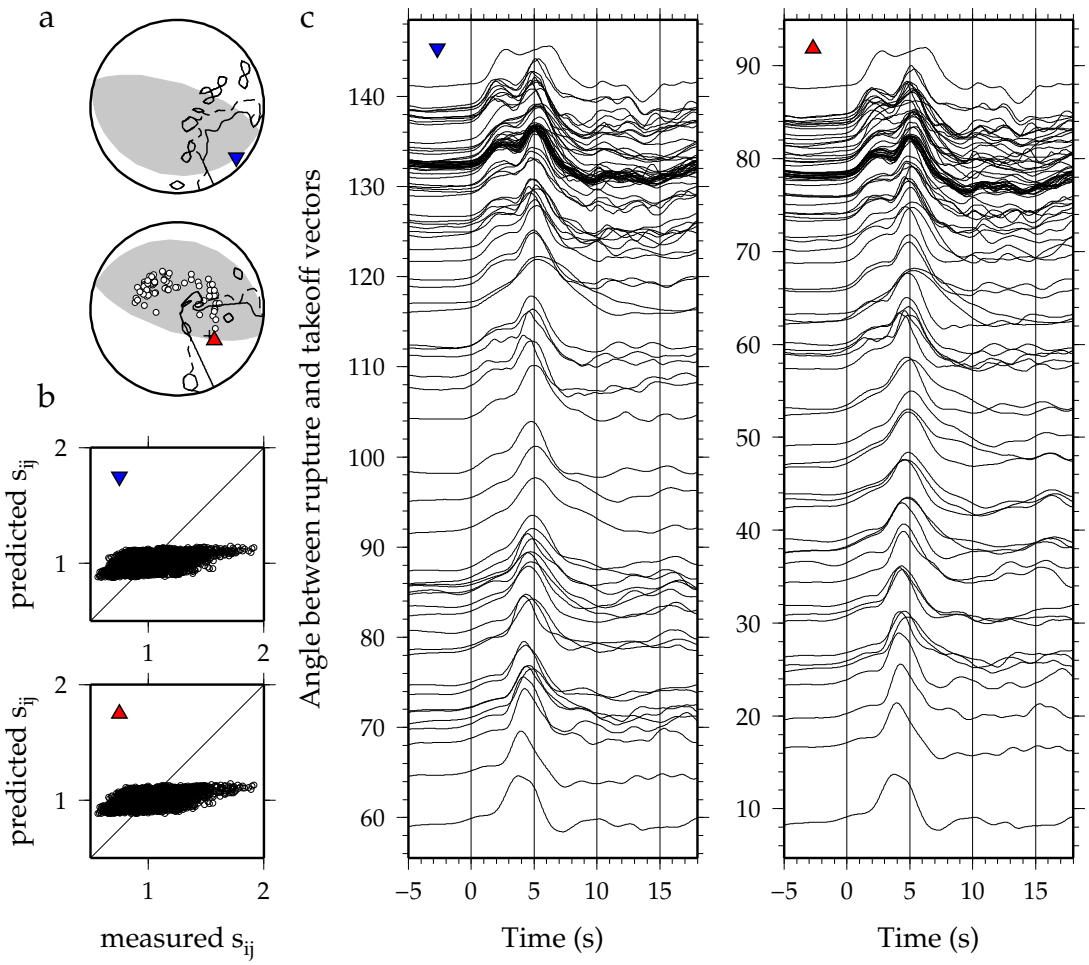

Figure B34: Results for the 3 March 2002, Mw 7.4 earthquake, which occurred at 36.50°N 70.48°E and 225 km depth. Subplots are as described at the beginning of the Appendix. For this event, we cannot tell which of the nodal planes is the fault plane, since the rupture propagated towards the intersection of the nodal planes.

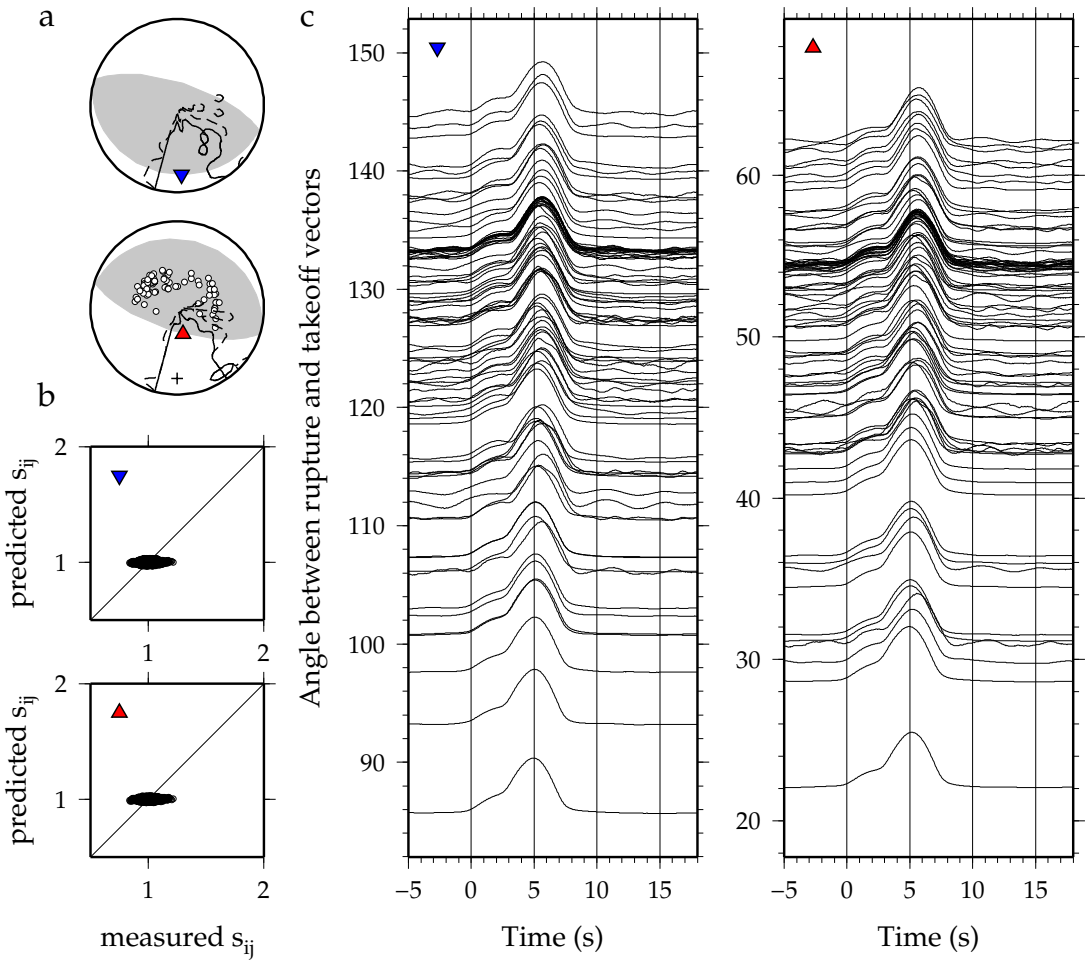

Figure B35: Synthetics for the north-northeast-dipping subhorizontal plane for the 3 March 2002, Mw 7.4 earthquake. Subplots are as described at the beginning of the Appendix. Synthetics do not replicate the rupture pattern seen for the earthquake.

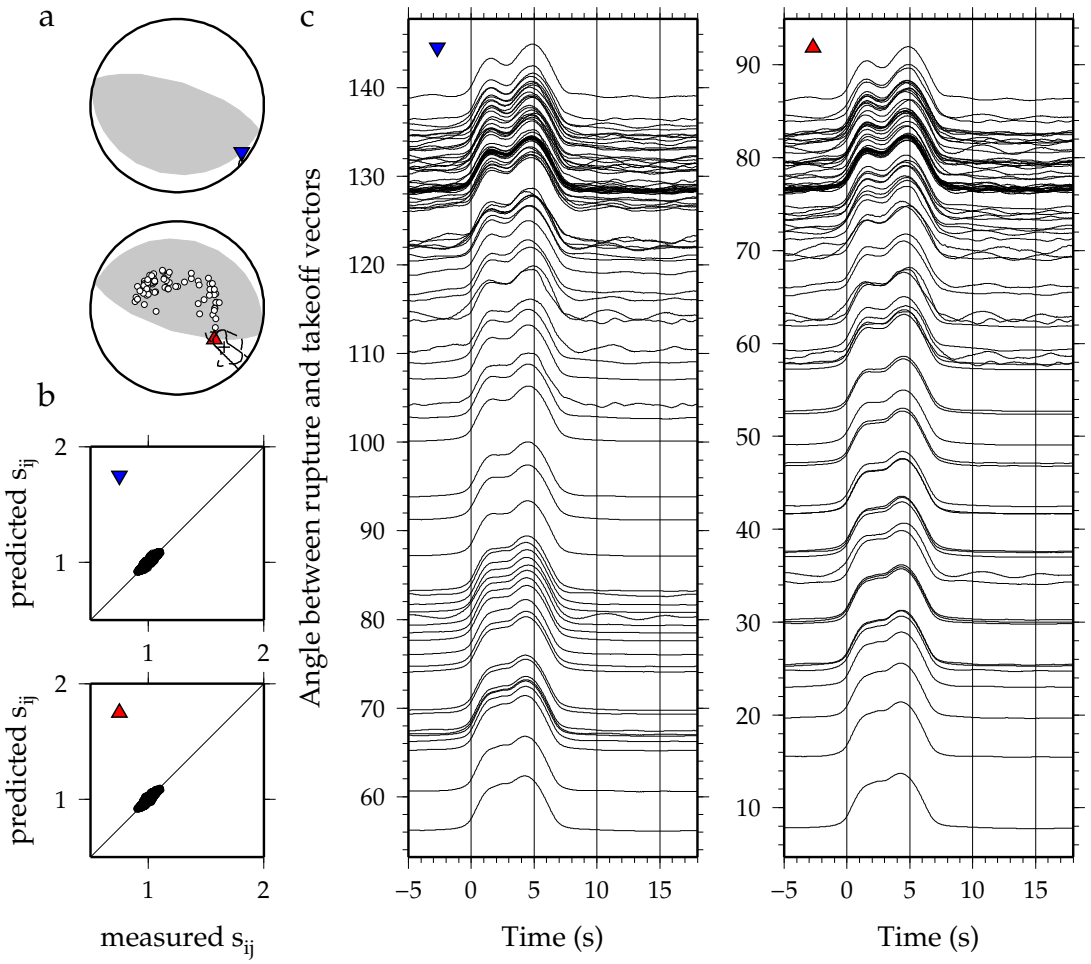

Figure B36: Synthetics for the south-southwest-dipping near-vertical plane for the 3 March 2002, Mw 7.4 earthquake. Subplots are as described at the beginning of the Appendix. Synthetics replicate little from the rupture pattern seen for the earthquake.

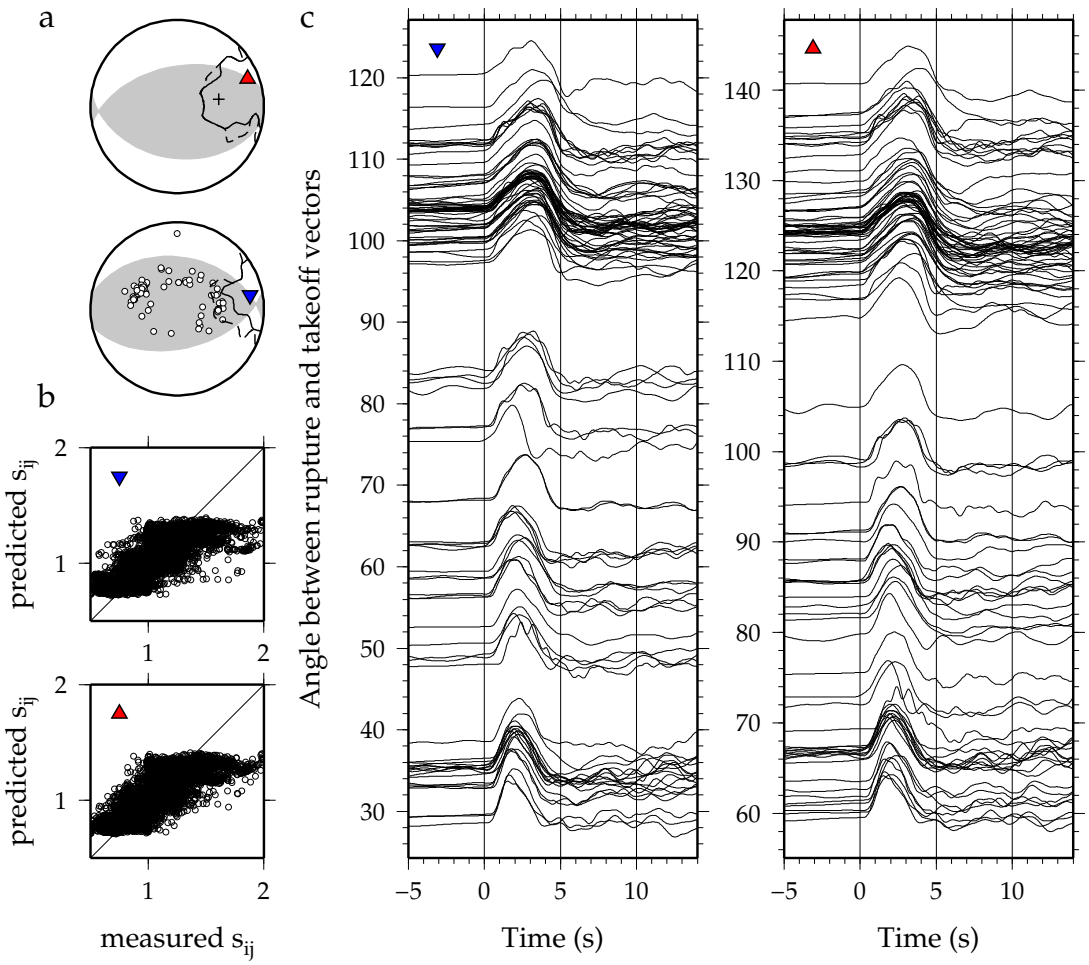

Figure B37: Results for the 12 December 2005, Mw 6.5 earthquake, which occurred at 36.36°N 71.09°E and 224 km depth. Subplots are as described at the beginning of the Appendix. For this event, we cannot tell which of the nodal planes is the fault plane, since the rupture propagated towards the intersection of the nodal planes.

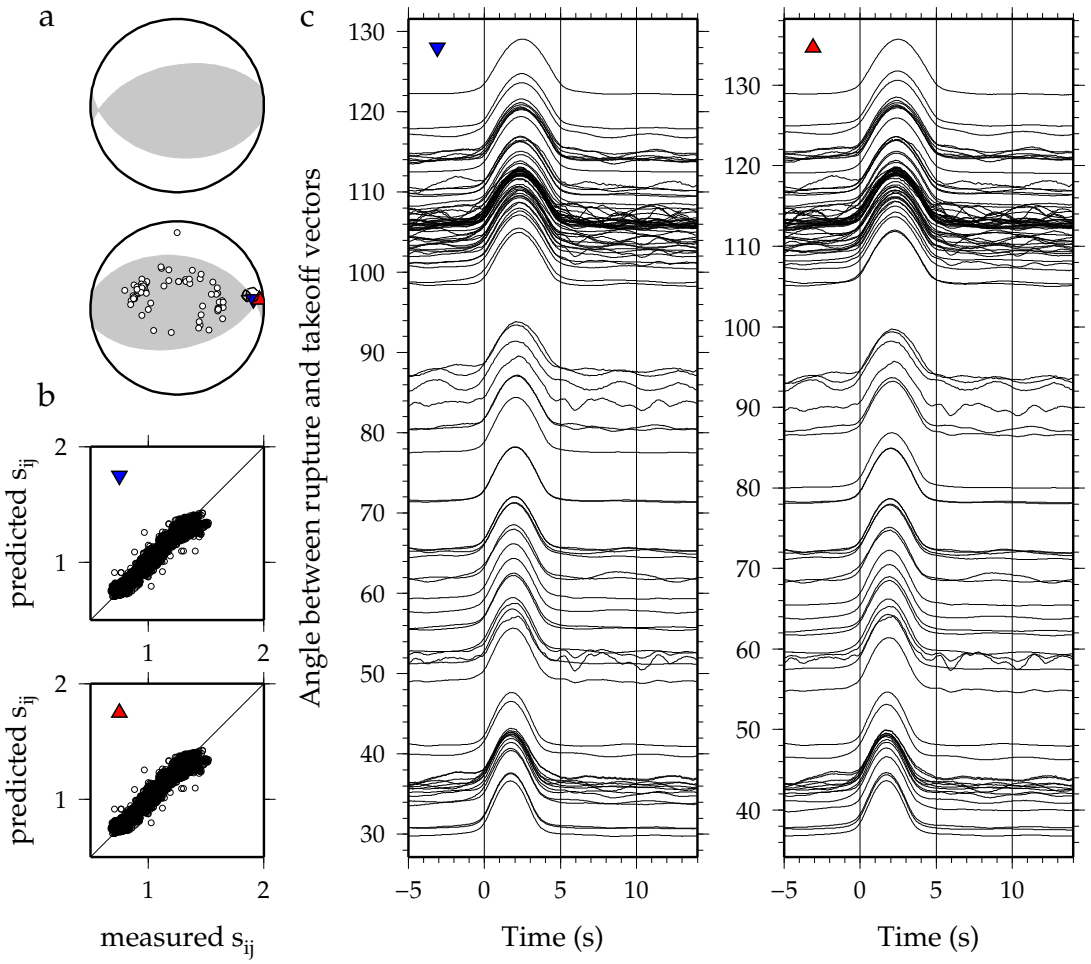

Figure B38: Synthetics for the north-dipping plane for the 12 December 2005, Mw 6.5 earthquake. Subplots are as described at the beginning of the Appendix. Synthetics do not replicate the rupture pattern seen for the earthquake.

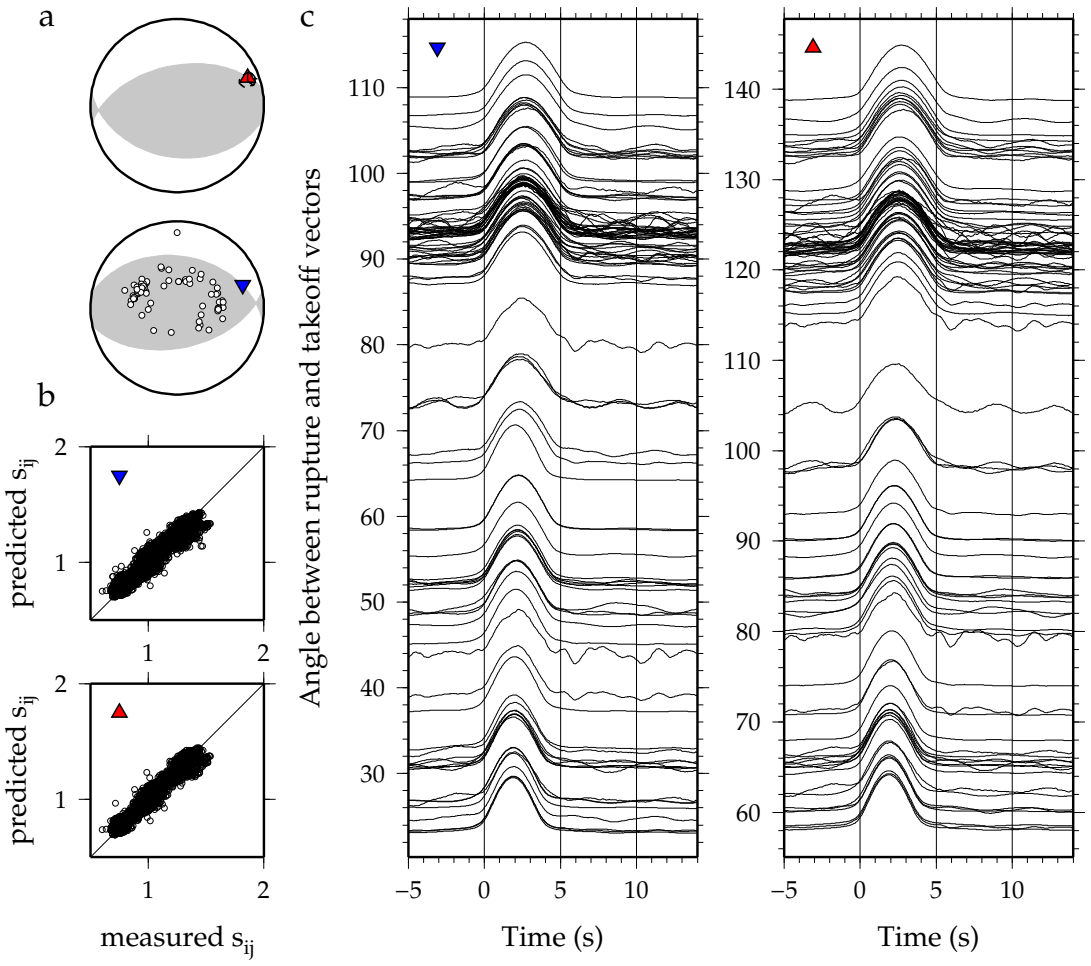

Figure B39: Synthetics for the south-dipping plane for the 12 December 2005, Mw 6.5 earthquake. Subplots are as described at the beginning of the Appendix. Synthetics replicate the rupture pattern seen for the earthquake.

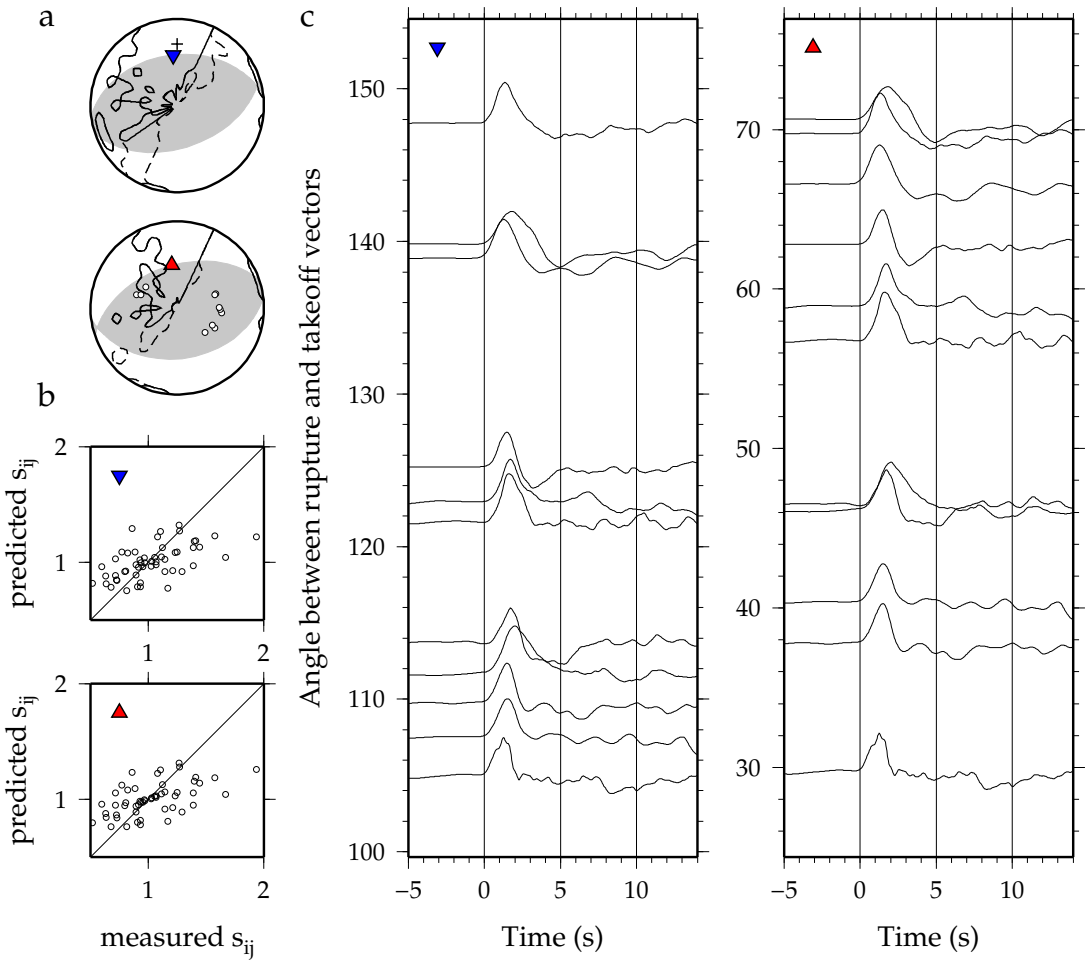

Figure B40: Results for the 22 October 2009, Mw 6.2 earthquake, which occurred at 36.52°N 70.95°E and 185 km depth. Subplots are as described at the beginning of the Appendix. For this event, we cannot tell which of the nodal planes is the fault plane.

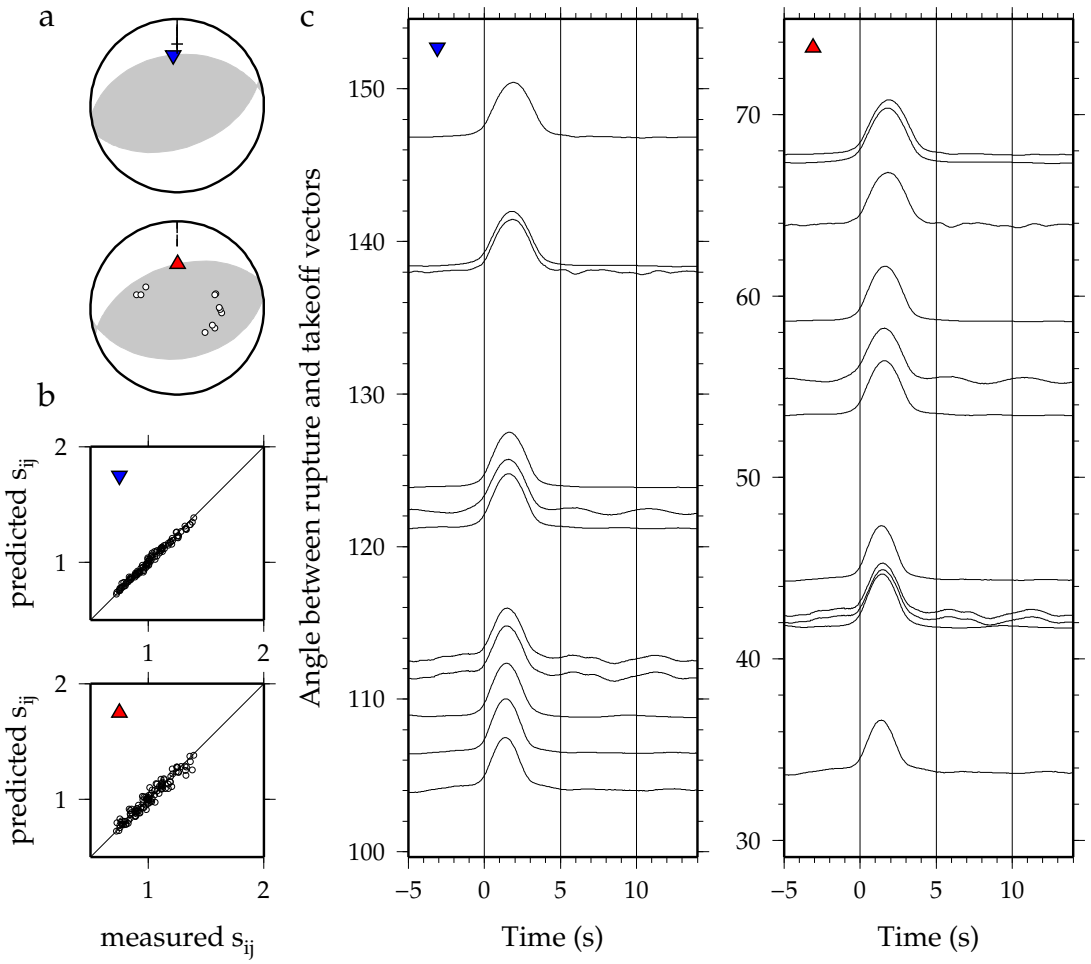

Figure B41: Synthetics for the south-southeast-dipping plane for the 22 October 2009, Mw 6.2 earthquake. Subplots are as described at the beginning of the Appendix. Synthetics replicate the rupture pattern seen for the earthquake.

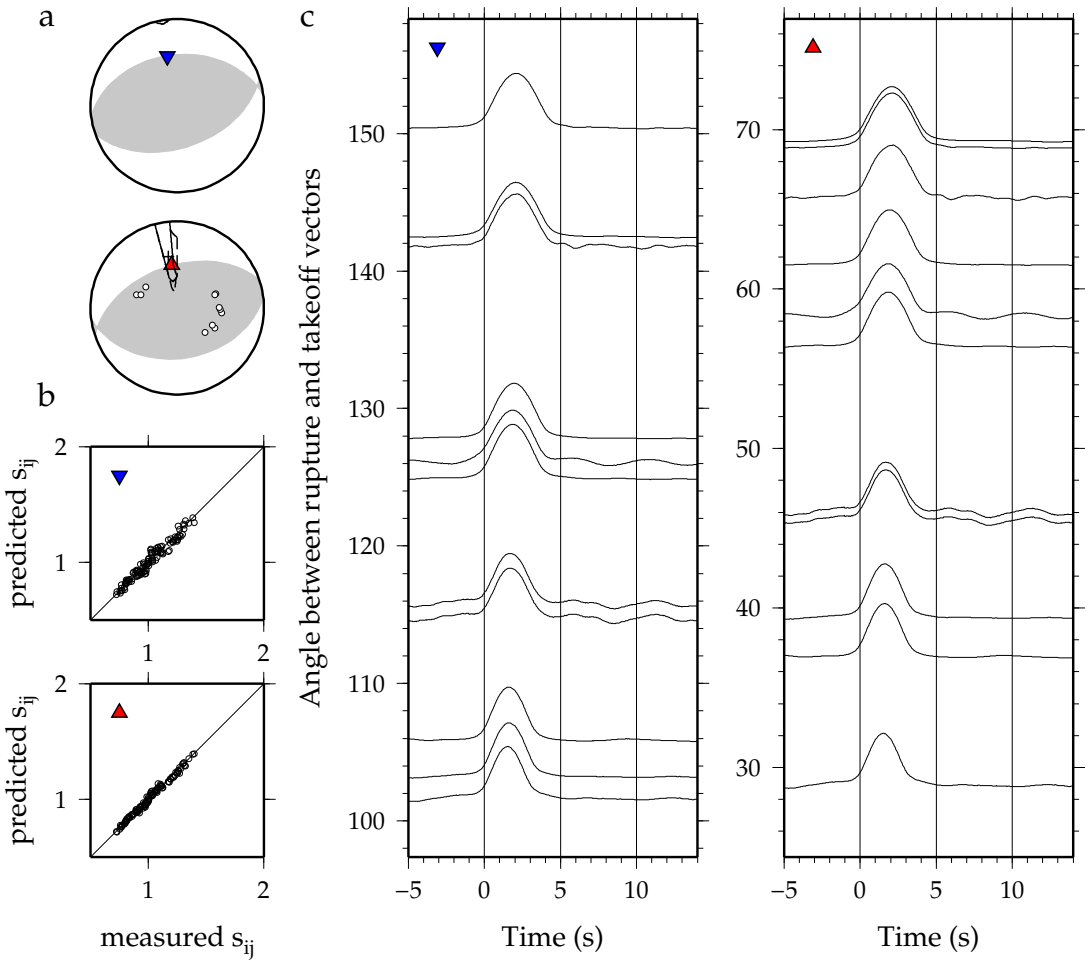

Figure B42: Synthetics for the north-northwest-dipping plane for the 22 October 2009, Mw 6.2 earthquake. Subplots are as described at the beginning of the Appendix. Synthetics replicate the rupture pattern seen for the earthquake.

References

Ben-Menahem, A., 1962. Radiation of seismic body waves from a finite moving source in the Earth, *J. Geophys. Res.*, 67, 345-350.

Billington, S., B.I. Isacks, and M. Barazangi, 1977. Spatial distribution and focal mechanisms of mantle earthquakes in the Hindu Kush-Pamir region: A contorted Benioff zone, *Geology*, 5, 699–704.

Brantut, N., J. Sulem, and A. Schubnel, 2011. Effect of dehydration reactions on earthquake nucleation: Stable sliding, slow transients, and unstable slip, *J. Geophys. Res.*, 116, B05304.

Burtman, V.S., and P. Molnar, 1993. Geological and geophysical evidence for deep subduction of continental crust beneath the Pamir, *Geological Society of America Special Papers*, 281, 1–76.

Chatelin, J.L., S.W. Roecker, D. Hatzfeld, and P. Molnar, 1980. Microearthquake seismicity and fault plane solutions in the Hindu Kush region and their tectonic implications, *J. Geophys. Res.*, 85, 1365–1387.

Cruciani, C., E. Carminati, and C. Doglioni, 2005. Slab dip vs. lithosphere age: No direct function, *Earth Planet. Sci. Lett.*, 238, 298-310.

De Mets, C., R.G. Gordon, D.F. Argus, and S. Stein, 1994. Effects of recent revision to the geomagnetic reversal time scale on estimates of current plate motions, *Geophys. Res. Lett.*, 21, 2191–2194.

Fan, G., J.F. Ni, and T.C. Wallace, 1994. Active tectonics of the Pamirs and Karakorum, *J. Geophys. Res.*, 99, 7131–7160.

Frohlich, C., 2006. *Deep Earthquakes*, 2nd ed., Cambridge Univ. Press, Cambridge, U. K.

Global Centroid Moment Tensor (CMT) Catalog. [http://www.globalcmt.org/CMTsearch.html]

Gudmundsson, O., and M. Sambridge, 1998. A regionalized upper mantle (RUM) seismic model, *J. Geophys. Res.*, 103, 7121-7136.

Hacker, B. R., G. A. Abers, and S. M. Peacock, 2003. Subduction factory 1. Theoretical mineralogy, densities, seismic wave speeds, and H2O contents, *J. Geophys. Res.*, 108(B1), B012029.

Hafkenscheid, E., M. J. R. Wortel, and W. Spakman, 2006. Subduction history of the Tethyan region derived from seismic tomography and tectonic reconstructions, *J. Geophys. Res.*, 111, B08401.

Hamburger, M.W., D.R. Sarewitz, T.L. Palvis, and G.A. Popandopulo, 1992. Structural and seismic evidence for intracontinental subduction in the Peter the First Range, central Asia, *Geol. Soc. Am. Bull.*, 104, 397–408.

Incorporated Research Institutions for Seismology (IRIS). [http://www.iris.edu/hq/]

International Seismological Centre (ISC). [http://www.isc.ac.uk/]

Kiser, E., M. Ishii, C. H. Langmuir, P. M. Shearer, and H. Hirose, 2011. Insights into the mechanism of intermediate-depth earthquakes from source properties as imaged by back projection of multiple seismic phases, *J. Geophys. Res.*, 116, B06310.

Koulakov, I., and S. V. Sobolev, 2006. A tomographic image of Indian lithosphere break-off beneath the Pamir-Hindu Kush region, *Geophys. J. Int.*, 164, 425-440.

Lister, G., B. Kennett, S. Richards, and Marnie F., 2008. Boudinage of a stretching slablet implicated in earthquakes beneath the Hindu Kush, *Nature Geosci.*, 1, 196–201.

Li, J., Y.M. He, and Z.X. Yao, 2006. Source finiteness and rupture propagation using higher-degree moment tensors, *Bull. Seis. Soc. Am.*, 96, 1241–1256.

Lukk, A.A., and L.P. Vinnik, 1975. Tectonic interpretation of the deep structure of the Pamirs, *Geotektonika*, 10(5), 73–80.

Lou, X., C. Chen, and C. Yu, J. Ning, 2009. Intermediate-depth earthquakes beneath the Pamir-Hindu Kush region: Evidence for collision between two opposite subduction zones, *Earthq. Sci.*, 22, 659-665.

Luyendyk, B. P., 1970. Dips of downgoing lithospheric plates beneath island arcs, *Geol. Soc. Am. Bull.*, 81, 3411-3416.

Masson, D G, 1991. Fault patterns at outer trench walls, *Mar. Geophys. Res.*, 13. 3, 209-225.

McGinnis, L.D., 1971. Gravity fields and tectonics in the Hindu Kush, *J. Geophys. Res.*, 76, 1894-1904.

Negredo, A.M., A. Replumaz, A.Villaseñor, and S. Guillot, 2007. Modeling the evolution of continental subduction processes in the Pamir-Hindu Kush region, *Earth Planet. Sci. Lett.*, 259, 212–225.

Omori, S., T. Komabayashi, and S. Maruyama, 2004. Dehydration and earthquakes in the subducting slab: empirical link in intermediate and deep seismic zones, *Phys. Earth Planetary Int.*, 146, 297–311.

Pavlis, G.L. and S. Das, 2000. The Pamir-Hindu Kush seismic zone as a strain marker for flow in the upper mantle, *Tectonics*, 19, 103–115.

Pegler, G., and S. Das, 1998. An enhanced image of the Pamir-Hindu Kush seismic zone from relocated earthquake hypocenters, *Geophys. J. Int.*, 134, 573–595.

Replumaz, A., K. Karason, R. van der Hilst, J. Besse, and P. Tapponnier, 2004. 4-D evolution of SE Asia mantle structure from geological reconstruction and seismic tomography, *Earth Planet. Sci. Lett.*, 221, 103-115.

Replumaz, A., A. M. Negredo, S. Guillot, and A. Villaseñor, 2010. Multiple episodes of continental subduction during India/Asia convergence: Insight from seismic tomography and tectonic reconstruction, *Tectonophysics*, 483, 125–134.

Roecker, S. W., 1982. Velocity structure of the Pamir-Hindu Kush region: possible evidence of subducted crust, *J. Geophys. Res.*, 87, 945-959.

Scholz, C. H., 2002. *The Mechanics of Earthquakes and Faulting*, 2nd ed., Cambridge Univ. Press, Cambrifge, U. K.

Van der Voo, R.,W. Spakman, and H. Bijwaard, 1999. Tethyan subducted slabs under India, *Earth Planet. Sci. Lett.*, 171, 7–20.

VanDecar, J.C., and R.S. Crosson, 1990. Determination of teleseismic relative phase arrival times using multi-channel cross correlation and least squares, *Bull. Seis. Soc. Am.*, 80, 150-169.

Verma, R.K., and C.C. Sekhar, 1985. Seismotectonics and focal mechanisms of earthquakes from Pamir-Hindukush regions, *Tectonophysics*, 112, 297–324.

Vinnik, L.P., A.A. Lukk, and I.L. Nersesov, 1977. Nature of the intermediate seismic zone in the mantle of the Pamir-Hindu Kush, *Tectonophysics*, 38, 9–14.

Warren, L. M., 2008. A giant subducting sausage, *Nature Geoscience*, 1, 154-155.

Warren, L. M., and P. G. Silver, 2006. Measurement of differential rupture durations as constraints on the source finiteness of deep-focus earthquakes, *J. Geophys. Res.*, 111, B06304.

Warren, L. M., A. N. Hughes, and P. G. Silver, 2007. Earthquake mechanics and deformation in the Tonga-Kermadec subduction zone from fault-plane orientations of intermediate- and deep-focus earthquakes, *J. Geophys. Res.*, 112, B05314.

Warren, L. M., M. A. Langstaff, and P. G. Silver, 2008. Fault-plane orientations of intermediate-depth earthquakes in the Middle America trench, *J. Geophys. Res.*, 113, B01304.

Zhu, L., D. V. Helmberger, C. K. Saikia, and B. B. Woods, 1997. Regional waveform calibration in the Pamir-Hindu Kush region, *J. Geophys. Res.*, 102, 22, 799-22, 813.

Zarifi, Z., and J. Havkov, 2003. Characteristics of dense nests of deep and intermediate-depth seismicity, *Adv. in Geophys.*, 46, 237–278.

Vita Auctoris

Wan-Jou Chen graduated from National Taiwan University, Taiwan, with a Bachelor of Science degree in Geology in June, 2007. From there she worked in the Institute of Earth Sciences, Academia Sinica, Taiwan, as a research assistant from 2007 to 2010.

Later in 2010, she decided to continue her education and pursue an M.S. degree in Geophysics at Saint Louis University when she learned that she was accepted to the graduate program.